Doctoral Thesis

Structure and Reactivity of Small Clusters

Kohei Imura

Department of Chemistry,

Graduate School of Science,

Osaka University,

Toyanaka, Osaka 560-0043, Japan

February, 2000

Doctoral Committee

Professor Toshio Kasai, Supervisor

Professor Takeshi Ohno

Professor Kizashi Yamaguchi

Professor Sumio Kaizaki

Acknowledgements

The author is deeply indebted to many people for the work in this thesis. The author would first like to express his profound and sincere thankfulness to Professor Toshio Kasai for the continuous guidance, encouragement, and helpful indications. The author would also like to be grateful to Professor Ron Naaman of the Weizmann Institute of Science in Israel for giving a chance to study at the institute, many valuable suggestions, and continuous interesting. The author would also like to acknowledge the considerable suggestions and kind guidance of Associate Professor Ohoyama. The author wishes to thank Dr. Dock-Chil Che and Dr. Michio Okada for their encouragement. Thanks are extended to members of the stuff in the machine shop of Osaka university for their help in construction of the several experimental apparatus. The author thanks the Japan Society for the Promotion Science for financial support. The author would like to thank all students in Kasai laboratory for being so generous and kind to him. Finally, the author wishes to give his best gratitude to his parents and his wife.

Contents

Chapter 1 General Introduction

1-1 Cluster Chemistry

A term cluster refers to beam particles, which are an assembly of clustered atoms bound together by moderate force such as van der Waals force or hydrogen bonding. They clusters range in size from a dimer up to as large as microcrystals, or microdrops of many million atoms. By Becker and Henkes[1], the first observation of a weakly bounded cluster in the expanded beam was on anomalous velocity distribution of hydrogen beams compared to the Maxwellian distribution in molecular beams emanating from effusive nozzle source (When they worked with low-temperature hydrogen beams, they observed within a narrow range of source pressure, P_0, the appearance of a characteristic discontinuity in the speed distribution. Simultaneously, a drastic increase of beam intensity with increasing P_0, was found.) Basic factor for producing a cluster beam source is a nozzle operating conditions and its geometry. In order to produce cluster beam effectively, higher stagnation pressure, lower temperature, and low expansion rates of a nozzle are required. Recently, supersonic expansion technique has been widely used to produce a cluster beam due to their low rotational temperature and several other merits for apparatus. In addition, a laser evaporation technique enables us to synthesize various organo-metallic clusters, which opened up a new field in gas phase chemistry.

Many of the present cluster beam activities have been concentrated on studies with such as elastic, inelastic, and reactive interactions of clusters with other gases, on surface, with electron, and with photons. At present, these kinds of experiments provide information about cluster properties like its size effect and structure. Once the relevant cluster properties are well-known, it will be possible to use cluster beam experiments to

study such diverse topics as inter-atomic forces, kinetics of chemical reactions, surface roughness, or the material properties in the transition regime between gas and condensed phase.

Recently, especially, small clusters have also been used to study on basic understanding of (1) the solvent effect in chemistry and biology, (2) stereo-dynamics, (3) transition state spectroscopy, and (4) catalysis chemistry.

(1) Weakly bound in van der Waals and hydrogen-bonded clusters are excellent frame work for exploring solvent effects on reaction dynamics because of their simplicity derived from relatively small number of particles. Therefore, these systems imply important conceptual and computational advantages for understanding condensed matter. One of the most important and famous solvent effects is cage effect. While photodissociation of an isolated diatomic molecule results in a direct separation of the atoms, when the molecules is mixed in solid matrix or in solution, photolysis may occur in quite different way. The surrounding atoms and molecules behave like a cage, to confine diffusion of photofragments, and give delay in their separation time.

Manifestations of cage effect in clusters have been found both experimentally and theoretically. In one of these studies, Garcia-Vela and Gerber revealed that single solvent atom is able to cause a significant solvent effect. They theoretically studied the photodissociation of Ar-HCl vdW cluster using time-dependent-SCF calculation.[2] When the HCl molecule in a cluster was dissociated by a 193 nm laser radiation, the H atom was produced as a photofragment. This product H atom is thought to experience multiple collisions between Ar and Cl cage. For photolysis of an isolated HCl molecule, the recoil direction of hydrogen lies along the internuclear axis (transition moment) and the angular distribution consists of a delta-function. In the case of Ar-HCl, due to

multiple collisions, the recoiled directions are widely spread out, giving two main peaks around 45 and 135 degrees from internuclear axis of Ar-Cl. It is good manifestation that only single solvent is sufficient to change their dynamics drastically.

(2) Clusters can be applied to investigate steric effects in reactive and non-reactive collisions by exploiting their geometrical limitation. For example, in H + N_2O and H + CO_2 binary reaction, we can exploit binary van der Waals clusters such as HX-N_2O and HX-CO_2 for their corresponding precursors. The reactions are initiated by laser photolysis of HX in the corresponding cluster, then the produced hydrogen atom attacks the second reagent with restricted range of impact parameters by geometry of the precursor cluster.[3,4] A prerequisite for a full interpretation of the results is that structure of precusor cluster of interest is well-known. Knowledge of the amplitude of bending vibrations within the cluster is also important because for large-amplitude, low-frequency-bending vibrations of H atoms in an HX-CO_2 cluster, a range of impact parameter for the collision will much larger than for low-amplitude vibrations. The large amplitude in bending of the H atom in HBr-CO_2 permits some side-on attacks of the H at CO_2, and this approach was shown to be more reactive than end-on attack initiated in HCl-CO_2 clusters.[5] By using such intramolecular cluster reactions, we may control the reaction and also examine corresponding transition state spectroscopy.

(3) One of the pioneering study of transition state spectroscopy by exploiting the van der Waals clusters is negative ion photodetachment experiment.[6,7] This experiment is conceptually similar to the mentioned methodology in (2). The largest difference is that using photodetachment of stable negative ions, rather than electronic excitation of clusters, allows access to transition state. For example, photodetachment of the IHI^- anion forms an unstable IHI complex, which lies in the transition state region

for the I + HI reaction. The photoelectron spectrum attributed to the IHI complex that provides a detailed probe of the I + HI transition state region.

(4) After the development of laser evaporation methods, clusters component of metal and simple molecule have been paid much attention because of its applicability to model system on solid surface reaction. Smalley and co-workers have reported the size dependence of the hydrogen adsorption probability on the Co clusters.[8] They first produced Co cluster beam and identified its size distribution. Secondly, the cluster beam was introduced into a fast flow reactor, where H_2 gas was supplied. After passing through the reactor, the size distribution of reaction products was measured. The result showed anomalous size distribution of products. While this is the first demonstration of the size dependence study, in order to investigate the size dependence on reactivity, we have to select the neutral cluster size. However, nobody has done this concrete work so far because of its difficulty. In this thesis I would like to propose one of the most powerful method for neutral cluster size-selection.

As several examples have been shown above, van der Waals and hydrogen-bonded clusters have a plenty of attraction and possibility to understand and reveal reactions in more complex surroundings, such as liquids, solids, and interfaces, and describe chemistry on a microscopic level, the molecular interactions that the shape the overcome of a chemical reactions.

1-2 Electric Dipole Moment and Molecular Structure

Permanent electric dipole moment is principal electrostatic entity governing the molecular structure. It is also an important quantity in the microscopic understanding of

reaction dynamics since long range intramolecular interaction are dominated by dipole forces. Furthermore, dipole moment is a property that is an overall measure of the ionic bonding character and is routinely calculated by *ab initio* calculation, along with the equilibrium internuclear separation r_e. For obtaining reasonably good estimate for the electronic wave function, the calculated dipole moment should be the most reliable physical property because it is described by a sum of one electron operators. In many cases, dipole moment is extracted from analysis of high-resolution spectra than r_e. However, it is well known that the extraction of r_e from experimentally determined rotational constant may be in error because B_{eff} is inversely proportional to r_e^2. Specially, in the case of light atoms and weakly bonded cluster, it readily turns out to be difficult. Thus a comparison between the experimentally determined and theoretically predicted values of dipole moment is necessary as an initial test of quantitative reliability of any theoretical bonding model.

Traditionally, dipole moments have been measured by microwave spectroscopic techniques.[9] This method utilizes the Stark shift in the microwave region and magnitude in the shift depends on the dipole moment. In the gas phase, molecular beam electric resonance method has been used to determine dipole moment. However, because of the limitation of sensitivity and difficulty of the microwave tuning, this method has a difficulty to apply to the gas phase clusters or transient radicals. As it will be shown later, the hexapole focusing technique is a very useful tool for determining electric dipole moment of molecule and cluster.

References

1. E.W. Becker, K. Bier, W. Henkins, *Z. Phys.*, **146**, 333 (1956).
2. A. Garcia-Vela and R.B. Gerber, *J. Chem. Phys.*, **97**, 3297 (1992); A.Garcia-Vela, R.B. Gerber, D.G. Imure, J.J. Valentini, *Chem. Phys. Lett.*, **202**, 473 (1993).
3. C. Wittig, Y.M. Engel, R.D. Levine, *Chem. Phys. Lett.*, **153**, 411 (1988); E. Bohmer, S.K. Shin, Y. Chen, C. Wittig, *J. Chem. Phys.*, **97**, 2536 (1992).
4. C. Jouvet C. Jouvet, M. Boivineau, M.C. Duval and B. Soep, *J. Phys. Chem.*, **95**, 7145 (1991); M.C. Duval, B. Soep and W.H. Brengenridge, *J. Chem. Phys.*, **95**, 7145 (1991).
5. Y.P. Zheng, S.W. Sharpe, S.K. Shin, C. Wittig and R.A. Beaudet, *J. Chem. Phys.*, **97**, 5392 (1992).
6. A. Weaver and D.M. Neumark, *Faraday Discuss. Chem. Soc.*, **91**, 5 (1991).
7. S.E. Manolopoulos, K. Stark, H-J. Werner, D.W. Arnold, S.E. Bradforth and D.M. Neumark, *Science*, **262**, 1852 (1993).
8. M.E. Geusic, M.D. Morse, R.E. Smalley, *J. Chem. Phys.*, **82**, 590 (1985).
9. C.H. Townes, A.L. Schawlow, "*Microwave Spectroscopy*", Dover, 1975.

Chapter 2 Experimental

In this chapter a survey is given of the important techniques used in the experiment presented in the following chapters.

2-1 Structural Selection by Using the Electrostatic Hexapole Field

In this section, we describe the methodology for size selection of neutral clusters by using an electrostatic hexapole field. Hexapole technique has been used as a rotational state selector of molecule and it becomes possible to produce the oriented molecular beam. This technique could be understood in a qualitative way from classical mechanics, whereas those detail understanding require a quantum mechanical approach. First, we describe classical treatment for the quantum state selection of a molecule, and detailed treatment is discussed by quantum mechanics. Finally, we describe the applicability to neutral cluster size selection and the determination of the electric dipole moment of clusters.

2-1.1 Theory of electrostatic hexapole method

By electrostatic field, a molecule which has an electric dipole moment will be exerted and generate a torque and thereby it can be change its rotational motion. Then, rotational energy levels are perturbed by so called Stark effect. These effects can be described qualitatively by classical mechanics and quantitatively by quantum mechanics. Typical Stark energies for various molecular symmetries are indicated in Table 2-1.

Consider a simple case, for a rotating linear molecule with angular momentum perpendicular to electric field. The field tends to twist this molecule and gives it a faster rotation when the electric dipole moment is oriented in the direction of the field, and slow the rotation when it is pointed oppositely to the field. Hence, on the average, the dipole moment is oriented in the opposite direction from the field in contrast with what

Table 2-1.

Stark Effect For	W_{Stark}	Example
Linear molecules ($^1\Sigma$ state)	$-\frac{\mu^2 E^2}{2Bch(2J-1)(2J+3)}\left[1-\frac{3M^2}{J(J+1)}\right]$	NaCl, CO
No bending excited		
Linear molecules (Π state)	$-\mu E\frac{\Omega M}{J(J+1)}$	NO, OH
No bending excited		
Linear molecules ($^1\Sigma$ state)	$-\mu E\frac{Ml}{J(J+1)}$	N_2O, LiCN
Bending excited		
Symmetric top	$-\mu E\frac{KM}{J(J+1)}$	CH_3F
Asymmetric top	$\frac{W_1^0+W_2^0}{2}\pm\sqrt{\left(\frac{W_1^0-W_2^0}{2}\right)^2+E^2\mu_{12}^2}$	H_2O, HDO
(two repelling levels)		

Note: HFS and Λ–doubling are neglected. The permanent dipole moment is described by μ; J, K, M are rotational quantum numbers determining the angular momentum and its projections on a space-fixed axis(M) and the molecular axis (K); l describes the vibrational angular momentum projected on the molecular axis. W^0_1 and W^0_2 stand for the undisturbed energies of a two-level system, and $\mu_{12}E$ for an off-diagonal interaction.

would be expected if there were no rotation. Frequency difference between two extremes can be rationalized as follows.

$$f \propto \frac{2\mu E}{I\omega^2}, \tag{2-1}$$

where μ is the dipole moment, E the electric field, I the moment of inertia, and ω the angular velocity. Then the change in energy is expressed as $f\mu E$.

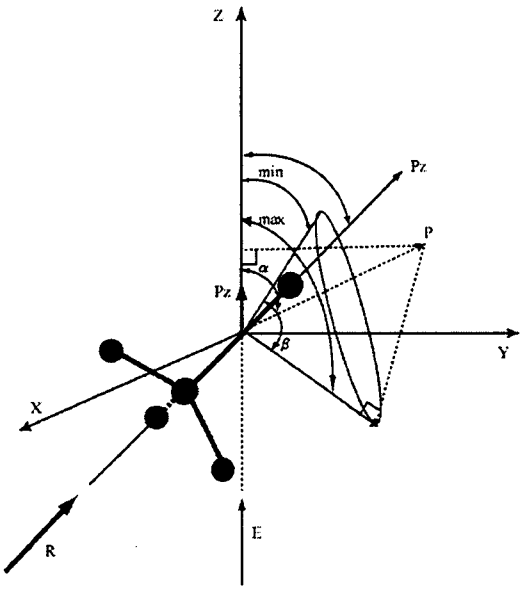

Figure 2-1. The angle α determines the position of P in the space-fixed coordinate system with respect to the Z axis, which is set by the E axis. The PZ is the Z component of P. The instantaneous position of Pz with respect to the Z axis is defined by the angle θ. Furthermore, the angle θ is bounded by θ_{min} and θ_{max}, which are characteristics of a given rotational state.

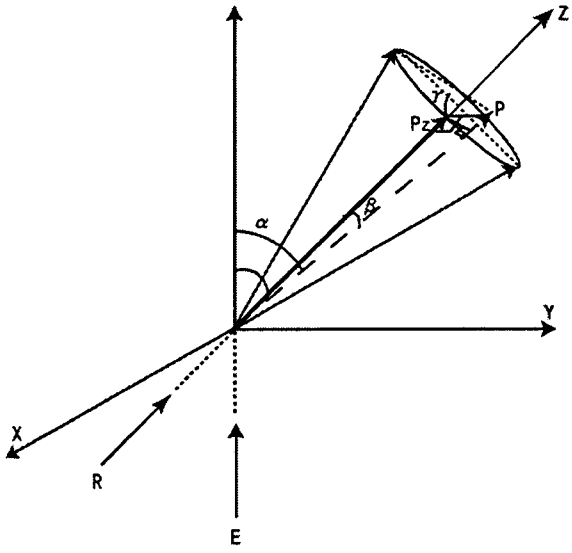

Figure 2-2. Pz precesses about P at a constant rate, making a cone of angle β. The angle χ is the dihedral angle between the P, Z plane the P, Pz plane. The polar angle θ, in the spaced-fixed coordinate system, is related to angles α, β, χ by $\cos\theta = \cos\alpha\cos\beta + \sin\alpha\sin\beta\cos\chi$

If a linear molecule rotates with its angular momentum parallel or anti-parallel to the field, the energy change is also the same amount. An average energy change over

random orientations of a rotating molecule gives no net change in energy, various positive and negative changes are exactly cancelled out each other.

Symmetric top molecules show a rather different type Stark effect, since their dipole moment may have components parallel to the angular momentum. Thus for a symmetric top molecule rotating around its symmetry axis, the dipole moment is in the direction of total angular momentum and its energy in an electric field is written as $-\mu E\cos\theta$, where θ is an angle between angular momentum and E. Since a symmetric top molecule experiences the processional motion, the angle θ varies within limits specified θ_{max} and θ_{min}. The rotational behavior of a symmetric top molecule in an electric field is completely described by three angular momentum vectors: P (total angular momentum), Pz (z component of P), and PZ (the projection of P on the Z axis) as shown in Fig. 2-1. It is seen that

$$\cos\alpha \equiv \frac{|PZ|}{|P|} \tag{2-2}$$

$$\cos\beta \equiv \frac{|Pz|}{|P|} \tag{2-3}$$

from which θ_{max} and θ_{min} are determined:

$$\cos\theta_{\max} = \cos(\alpha+\beta) \tag{2-4}$$

$$\cos\theta_{\min} = \cos(\alpha-\beta) \tag{2-5}$$

According to the spherical triangle relationship, following equation can be derived.

$$\cos\theta = \cos\alpha\cos\beta + \sin\alpha\sin\beta\cos\gamma \tag{2-6}$$

After the Jacobian transformation, orientational distribution can be expressed.

$$P(\cos\theta) = [\pi\sqrt{(}\cos\theta_{\max} - \cos\theta)(\cos\theta - \cos\theta_{\min})]^{-1} \tag{2-7}$$

Then averaged from θ_{max} to θ_{min}, averaged can be derived.

$$\langle\cos\theta\rangle \equiv \cos\alpha\cos\beta = \frac{KM}{J^2}\ , \tag{2-8}$$

For easier comparison, rotational quantum numbers are introduced as follows: $P = J$, $PZ = K$, $Pz = M$. When a vector model is used, J^2 must be always replaced by $J(J+1)$, then Stark energy turns out to be:[1]

$$E = \mu E\frac{KM}{J(J+1)}\ , \tag{2-9}$$

The change in energy for a symmetric top molecule is thus proportional to the first power of μE, whereas that for a linear molecule is proportional to the second power of μE and is much smaller. We referred to as "first order" and "second order" Stark effect, respectively.

The quantum mechanical treatment of the Stark effect starts with the Hamiltonian and the wave equation.[2] The rotational wavefunction Ψ_{JKM} of a symmetric

top molecule is characterized by the total angular momentum J, its projection K on the molecular axis, and its projection M on the space fixed axis of quantization, the electric field E. The axis of molecule precesses around the total angular momentum J, and J precesses around the space fixed axis, that is Z axis.

When the center of mass is chosen as the origin of the space fixed system, the relationship between the body fixed and the space fixed frames can be expressed by the Eulerian angle (ψ, ϕ, λ). Definition of the angles is given in Ref. 2. The normalized wave function Ψ_{JKM} has the explicit form;

$$\Psi_{JKM} = (-1)^{M-K}[(2J+1)/8\pi^2]^{\frac{1}{2}} D^J_{KM}(\psi,\theta,\phi) \ , \tag{2-10}$$

where D^J_{KM} is the rotational function, *i.e.*, the angular momentum eigen function.[2] The effect of an electric field on the molecular rotation (i.e., the Stark effect) can be calculated by the perturbation theory. The first order perturbation energy ΔW_1 is simply the average of the interaction energy for a given rotational quantum state, *i.e.*,

$$\begin{aligned} \Delta W_1 &= \int \Psi^*_{JKM}(\mu E\cos\theta)\Psi_{JKM}\, d\phi \sin\theta d\theta d\psi \\ &= \mu E\langle\cos\theta\rangle \end{aligned} \tag{2-11}$$

where $\langle\cos\theta\rangle$ is the quantum mechanical expectation value for $\cos\theta$, where θ is exact angle between M and E averaged over the rotational motion of the symmetric top molecule. Here, $\langle\cos\theta\rangle$ can be expressed as follows;

$$\langle \cos\theta \rangle = \int \Psi^{*}_{JKM}(\cos\theta)\Psi_{JKM} \sin\theta d\theta$$

$$\langle \cos\theta \rangle = KM/(J^2 + J) \tag{2-12}$$

Thus, there is exact agreement between the classical equation and the quantum mechanical equation.

The next approximation (the second order perturbation) takes into account small distortion of the wave function due to the electric field, and the resulting energy may be written as;

$$\Delta W_2 = \sum_{n'} \frac{|\mu_{nn'}|^2 E^2}{E_n - E_{n'}}$$

$$\Delta W_2 = \frac{\mu^2 E^2}{2Bh}\{\frac{(J^2 - K^2)(J^2 - M^2)}{J^3(2J-1)(2J+1)} - \frac{((J+1)^2 - K^2)((J+1)^2 - M^2)}{(J+1)^3(2J+1)(2J+3)}\} \tag{2-13}$$

As mentioned above, the first order Stark energy would be much larger than the second order Stark energy unless $K = 0$. However, as can be seen form the equation, the second order Stark effect would become important in the strong electric field or for the case with a prolate symmetric top molecule whose rotational constant B is generally small. Therefore, in this case, it is necessary to take into account the second order Stark effect.[3]

2-1.2 Rotational state selection by the hexapole electric field

By using a type of the Stern-Gerlach inhomogeneous electric field, the sign of

dipole moment can be reflected. Unfortunately, the deflection is too small, and the intensity would be too low to perform further experiments with the beam.

Electric hexapole field was invented to overcome this intensity limitation,.[4,5,6] This field consists of six rods, they are alternately charged and equally spaced on a circle centered about the beam axis. The form of equipotential surface in this field is given by,

$$V = V_0 (r / r_0)^3 \cos(3\phi) \tag{2-14}$$

where we take cylindrical coordinates (r, q, z) with z axis coinciding with the beam axis. The shortest distance between six surfaces of the rod and the z-axis is given by r_0. The absolute strength of the electric field expressed by,

$$E = 3V_0 r^2 / r_0^3 \tag{2-15}$$

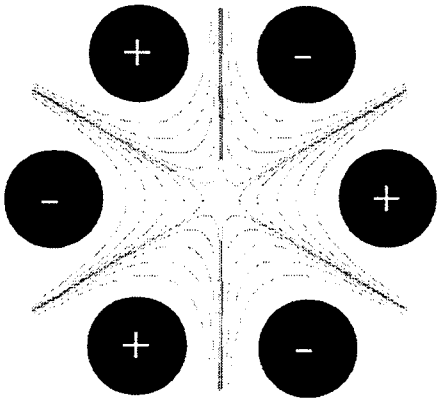

Figure 2-3. Equipotential in the hexapole field.

and does not depend on ϕ. This expression shows the field strength of the electric field inside of a hexapole. A schematic view of the equipotential in the hexapole field is shown in Fig. 2-3.

A polar symmetric top molecule in a rotational state with quantum number *J*, *K*, and *M*, moving in an electric field undergoes energy change due to the Stark effect. The potential energy depends only on the radial position *r*, and radial force is given by,

$$F = m\frac{d^2r}{dt^2} = -\frac{dW_{Stark}}{dr}$$
$$= -k_1 r - k_2 r^3 \qquad (2\text{-}16)$$

where *m* is a molecular weight, and k_1 ($= 6\mu V_0 \langle \cos\theta \rangle / R^3$) and k_2 ($= 18\mu^2 V_0^2 \Delta W_J / BhR^6$) are coefficients from the first and second Stark effect, respectively. A quantum mechanical treatment shows that $\cos\theta$ is quantized, but for all practical purposes we may regard it as continuous. The sign of the interaction depends on whether $\cos\theta$ is positive, zero, or negative. If a symmetric top molecule is put in an electric field, the molecule is forced to minimize its energy by reorienting itself in the field. The molecule with positive $\cos\theta$ will be defocused from the beam axis and those of negative values will be focused toward the beam axis, and long length-hexapole can be used for state separation without concomitant $1/r^2$ losses. Molecule with $\cos\theta = 0$ will not be deflected.

2-1.3 Size selection of neutral clusters

As have been seen so far, the focusing effect of polar symmetric top molecule in a hexapole field is preferentially determined via magnitude of the dipole moment, its molecular weight, and beam velocity. (molecular beam velocity is approximated to be identical to the carrier gas used.) Threshold voltage of hexapole to emerge a focusing effect is inversely proportional to the molecular weight under the assumption that every cluster has the same magnitude of dipole moment. This relationship can be easily derived from *Eq.* (2-17). Now let us consider applying this hexapole method to cluster beam whose size distribution is unity. Threshold voltage of focusing for a cluster is proportional to n, where n denotes the size of the cluster. This suggests that we can select single quantum rotational state for each cluster, cluster size selection achieves by scanning the hexapole voltage. We term the beam intensity dependence on V_0 as "focusing curve". Focusing curves of various size of clusters are depicted in Fig. 2-4.

While any molecular beam has a certain rotational distribution even in very cold rotational temperature which is rather easily attained by supersonic expansion, a

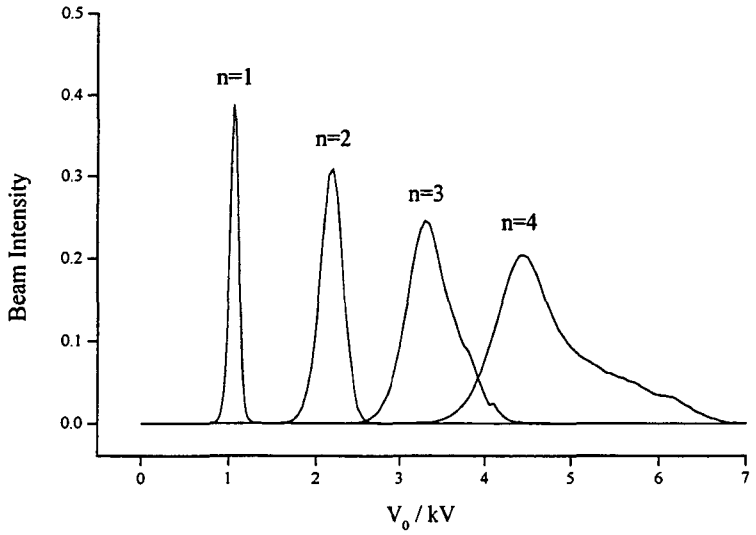

Figure 2-4. Simulated focusing curve for each cluster size.

focusing curve is likely to be composed of several rotational states contributions. This means that a focusing curve could become more complex and broader as shown in Fig. 2-6. Therefore, the focusing curve summed over all clusters could turn out to be extremely broad and some of quantum states are possibly overlapped with those of other size clusters. In order to examine such focusing overlap among rotational levels of whole clusters, we consider focusing of $J1M$ state for monomer and $J'1M'$ states for cluster of size n. For further simplicity, $J = M$ and $J' = M'$ are assumed. In practice, these states mainly contribute to the focusing curves. Since the second order Stark effect has smaller contribution, Stark force in the field is almost proportional to ρ / m.

$$\frac{\rho}{m} = \frac{\rho'}{mN}$$
$$\frac{1 \cdot J}{mJ(J+1)} = \frac{1 \cdot J'}{mNJ'(J'+1)} \qquad (2\text{-}17)$$

Then

$$J = N(J'+1) - 1 \qquad (2\text{-}18)$$

under this equation conserved, monomer state overlapping with that of other clusters can not be avoided. This result suggests that it seems quite difficult task to attain complete size selection by using an hexapole field technique. However, as we can measure focusing curve for each cluster size separately, we can change cluster size distribution only by changing the applied hexapole voltage. At each hexapole voltage, cluster distribution can be calculated from the focusing curve measurement for each

cluster size, yet. There is a limitation on this methodology. As mentioned above, threshold voltage of a focusing effect is proportional to cluster size. Hence, the difference between V_n and V_{n+1} decreases with increasing cluster size. This behavior is very similar to the limitation of time-of-flight mass spectrometry, because with TOF-MS, mass resolution becomes worse with increasing molecular weight to be analyzed.

2-1.4 Dipole moment determination

Focusing curve can be reproduced by calculations of exact trajectory in the hexapole field. Trajectory simulation can be carried out by simple point-by point calculation following classical Newton mechanics.[3,7] The radial portion was calculated with a 1-μs time step. Both the experimental and molecular parameters for this simulation are required. The velocity distribution of the molecular beam can be

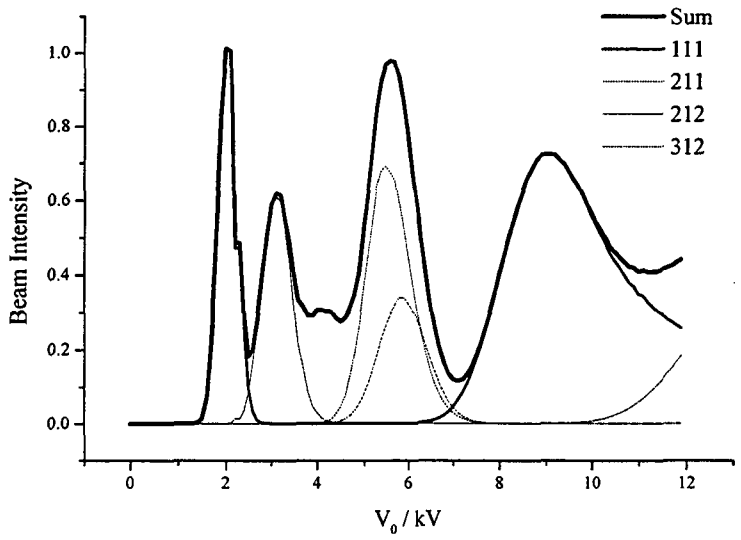

Figure 2-5. Simulated focusing curve of CH_3I. Rotational temperature is 3 K.

determined by TOF measurement. Rotational temperature which is also one of necessary parameters is assumed to be equivalent to experimentally determined translational temperature. In general, this rotational temperature is the only one parameter for fitting the focusing curve, and this result suggests that the assumption made above is always valid within experimental errors. When we measure a focusing curve for newly synthesized compound, dipole moment and rotational constants are required parameter to reproduce experimental focusing. Although threshold voltage only depends on the magnitude of dipole moment, this can be easily determined. On the other hand, in order to reproduce whole profile of the focusing curve, rotational constants also have to be taken into account.

2-2 Production of vdW and Hydrogen-Bonded Cluster Beam

In general, titled clusters have been produced in supersonic expansion from a nozzle source. It is known that the aperture size of a nozzle and shape determines the flow field gradients and, together with the conditions P_0 and T_0, the time scale of the expansion which is of prime importance for the condensation process. In addition, the area of a nozzle throat determines the mass flux through the nozzle and thus the pumping capacity of the vacuum system. The selection of a nozzle is not a unique process, but depends on the pumping system and on the desired cluster beam properties. A wide variety of the nozzle has been used for cluster source such as sonic nozzle, cylindrical nozzle, and conical nozzle. Sonic nozzle is preferred for studies on both molecular and small size cluster beam experiments. Conical nozzle is used to efficiently produce larger size cluster beam.

The next important component of nozzle is the control system for supply pressure P_0 and temperature T_0. Since the condensation process is very sensitive to both P_0 and T_0, careful control is necessary for cluster beam experiments.

Finally, practical technique associated with the nozzle source concerns the seed gas properties for the desired reactant gas. Rare gases, especially, Helium and Argon, are preferred to produce cluster beam effectively by collisional cooling.

2-3 Production of Organo-Metallic Cluster Beam

2-3.1 Laser Evaporation Method

When high power laser beam is tightly focused on solid metal surface, it is known to generate superheated plasma.[8] Typically, laser beam of 10 mm diameter with 5-50 mJ/pulse is focused onto from 0.5 to 1.0 mm in diameter. Making use of this phenomenon, any kinds of materials, such as metal, semiconductor, and insulator, can be vaporized. It should be noted that this method has potential advantage for extremely high boiling point metals like carbon, while heated oven can not attain sufficient vapor pressure. The second advantage of this method is its wide applicability to experiments. By the combination with molecular beam technique, not only pulsed atomic beam and cluster are produced, but also it is possible to produce variety of compounds, which can not be synthesized in usual circumstances because of its instability. In order to produce these atomic and molecular beams efficiently, it is necessary to cool down drastically plasma temperature by great amount employing the collisions with rare gases.

2-3.2 Laser source

A nano-second pulsed laser is used to produce superheated plasma. Specifically, second harmonic of Nd:YAG is one of the most commonly used sources, since it is visible and easy to align its laser beam path. Laser wavelength, generally, does not affect the production efficiency of plasma so much.

2-3.3 Cooling gas

It is well known that for producing neutral clusters, superheated plasma must be cooled efficiently.[9] For the sake of cooling down superheated plasma and confining the expanded vapor plume, pulsed rare gas injection is usually adopted, which has to be well adjusted with evaporation laser firing timing.[10] Due to the fact that various particles such as positive ions, negative ions, metastable atoms coexist in the initial superheated plasma, it is important for producing well cooled neutral species to optimize the timing between the plasma generation and cooling gas injection. This timing and injecting gas pressure depend on the geometry of laser evaporation source.

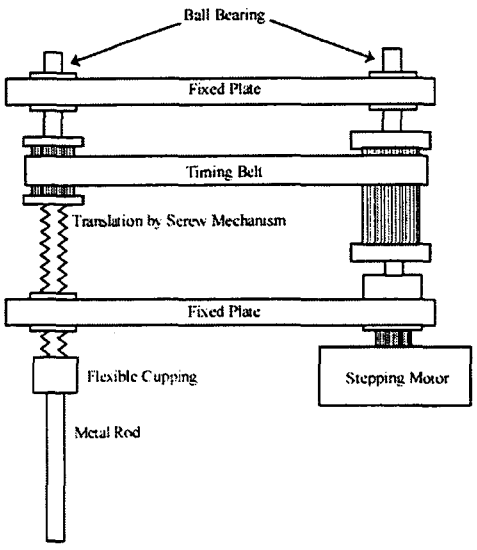

2-3.4 Solid metal sample

While a pulsed laser is continuously focused onto metal surface at one position, the efficiency for superheated plasma production decreases drastically with the accumulation of laser shots. In order to avoid this phenomenon and to keep the surface clean all the time(at each laser shot), a sample rod is designed to be rotated and translated by a screw mechanism immediately after each laser irradiation. This procedure works well for improving vaporized beam pulse-to-pulse reproductivity. The rod rotation has been induced by means of Poolly mechanism, regulated with a stepping motor shown above.

2-3.5 Reaction cell (channel) of the nozzle

After the production of metal atoms or clusters from the evaporation source, they move into a reaction channel and are mixed with reactant gases. The reactant gases are injected by another time-controlled pulse valve, and $(Metal)_n$-$(Reactant)_m$ clusters are produced. Unless metal beam is sufficiently cooled down, in some cases reactants may be decomposed. It is known that the size of product clusters depends on the length of this reaction channel.[11] Namely, the longer reaction channel, the larger clusters are formed.

2-3.6 Time correlation

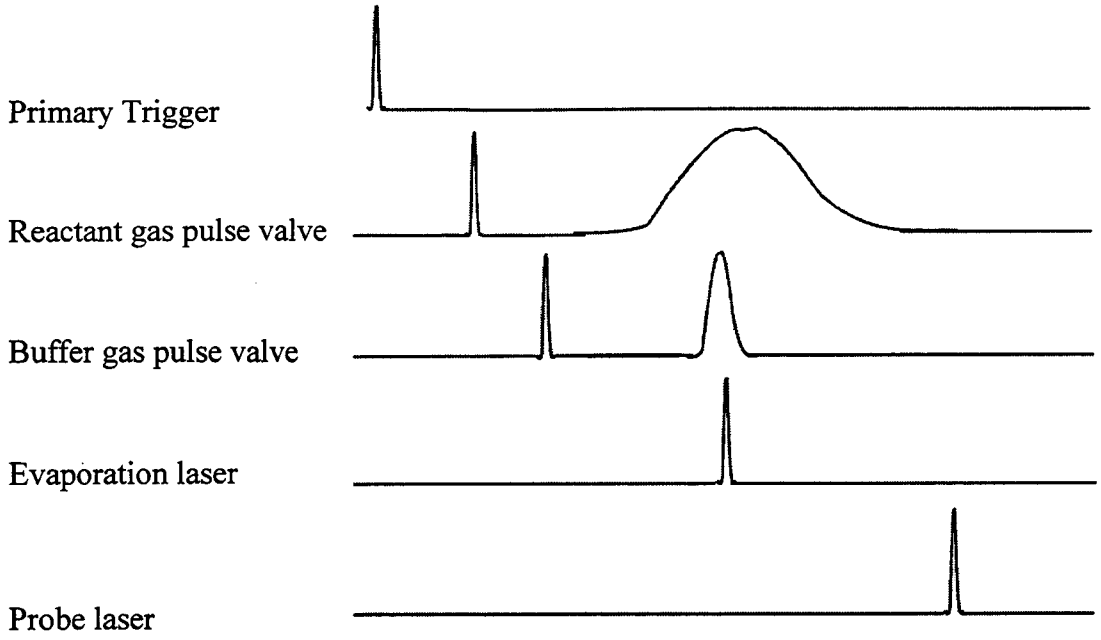

All the feeding pulses are synchronized by a digital delay generator, which is remote-controlled by a computer. Among these pulses, reactant gas injection is one of the most important, since reactant gas should be well homogeneously mixed with vaporized beam in order to produce mixed clusters efficiently. For this purpose, reactant gas should be injected into reaction cell before vaporized beam arrives, and long pulse duration is preferable.

2-3.7 Nozzle design

There have been reported various kinds of nozzle designs.[12,13,14,15] Most of them have been used to produce relatively larger clusters containing from two to several hundred atoms or molecules. First of all, we like to deal with small clusters such as binary complex. Therefore the nozzle was specially designed to produce only small clusters whose rotational and translational temperature would be sufficiently low.

Typical nozzle design to optimize production yield of small clusters is depicted in Fig. 2-6, several parameters were adjusted. The following figures show several characteristic parameters to be adjusted.

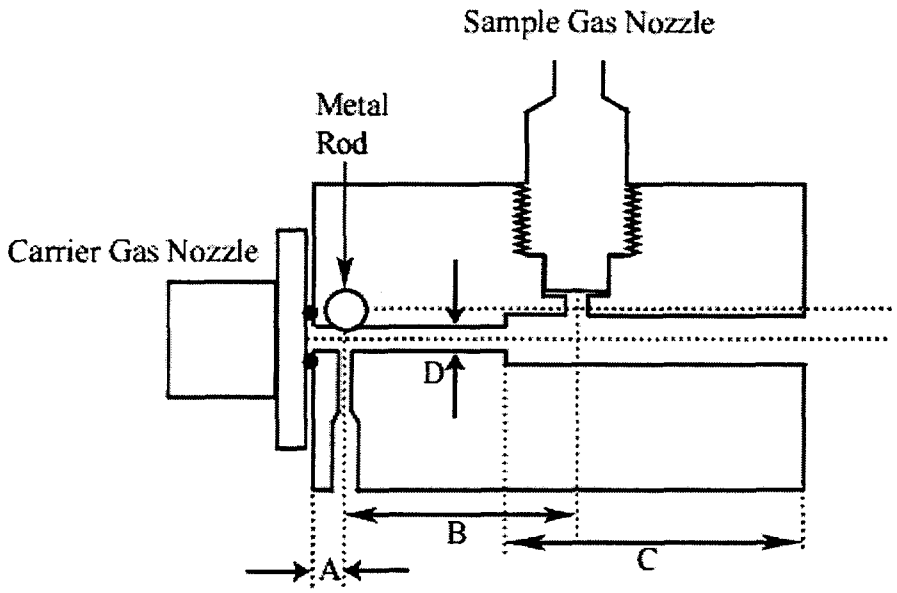

Figure 2-6. Schematic view of Nozzle source. Where *A* is the distance from valve to rod center, *B* the distance from rod to sample valve, *C* the reaction channel, and *D* denotes the throat diameter.

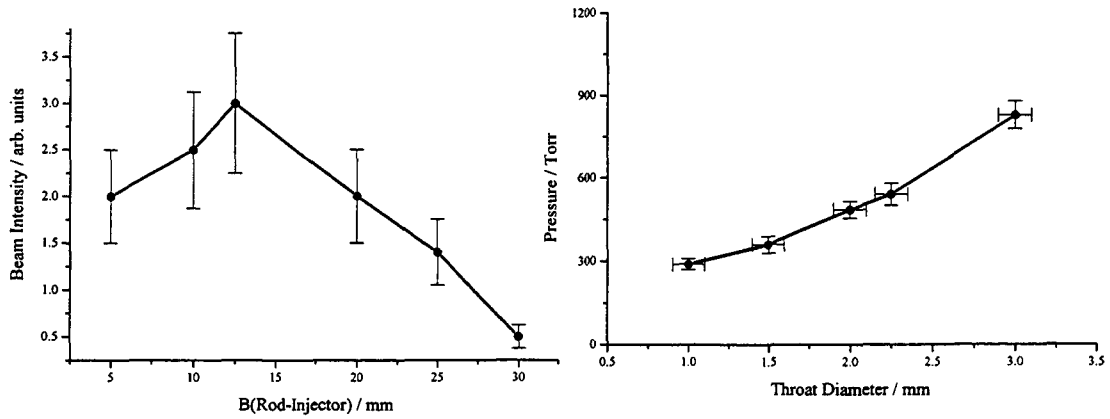

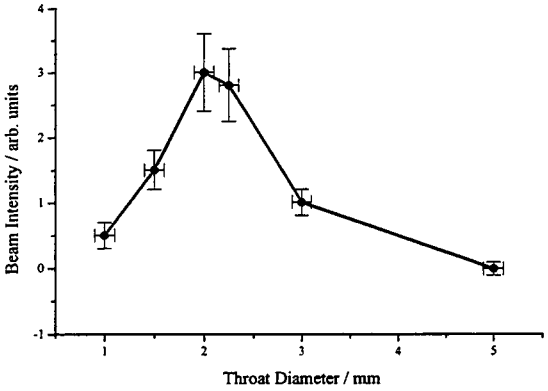
Beam Intensity / arb. units
Throat Diameter / mm

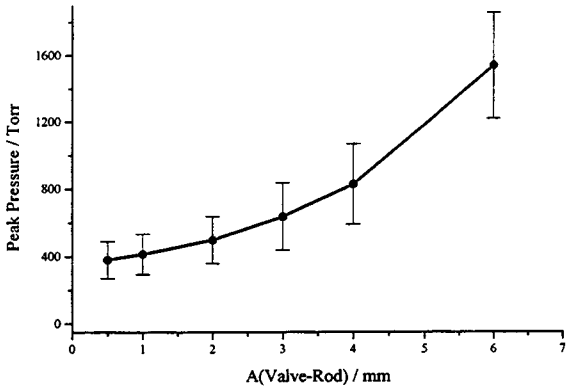
Peak Pressure / Torr
A(Valve-Rod) / mm

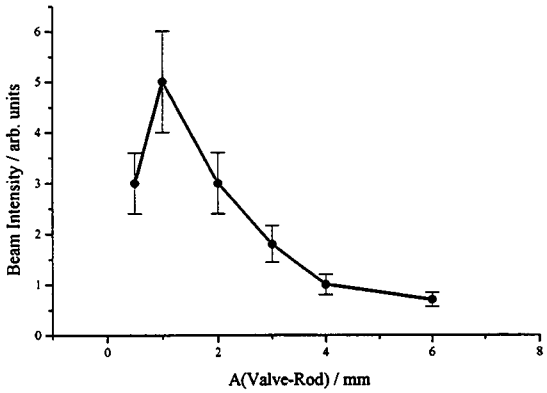
Beam Intensity / arb. units
A(Valve-Rod) / mm

2-4 *Production of Metastable Rare Gas Beam*

When rare-gas atomic beam is bombarded by thermal electrons, several ionic and electronically excited species may be produced. Some of the excited atoms will be de-excited through optical transition to the ground state. The rest of the excited atoms will remains in the same state from whose transition into the ground state is optically forbidden; in such case the excited atoms are subject to de-excitation only by collisions with other atoms. These atoms have a very long lifetime ranging from ms to seconds. These species are termed as metastable states. Heavy rare gases of the first electronic configuration $(n\text{-}1)p^5(n)s^1$ give a set of four states $^3P_{2,1,0}$ and $^1P_1$ in increasing order of energy. Radiative transitions from $^3P_1$ and $^1P_1$ states to the ground state are allowed and these states are termed resonance states. Transition from the triplet $^3P_2$ and $^3P_0$ states to the ground state are rigorously forbidden for electric dipole radiation. In this thesis, excited atoms in these states are referred as metastable atoms and are denoted by terms such as Ar^* and Ne^*. Generally, atomic beam through supersonic expansion has very long mean free path, then metastable atomic beam can be generated, since collisional relaxation processes in the beam are not likely.

A number of experimental methods have been reported to generate metastable beam, such as electron bombardment, glow discharge, and so on.[16] In this thesis, a glow discharge method was adopted for several advantages. The discharge source consists of a heated helical filament and a grid mesh. Typically, about 7 A dc-current is supplied to the filament and heated up to 1500 K and the grid potential is biased ranging from +40 to +120 V. Thermal electrons emerge from the filament surface and ejected to the grid. As a pulsed atomic beam passes between these two electrodes, electric discharge occurs,

which produces ion species, metastables, and so on. Ions are removed by reflector electrodes installed downstream. A major advantage of this method is that the design and set-up of the discharge source are easy and that its beam intensity of the obtained metastables is higher than usual other methods, and pulse-to-pulse instability is acceptable. Maximum metastable beam intensity is about 10^{16} atoms·$sr^{-1}s^{-1}$. Finally, the spin orbit ratios ($^3P_2$ / $^3P_0$) of metastable can be varied simply changing the biased grid voltage, while optical dumping method can be select one spin orbit state by tunable dye laser.[17]

2-5 (Laser Induced Fluorescence) LIF Measurement

Light emission from chemical reaction product directly reflects product internal state distributions, therefore it is a good criterion in order to reveal more detailed reaction mechanics. However, this method is only applicable to a molecule produced in electronically excited states. On the other hand, LIF method is a very powerful tool to investigate ground state products.[18,19] Recently, high resolution tunable dye lasers with wide spectral range have become commercially available, and LIF method has become a common tool not only in spectroscopical study but also reaction in dynamics study. The basic idea of LIF is simple. First, light from tunable laser is impinged on the sample to be investigated. As the wavelength of laser change, a molecule within the irradiated portion of sample will absorb a photon and will be excited to an allowed excited state. Since the molecules so excited are those in specific level by corresponding transition, the excitation is selective for this state. Hence, the excitation spectra of molecule as a function of wavelength reflect the relative population

of these different states. Deviation of the relative populations *n(v",J")* from excitation spectrum can be divided into two measurement regimes depending upon laser power.[20,21,22]

< Linear regime>

If the laser power is sufficiently weak not to saturate any transitions, can be calculated from the fluorescence intensity of the transition using the relation.

$$n(v'',J'') \propto \frac{I}{B \cdot P} \tag{2-19}$$

where B is the tabulated Einstein transition probability (proportional to both Hönl-London and Franck-Condon factors) for the absorption. P is the laser power.

<Saturation regime>

If the laser power is sufficiently strong to saturate all transitions, the population is directly proportional to fluorescence intensity, and is independent of laser or transition probability.

$$n(v'',J'') \propto I \tag{2-20}$$

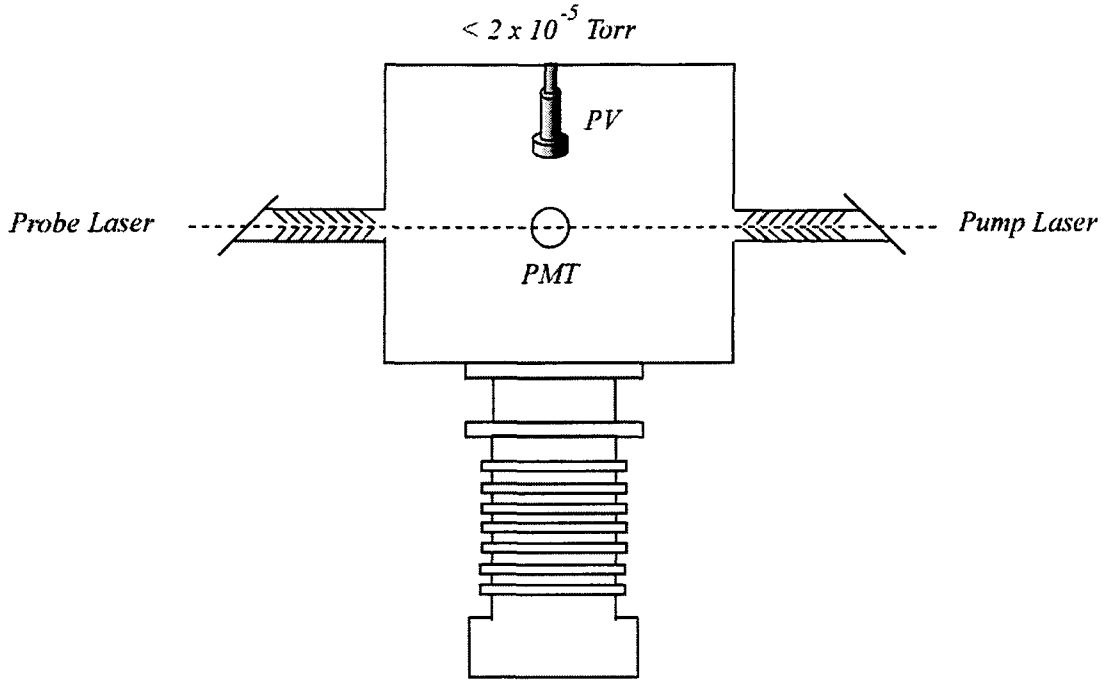

Figure 2-7. Typical setup for LIF measurement

A typical experimental apparatus for LIF measurement is shown in Fig. 2-7. The chamber (equipped with two buffle arms to reduce the scattered light) is evacuated by a diffusion pump, which usually produce a base pressure of lass than 10^{-5} Torr. Both ends of buffle arms have Brewster-angle windows in order to eliminate the scattered light from the windows. Sample gas will be introduced from the pulsed valve, which is synchronized with probe laser (LIF laser). Fluorescence from the molecule will be detected by a photomultiplier. A light collection mirror can also be installed, if necessary. At each wavelength, signals are accumulated to improve signal-to-noise ratio and stored in a computer.

2-6 Time of Flight Mass (TOF-MS) Spectrometer

The principle of operation of time-of-flight mass spectrometer is very simple.[23]

Significant advantage of this method is its multi-channel mass detection with high mass range. The ion transmission is almost independent of ion mass. This spectrometer consists of an ion source, ion lenses, and an ion detector separated by a drift region, respectively. Experimentally, first, an ion plume is produced by a laser light or electron bombardment. Ions are then accelerated by means of electrostatic field and are introduced to drift region, through which they travel until they are detected. An ion detector placed at the end of the drift tube receives ions with different masses at different time. The kinetic energy for all ions is almost the same and the velocity of each ion is inversely proportional to its mass. Arrival time of each ion can be expressed as,

$$t = D\sqrt{\frac{m}{2E}} \tag{2-21}$$

where D is a flight distance from ion source to the detector, m is the ion mass, and E is the kinetic energy of the accelerated ions. Time origin is set to the trigger pulse for ionization laser.

Resolution of TOF mass spectrometer is limited by both spatial divergence of the ionization region and the spread of ion velocities.[24,25] To achieve better mass resolution, it is necessary to ionize molecules or clusters within very short time at a specific location. This might be achieved by pulsed electron impact ionization or pulsed laser photoionization. In order to reduce the velocity spread resulting from the thermal distribution of the neutral target, the use of supersonic molecular beam is effective.

In this thesis, dual acceleration system was used to compensate for different arrival time of the same mass species due to relatively large ionization volume.

References

1. S.E. Choi, R.B. Bernstein, *J. Chem. Phys.*, **85**, 150 (1986).
2. C.H. Townes, A.L. Schawlow, "*Microwave Spectroscopy*", Dover, 1975.
3. H. Ohoyama, T. Ogawa, T. Kasai, *J. Phys. Chem.*, **99**, 13606, (1995); T. Kasai, T. Matsunami, T. Fukawa, H. Ohoyama, K. Kuwata, *Phys. Rev. Lett.*, **70**, 3864 (1993); K. Kuwata, T. Kasai, in: K. Liu, A. Wagner, Eds. "*The Chemical Reaction Dynamics and Kinetics of Small Radicals*", in Advanced Series in Physical Chemistry, Vol. **6**, Word Scientific, 1993.
4. P.R. Brooks, *Science*, **193**, 11 (1976).
5. H.G. Bennewitz, W.Paul, C.H. Schlier, *Z. Phys.*, **141**, 6 (1955).
6. K.H. Kramer, R.B. Bernstein, *J. Chem. Phys.*, **42**, 767 (1965).
7. R.W. Anderson, *J. Phys. Chem. A* **101**, 7664 (1997).
8. E.S. Marmar, J.L. Cecchi, S.A. Cohen, *Rev. Sci. Instrum.*, **46**, 1149 (1975).
9. M.R. Zakin, D.M. Cox, A. Kalder, *J. Phys. Chem.*, **91**, 5224 (1987).
10. R.J. St. Pierre, M.A. El-Sayed, *J. Phys. Chem.*, **91**, 763 (1987).
11. K. Hoshino, T. Kurikawa, H. Takeda, A. Nakajima, K. Kaya, *J. Phys. Chem.*, **99**, 3053 (1995).
12. P. Weiss, P.R. Kemper, M.T. Bowers, *J. Phys. Chem.*, **101**, 8207 (1997).
13. Y.A. Yang, P. Xia, A.L. Junkin, L.A. Bloomfield, *Phys. Rev. Lett.*, **66**, 1205 (1991).
14. K. Ohoshimo, H. Tsunoyama, Y. Yamakita, F. Misaizu, K. Ohno, *Chem. Phys. Lett.*, **301**, 356 (1999).
15. D.E. Powers, S.G. Hansen, M.E. Geusic, A.C. Puiu, J.B. Hopkins, T.G. Dietz, M.A. Duncan, P.R.R. Langridge-Smith, R.E. Smalley, *J. Phys. Chem.*, **86**, 2556 (1982).

16. D.H. Stedman, D.W. Setser, *Progress in Reaction Kinetics*, Pergamon Press, 1971.

17. K. Imura, R. Midorikawa, T. Kasai, H. Ohoyama, D.C. Che, *Chem. Letters*, **299** (1996).

18. J.L. Kinsey, *Ann. Rev. Chem.*, **28**, 349 (1977).

19. P.J. Dagdigian and R.N. Zare, *Science*, **185**, 739 (1974).

20. W.M. Fairbank, T.W. Hansen, A.L. Schawlow, *J. Opt. Soc. Am.*, **65**, 199 (1975).

21. P.J. Dagdigian and R.N. Zare, *J. Chem. Phys.*, **61**, 2464 (1974).

22. P. Andresen, G.S. Ondrey, B. Titze, E.W. Rothe, *J. Chem. Phys.*, **80**, 2548 (1984).

23. K. Rinnen, D.A. Kliner, R.S. Blake, R.N. Zare, *Rev. Sci. Instrum.*, **60**, 717 (1989).

24. D.S. Cornett, M. Pescheke, K. LaiHing, P.Y. Cheng, K.F. Willey, M.A. Duncan, *Rev. Sci. Instrum.*, **63**, 2177 (1992).

25. D.M. Lubman, W.E. Bell, M.N. Krinick, *Anal. Chem.*, **55**, 1437 (1983).

Structures of Small Clusters

Focusing of DCl and HCl dimers by an electrostatic hexapole field: The role of tunneling motion

3-1 Introduction

Since the hydrogen bonding is of major importance in chemistry and also biology, the ability to investigate its properties in a microscopic system is of interest. One of the good instances of hydrogen bond in chemistry is the elevated boiling point of the first-raw hydride, which has been attributed to their enhanced hydrogen bonding power. Hydrogen bonded dimers like $(HX)_2$ when X=F, Cl serve as paradigms for hydrogen bonding. The molecular beam method has made it possible to investigate these complexes, by applying a large variety of methods that include IR and far IR spectroscopy, mass spectroscopy and more.[1,2] Specially, the dipole moment of $(HF)_2$ has been measured experimentally in a molecular beam, as well as calculated theoretically. A DC electric field has been used to quench the tunneling in the HF dimer.[3] However, in case of $(HCl)_2$, direct measurement of the dipole moment has never been performed, although it has been calculated.[4]

Recently, the relationship between the structure and dynamics in floppy systems is a subject that has focused much attention. Specifically the "geared interconversion" of hydrogen bonded dimers such as $(HCl)_2$, $(DCl)_2$, and $(HF)_2$ have been studied extensively both experimentally and theoretically. Most of the experimental studies focused on the spectroscopy of these species, from which the tunneling splitting could be extracted. One of the IR studies suggested that when one of the cluster moiety in the heterodimer, $H^{35}Cl$-$H^{37}Cl$ was vibrationally excited, large

amplitude internal rotor motion was quenched effectively and elevate the dimer from a rapidly tunneling species into a state frozen into one of the two possible quasi-rigid structures. In addition, very recently, the first order Stark effect was obtained in the IR spectrum of the heterodimers $H^{35}Cl$-$H^{37}Cl$ in $K = 1$, while the heterodimers in $K = 0$ show a second order Stark effect.[5]

In order to determine the electric dipole moment and to differentiate between the hetero- and homodimers, we have performed focusing curve measurements of these species with 60 and 210 cm long hexapoles, so that the field applied is smaller for longer one. In addition, the DCl dimers were investigated in order to elucidate the isotope effect on this tunneling motion.

Rank et al.[6] were the first to observe spectroscopically the HCl dimer. They identified it via the presence of new vibrational structures in the infrared spectrum of the HCl monomer. The rotational spectrum of $(HCl)_2$ was observed in the near-infrared region by Pine and Ohashi, who studied the dimers with Doppler-limited resolution using a long-path cell cooled to 130 K.[7] Their rotational analysis of the *K*-subband structure suggested a nearly L-shaped structure for $(HCl)_2$ as schematically shown in Fig. 3-1. The equilibrium geometry of the dimer,[8,9,10,11,12,13,14,15] as well as the nature of the intramolecular hydrogen motion have also been determined by various experiments

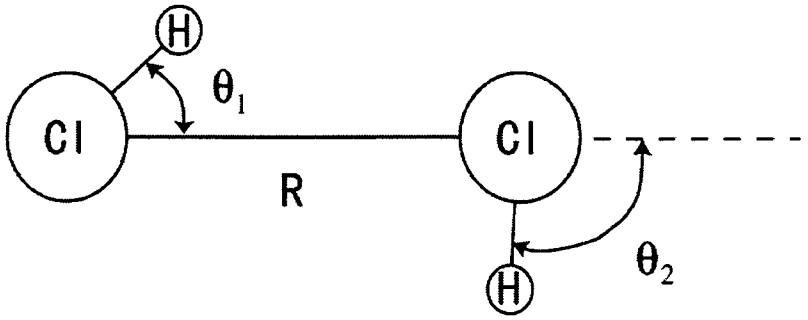

Fig. 3-1. The equilibrium structure of the HCl dimer as suggested in Ref. 22. $R = 3.746$ Å, $\theta_1 = 9°$, and $\theta_2 = 89.8°$.

and calculations.[16,17,18,19]

Recently, considerable emphasis has been placed on studying the tunneling motion in $(HCl)_2$, which corresponds to the proton interchange between the bonds.[20,21,22,23,24,25] It was suggested that there is a splitting of about 3–15 cm^{-1} in the dimer spectrum, which indicates a tunneling time in the range of picoseconds.[26]

The $(DCl)_2$ dimer, on the contrary, has been less studied, partly due to the difficulty for probing intra- and intermolecular vibrational spectra. Schuder et al.,[17] however, have measured the high-resolution spectra of $(DCl)_2$ in the near-IR region and provided accurate tunneling splitting constants for all ^{35}Cl and ^{37}Cl isotopomers. It was found that the tunneling motion slows down significantly when the dimers are excited vibrationally and the effect is especially pronounced for the heterodimers. The two-state model predicts that the two tunneling states, which are vibrationally excited, can be distinguishable in structures, such as $D^{35}Cl$–$D^{37}Cl$ and $D^{37}Cl$–$D^{35}Cl$. A detailed comparison between the dimers of HCl and DCl would provide further insight into the large amplitude nature of low-frequency geared-tunneling motions because deuterium substitution should provide a strong isotope effect on the tunneling rate. In the case of $(HF)_2$ and $(DF)_2$, the tunneling splitting decreases by 12-fold by deuteration, whereas the tunneling splitting showed less than a threefold decrease in the case of $(HCl)_2$ and $(DCl)_2$.

3-2 Experimental

Schematic view of the apparatus for rotational state selection with a 2-m-long hexapole field is shown in Fig. 3-2. The apparatus employed in the present study

consists of four vacuum chambers, which are differentially pumped; i.e., nozzle, buffer, hexapole field, and mass spectrometer chambers. The HCl cluster beam, with 400 μs

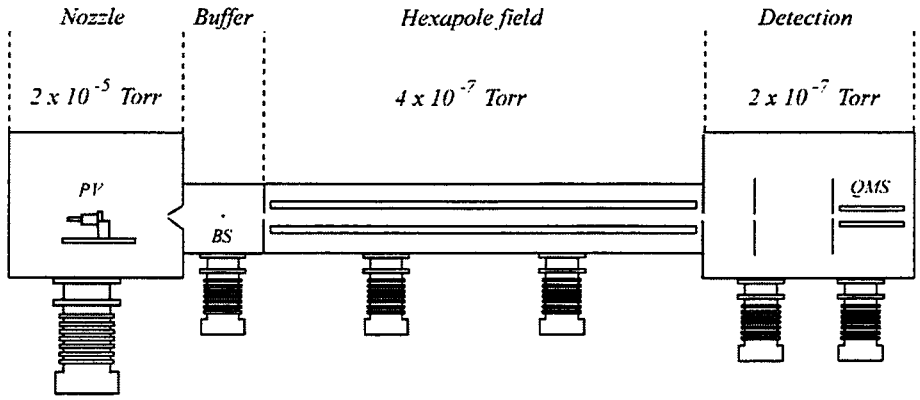

Fig. 3-2. Schematic view of the experimental setup.

pulse length emerged from a 0.8 mm diam nozzle. It was produced by supersonic expansion of neat HCl (99.9%) at stagnation pressures from 300 to 700 Torr. The DCl cluster beam was generated from DCl gas (Matheson, purity of 99.5 vol. %), without seeding, at a stagnation pressure ranging from P_0 = 150–1100 Torr. The cluster beam was skimmed by a 1 mm diam skimmer at a distance of 42 mm downstream from the nozzle. In the buffer chamber, either a molecular beam stop with 1.2 mm diam. was installed for the focusing experiments or a chopper wheel was placed for the time-of-flight (TOF) measurements. The velocity distribution of the $(HCl)_2$ beam $g(v)$ is described by the following expression:[27]

$$g(v) \propto v^2 \exp[-(v - v_s)^2 / \alpha_s^2] \tag{3-1}$$

$$\alpha_s = (2kT/m)^{\frac{1}{2}} \tag{3-2}$$

where V_s is the stream velocity, k is the Boltzmann factor, and T is the translational

temperature. From the TOF experiments it was found that for the HCl dimer, V_s = 625 ± 10 ms^{-1} and α_s = 65 ± 10 ms^{-1}. These values hold for the major portion of the pulsed beam, since at the beginning and at the end of the pulse the beam characteristics vary. The detection system was gated so that measurements were performed only on the central portion of the beam pulse.

Since the HCl and DCl dimer rotates with respect to the Cl–Cl axis, it can be treated as a symmetric top. Thus, the $|JKM\rangle$ rotational states of $(DCl)_2$ can be selected and focused by the hexapole field. The dimer was selectively measured with a quadruple mass spectrometer by monitoring either the parent peak (m/e = 74) or the protonated peak (m/e = 39). For the parent peak, the mass resolution Δm was set as + 2 due to the weak beam intensity. Therefore, it was not possible to separate the peaks of $D^{35}Cl$–$D^{35}Cl$ and $D^{37}Cl$–$D^{35}Cl$. The focused beam was detected by the mass spectrometer through a 1.5-mm inlet aperture. The signal from the mass spectrometer was stored as a time-profile signal in a transient memory. The voltage (V_0) on the hexapole rods was varied from 0 to 12 kV. Typically, 10^4 time profiles were accumulated at each V_0. The same experimental parameters were also used in the trajectory simulation and are shown in Table 3-1.

Table 3-1. Experimental parameters for 210-cm-long that were applied in the simulation of the focusing curve for the HCl and DCl dimers

	Radius / mm	Distance from the nozzle / mm
Skimmer	1.0	45
Beam stop	1.0	235
Collimator	5.0	293
Hexapole inlet	7.0	374
Hexapole outlet	7.0	2483
Collimator	1.5	2930
Detection point	1.5	2948

3-3 Results and Discussion

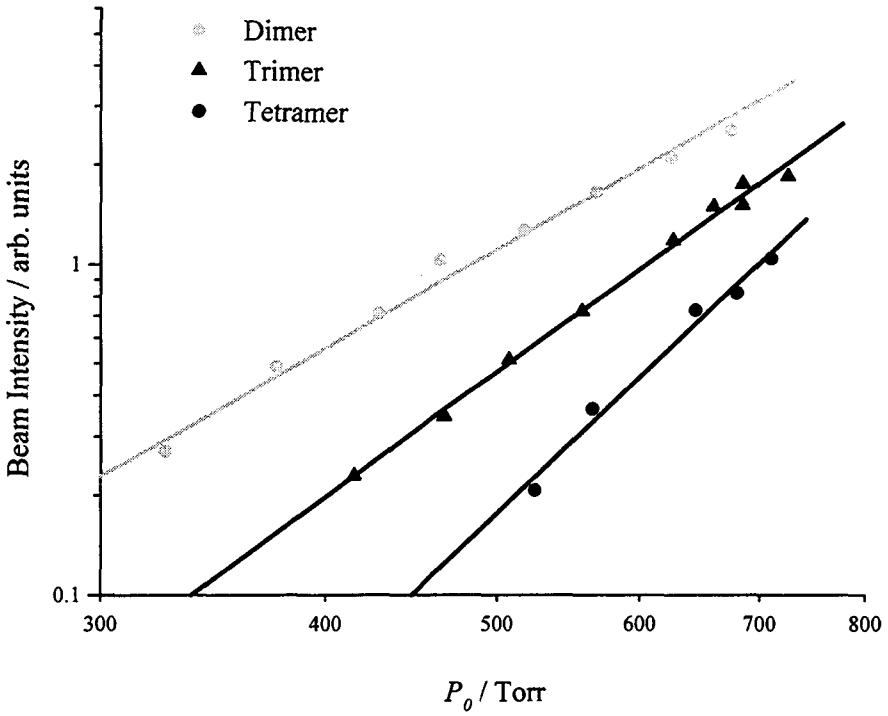

Figure 3-3. Logarithmic plots of the $(HCl)_n^+$ (n = 2-4) beam intensities versus the stagnation pressure P_0. All the data were obtained at an electron impact energy of 62.4 eV.

Figure 3-3 shows the dependence of the mass spectrometer signal intensity on the stagnation pressure of neat HCl (P_0), for the three parent ion peaks corresponding to the HCl dimer, trimer, and tetrameter; i.e. $(HCl)_n^+$ ions (n = 2-4). The $(HCl)_4^+$ ion was the largest cluster that could be detected by the present mass spectrometer. For each cluster of size n, the dependence of the signal on the stagnation pressure, P_0, shows an exponential dependence of nth order, indicating a good agreement with the P_0^n scaling law in the pressure region from 400 to 700 Torr. There fore, it is reasonable to assume that the signal observed at a mass corresponding to the $(HCl)_n^+$ cluster originated mostly

from the corresponding neutral clusters $(HCl)_n$ (n = 2-4).

It is know that van der Waals clusters, which are characterized by weak intermolecular bonds, suffer fragmentation due to electron bombardment in the ion source. On the other hand, hydrogen bonded clusters are characterized by much less fragmentation; however, they form protonated-type cluster ions. Recently, Wittig and co-workers reported that in case of $(HCl)_n$ clusters, non-protonated cluster ions were also observed at the mass corresponding to $(HCl)_n^+$ in accord with our observation.

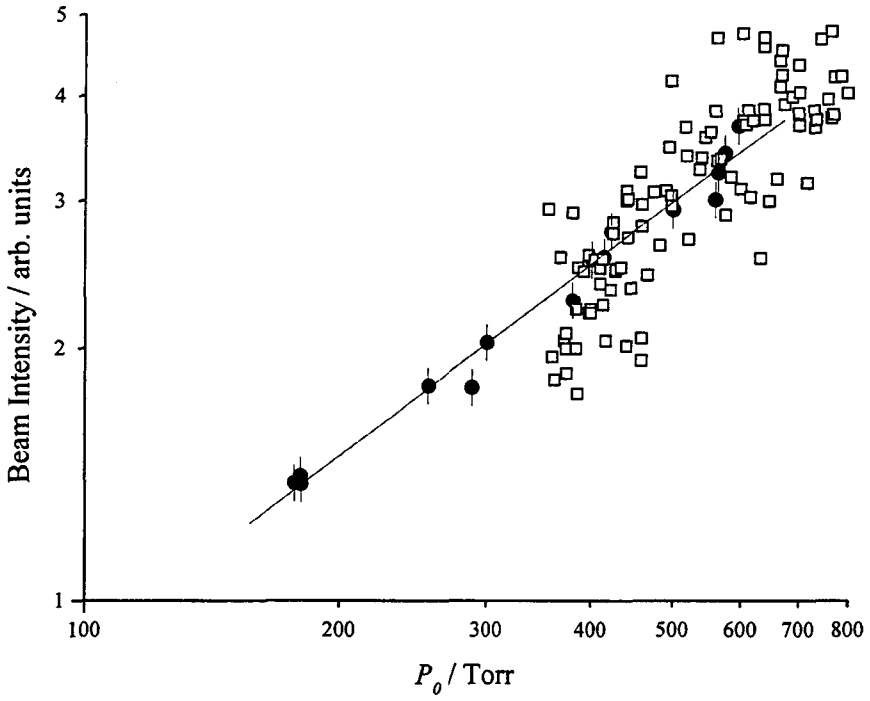

Figure 3-4. The dependence of the beam intensity on the DCl stagnation pressure when the mass spectrometer monitored m/e = 74 ± 2 (open circles) and m/e = 39 ± 1 (solid circles). The solid line indicates a slope of 2.

Figure 3-4 shows the dependence of the beam intensity for the $(DCl)_2$ dimer on the DCl stagnation pressure (P_0). The mass spectrometer was tuned either to m/e = 74 for $(DCl)_2$ with mass resolution of Δm = 2 (the open circles), or to m/e = 39 for the protonated ion peak of D_2Cl (the solid circles) with the mass resolution (Δm = 1). It was

found that the observed points nicely lay on the line with a slope of 2, which confirms that the mass signals at *m/e* = 39 and 74 are mostly due to $(DCl)_2$, and they also reflect the scaling law. Hence, we chose to measure the *m/e* = 39 peak intensity to obtain the focusing curve for the DCl dimers.

Focusing curve measurement of HCl dimer with 60-cm long hexapole

In the focusing experiment, the stagnation pressure of neat HCl gas was held constant at 400 Torr. This pressure was chosen because it was shown experimentally that at this pressure the only cluster in the beam is the dimer, and no larger HCl clusters could be detected. In this measurement, the beam-stop was inserted in front of the

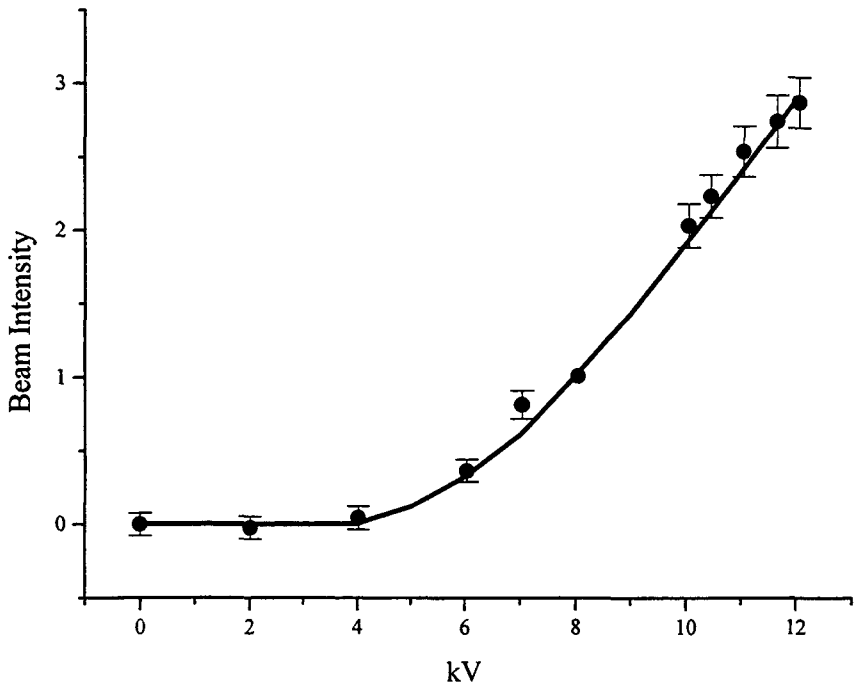

Figure 3-5. Focusing curve of the HCl dimer produced at a stagnation pressure of 400 Torr (dots). The simulated curve is shown as a solid line.

hexapole rods to execute the direct beam, namely to bock those species that are not affected by the hexapole field. Figure 3-5 represents the observed focusing curve for the HCl dimer. It is obtained by monitoring the dependence of the dimer signal intensity on the hexapole field, V_0, after subtracting the background signal, namely the signal observed at $V_0 = 0$. The background signal is mainly because of dimers that by-pass the beam stopper due to slight misalignment of the beam stop relative to the molecular beam. Vertical scale in Fig. 3-5 is normalized to 8.0 kV. The observed curve clearly shows that the beam intensity is enhanced, as hexapole rod voltage increases. The enhancement of the signal at 12 kV is about 20% relative to the back-ground signal.

It was suggested that fast tunneling between the donor-acceptor configuration occurs in the ground state of dimer, which leads to a splitting of about 15 cm^{-1} between the symmetric and anti-symmetric states. If the focused species indeed undergo such tunneling, the structure has to be averaged properly, as was done of ammonia in a hexapole field. We tried to simulate the data in Fig. 3-5, assuming that tunneling occurs, and found that it could be simulated only by using an unreasonably large value for the dipole moment. However, this is quite unlikely. On the other hand, the data can be reproduced very nicely by a trajectory simulation assuming the first order Stark effect of symmetric top molecule with 1.5 D dipole moment. These results may suggest that either electric field quenched the tunneling, as was observed for $(HF)_2$, or some of the HCl dimers are deflected by the hexapole field and shows first order Stark effect.

In order to differentiate these possibilities, we performed same measurement with longer hexapole, so that field applied is smaller.

Focusing curve measurement with 210-cm long hexapole

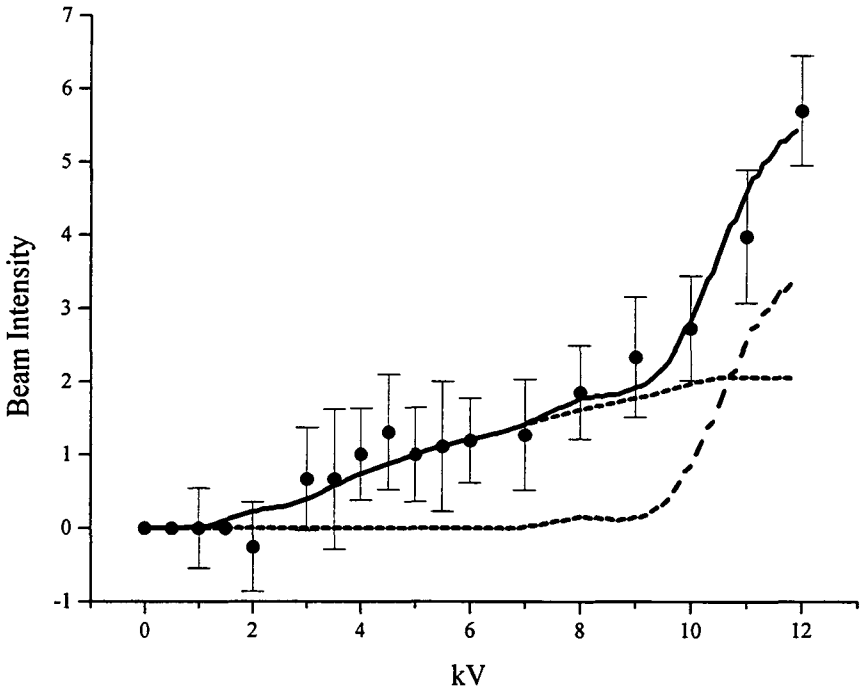

Figure 3-6. The measured beam intensity as a function of the potential on the hexapole (V_0) (close circles) measured at m/e = 39 for a beam of DCl. The results from simulation assuming the first-order Stark effect and a dipole moment of 1.5 D are shown as a dotted line. The results from a simulation based on *Eq.* (3-3) and assuming a dipole moment of 1.5 D is shown as a dashed line. The solid line in the sum obtained by adding the contribution from the two simulations.

Figure 3-6 shows the experimental focusing curve, namely, the dependence of the DCl dimer beam intensity on V_0, when the m/e = 39 peak intensity (solid circles) was monitored. The stagnation pressure of the DCl gas was 380 Torr, which results in the beam containing only monomers and dimers. Starting from about V_0 = 2 kV there is a constant increase in the beam intensity as a function of the hexapole field. After V_0 = 10 kV the slope increases. The dotted line in Fig. 3-6 presents the results from the trajectory simulation assuming the first-order Stark effect, namely, that the dimer is a

symmetric top with a permanent dipole moment of 1.5 D. Clearly, the calculated curve shows a significant discrepancy from the experimental observations for V_0 larger than 10 kV.

If we assume that the species focused undergo rapid tunneling motion between two configurations both with the same nominal dipole moment, but with opposite sign, as in the well-known case of NH_3, than *Eq.* (3-3) represents the force in the hexapole field:

$$F = m\frac{d^2r}{dt^2} = -\frac{dW_{Stark}}{dr}$$
$$= \mp \frac{\left(\frac{6\mu_{as}V_0}{R}\right)^2 r^3}{\left[(W_a - W_s)^2 + \left(\frac{6\mu_{as}V_0}{R}\right)^2 r^4\right]^{1/2}} \qquad (3\text{-}3)$$

When $\mu_{as} = KM/J(J+1)$ (is the nominal dipole moment of the species focused), $W_a - W_s$ is the tunneling splitting as obtained from spectroscopy, and R is the radius of the path between the hexapole rods. Assuming a nominal dipole moment of 1.5 D and tunneling splitting of 5.96 cm^{-1},[1,17] the dashed line in Fig. 3-6 was obtained.

The experimental curve in Fig. 3-6 could simulate accurately, assuming the focusing of two species. One is a symmetric top system with a dipole moment of 1.5 D, and the other with a contribution of 20–40 times larger, is a species that undergoes fast tunneling. In the simulation the rotational temperature was assumed to be 18 K, and *JKM* states up to $J = 12$, $K = 1, 2$ were taken into account.

The results can be rationalized if we assume that at $m/e = 39$ we detect two

species: $D^{37}Cl^+$ and DCl^+. The first is a fragment mainly from the heterodimer $D^{35}Cl$–$D^{37}Cl$ while the second results mainly from the homodimer $(D^{35}Cl)_2$. Hence, due to the breaking of symmetry, the heterodimer can be treated as a symmetric top species with a permanent dipole moment which is focused at lower V_0, while in the homodimer fast tunneling occurs and it is focused only at $V_0 > 10$ kV. The obtained dipole moment of 1.5 D agrees with the value determined at shorter hexapole. Therefore, the possibility that the electric field quench the tunneling can be ruled out.

The ratio between the dimers that are focused by the first-order Stark effect to that focused by second-order Stark effect is 1 to about 20–40. Since the ratio between the hetero-to-homodimers is 1:1.5, this means that not all heterodimers can be focused by the first-order Stark effect, and actually only one out of about ten molecules is focused. This difference may result from the possibility that the tunneling in the heterodimer is suppressed only for specific *JKM* state.[28]

The same setup has been used to focus HCl dimers. In this case, the mass spectrometer was set for $m/e = 72 \pm 2$ and the results shown in Fig. 3-7 were obtained. The data could be simulated by assuming the first-order Stark effect, rotational temperature of 18 K, dipole moment of 1.5 D, and rotational states up to $J = 12$ and $K = 1, 2$ were taken into account. Unlike in Fig. 3-6, no contribution due to species with fast tunneling could be observed.

The results can be rationalized if we assume that the species observed is $^{35}Cl^{37}Cl^+$, which is a fragment from the heterodimer of HCl. The fact that no homodimer can be focused is probably due to the large tunneling splitting in this system, which indicates a very fast tunneling rate.

The results observed in the case of the DCl dimers shed new light on the former results obtained for the HCl dimers. In both cases the observed dipole moment is the same, within the experimental accuracy, as expected. Based on the interpretation of the spectroscopy, one would not expect to observe the first-order Stark effect even in the case of the heterodimer. The tunneling splitting observed spectroscopically in the

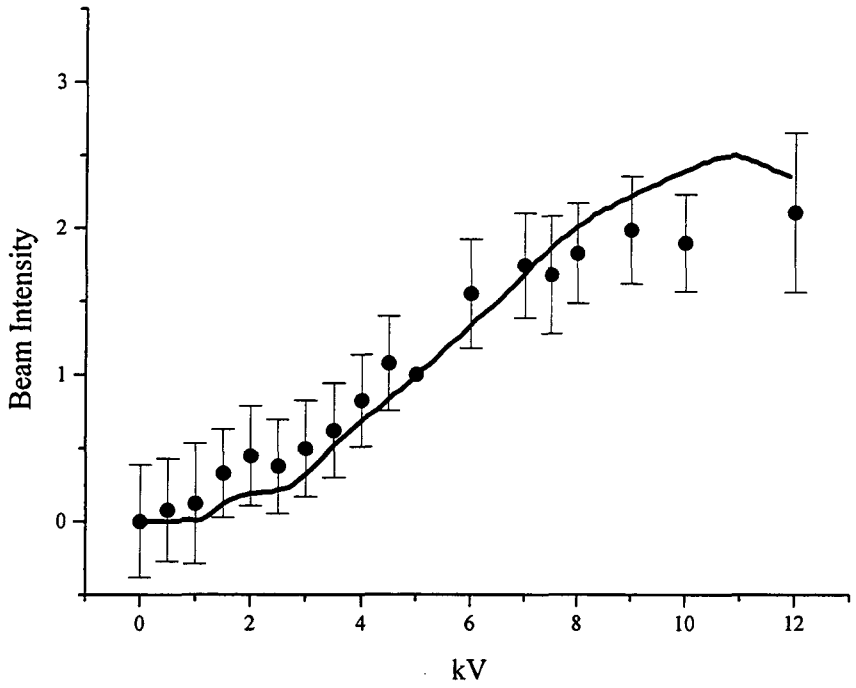

Figure 3-7. The measured beam intensity as a function of the potential on the hexapole (V_0) (close circles) measured at m/e = 72 for a beam of HCl. The solid line is the result of the simulation assuming a dipole moment of 1.5 and rotational temperature of 18 K.

case of the heterodimers (both for HCl and DCl) may hint that despite the breaking of the symmetry in the case of the heterodimer, the tunneling rates are not affected. However, the observation of the first-order Stark effect for the heterodimer means that for those species no tunneling occurs. The apparent contradiction may be explained by reinterpretation of the spectroscopic results based on a model presented recently.[30]

According to this model, the actual splitting related to the tunneling motion is very small (a fraction of a wave number) and the splitting observed in the spectroscopy has a different origin. The fact that the hexapole is observed only in the case of the heterodimer is due to the removal of the permutational symmetry in the heterodimer that allows the observation of a permanent dipole moment.

Vector summation of the dipole of the monomers, assuming the structure presented in Fig. 3-1, gives a value of about 1.14 D for the parallel component of the dipole moment. This value is significantly lower than the one obtained experimentally. All calculations indicate that upon formation of the dimer, negative charge is transferred from the hydrogen to the chlorine. Hence, they predict a larger parallel component for the dimer than the vector sum of the monomers. In recent ab initio calculations the dipole moment of the dimer, in its equilibrium configuration was calculated to be 1.37 D.[29] The experimental results indicate that the polarization if the HCl moieties in the dimer is slightly larger than that obtained form calculation.

3-4 Conclusion

The focusing of HCl and DCl dimers was observed using an electrostatic hexapole field. The results indicate the existence of two types of species. The first is the homodimers, either the $H^{35}Cl$–$H^{35}Cl$ or the $D^{35}Cl$–$D^{35}Cl$, for which the data indicate a fast tunneling motion. The second is the heterodimers, $H^{35}Cl$–$H^{37}Cl$ or $D^{35}Cl$–$D^{37}Cl$, that do not show evidence for significant tunneling motion on the time scale of the experiment. In the case of HCl dimers, even at relatively high fields, only one species could be focused, the heterodimer. The electric dipole moments for both $(DCl)_2$

isotopomers were determined to be 1.5 ± 0.2 D, which is the same value as observed for $(HCl)_2$.

References

1. J.F. Garvey and R.B. Bernstein, *Chem. Phys. Lett.*, **143**, 13 (1998).
2. H. Shinohara and N. Nishi, *Chem. Phys. Lett.*, **87**, 561 (1982).
3. R.J. Bemish, M.C. Chan, R.E. Miller, *Chem. Phys. Lett.*, **251**, 182 (1996).
4. C.E. Dykstra, *J. Phys. Chem.*, **99**, 11680 (1995).
5. R. Miller (private communication).
6. D. H. Rank, P. Sitaram, W. A. Glickman, and T. A. Wiggins, *J. Chem. Phys.* **39**, 2673 (1963); D. H. Rank, W. A. Glickman, and T. A. Wiggins, *J. Chem. Phys.*, **43**, 1304 (1965).
7. N. Ohashi and A. S. Pine, *J. Phys. Chem.* **81**, 73 (1984); A. S. Pine and B. J. Howard, **84**, 590 (1986).
8. P. Hobza, P. Carsky, and R. Zahradnic, *Collect. Czech. Chem. Commun.* **44**, 458 (1979); P. Hobza and J. Sauer, *Theor. Chim. Acta* **65**, 279 (1984).
9. M. Allavena, B. Silvi, and J. Cipriani, *J. Chem. Phys.* **76**, 4573 (1982).
10. C. Votava, R. Ahlirichs, and A. Geiger, *J. Chem. Phys.* **78**, 6841 (1983).
11. I. M. Mills, *J. Phys. Chem.* **88**, 532 (1984).
12. M. J. Frisch, J. A. Pople, and J. E. Del Bene, *J. Phys. Chem.* **89**, 3664 (1985).
13. Z. Latajka and S. Scheiner, *Chem. Phys.* **122**, 413 (1988).
14. S. Liu and C. E. Dykstra, *J. Phys. Chem.* **90**, 3097 (1986).
15. F.-M. Tao and W. Klemperer, *J. Chem. Phys.* **101**, 1129 (1994); **103**, 950 (1995).
16. G. A. Blake and R. E. Bumgarner, *J. Chem. Phys.* **91**, 7300 (1989).
17. M. D. Schuder, C. M. Lovejoy, D. D. Nelson, Jr., and D. J. Nesbitt, *J. Chem. Phys.* **91**, 4418 (1989).

18. M. J. Elrod and R. J. Saykally, *J. Chem. Phys.* **103**, 921 (1995).

19. J. D. Augspurger and C. E. Dykstra, *Chem. Phys. Lett.* **189**, 303 (1992).

20. N. Moazzen-Ahmadi, A. R. W. McKellar, and J. W. C. Johns, *Chem. Phys. Lett.* **151**, 318 (1988).

21. A. Furlan, S. Wulfelt, and S. Leutwyler, *Chem. Phys. Lett.* **153**, 291 (1988).

22. G. A. Blake, K. L. Busarow, R. C. Cohen, K. B. Laughlin, Y. T. Lee, and R. J. Saykally, *J. Chem. Phys.* **89**, 6577 (1988).

23. M. D. Schuder, C. M. Lovejoy, R. Lascola, and D. J. Nesbitt, *J. Chem. Phys.* **99**, 4346 (1993).

24. M. D. Schuder, D. S. Nelson, Jr., and D. J. Nesbitt, *J. Chem. Phys.* **99**, 5045 (1993).

25. M. J. Elrod and R. J. Saykally, *J. Chem. Phys.* **103**, 933 (1995).

26. K. Ohashi, T. Kasai, and K. Kuwata, *J. Phys. Chem.* **92**, 5954 (1988).

27. G. Scoles, "*Atomic and Molecular Beam Methods*" (Oxford University Press, London, 1988), Vol. 1.

28. Q. Zhang, L. Poth, J. V. Ford, and A. W. Castleman, Jr., *Chem. Phys. Lett.* **286**, 305 (1998).

29. M. J. Frisch, J. A. Pople, and J. E. Del Bene, *J. Phys. Chem.* **89**, 3664 (1985); J. D. Augspurger and C.E. Dykstra, private communication in relation to their work published in *Chem. Phys. Lett.* **189**, 303 (1992).

30. R. Naaman and Z. Vager, *J. Chem. Phys.* **110**, 359 (1999).

Chapter 3 is mainly based on the following articles:

K. Imura, T. Kasai, H. Ohoyama, H. Takahashi, R. Naaman, *Chem. Phys. Lett.*, **259**, 356, (1996).

K. Imura, T. Kasai, H. Ohoyama, R. Naaman, *J. Chem. Phys.*, **110,** 355 (1999).

K. Imura, H. Ohoyama, R. Naaman, D.C. Che, M. Hashinokuchi, T. Kasai, *J. Mol. Struct.*, in press.

Chapter 4 Structure and Dipole Moment of Organo-Metallic Cluster

Experimental determination of dipole moment of $Al_1(CH_3CN)_1$ and $Al_1(NH_3)_1$ clusters

4-1.1 Introduction

Over the past 20 years, much attention to the study of cluster has been paid due to the possibility of using them as an interface between gas phase and condensed phase in chemistry and physics. Various spectroscopic techniques have been developed and applied to these clusters in order to obtain specific information such as energetics, dynamics, and structures.

Alkaline metal clusters have been one of the most extensively studied clusters both experimentally and theoretically.[1,2] One reason is its relatively simple electronic configuration, which allows us to make easy comparison of experimental results with theoretical models. The second reason is its easiness of the production of those clusters. Since the development of laser evaporation method, more complicated transition metal clusters have been studied rigorously. One of the intermediates between alkaline metals and transition metals is aluminum, and it has been the subject of numerous studies since the early stages of metal cluster physics. The s^2p^1 electron configuration makes their properties rather different from those of the alkalis.[3,4,5]

Recently, there has been of considerable interest in the study of metal atom complexes with simple molecules. These clusters have exciting potential applications as models for both the fundamental interactions between metal surfaces and metal-ligand bonding. Metal-(molecule) clusters also provide gas-phase analogues of complexes studied in condensed phase organo-metallic chemistry. There have been many studies of alkaline metal atoms with small organic molecules[6,7,8,9] while very little has been done

on the clusters of Al with simple molecules in the gas phase.[10] Mille and co-workers applied electron magnetic resonance spectroscopic technique to the reaction of Al atom with several simple molecules, and they determined the structures of the reaction products.[11] However, there is still ambiguity remains to be discussed between experimentally and theoretically suggested structures and ones based on theoretical calculations. In this section, we demonstrate that the hexapole deflection technique was successfully applied to $Al_1(CH_3CN)_1$ and $Al_1(NH_3)_1$ clusters in order to reveal basic nature of clusters of Al with simple molecules.

The hexapole field state selector has been proven to be another powerful tool for obtaining important structural parameters of newly synthesized compounds, which are namely dipole moment and structural symmetry. Permanent electric dipole moment is regarded as principal electrostatic entity governing the molecular interaction with electromagnetic radiation. It is also important in the microscopic understanding of reaction dynamics since long range intramolecular interactions are dominated by dipole forces. In this sense, the determination of the dipole moment of clusters is very important for microscopic understanding of solvent effect and solvated geometry.

So far, it is known that only a few techniques can be used to determine electric dipole moment experimentally in the gas phase. Electric beam resonance method is one of the most useful techniques. Klempeler and co-workers reported dipole moment of HF-Benzene cluster by this technique.[12] Gandhi and Bernstein also suggested that the hexapole technique would serve as to determine the electric dipole moment of the clusters, and in fact, they determined dipole moment of HCl-C_6H_6 and HBr- C_6H_6 clusters, which turned out to be 1.5 D and 1.2 D, respectively.[13] These results suggest that whenever cluster formation is involved, dipole moment of cluster becomes larger

than one of monomer or simple vector summation of monomers, which is probably due to polarization effect from one of the cluster moiety. In the present section, we report the dipole moments and structures of $Al_1(CH_3CN)_1$ and $Al_1(NH_3)_1$ clusters. These results indicate that the ammonia cluster induces a larger dipole moment while its acetonitrile cluster does not. These results can be rationalized to its well-known bipolar character of Al.

4-1.2 Experimental

Our hexapole state selector apparatus has been already described in Chapter 2.[14] Therefore, only brief description and an experimental scheme will be given below. The apparatus consists of four differentially pumped chambers, that is, a nozzle, a buffer, a hexapole, and a detection chamber. At the nozzle chamber, either $Al_n(CH_3CN)_m$ or $Al_n(NH_3)_n$ clusters was synthesized by the laser evaporation-flow-tube-reactor method. Al rod purchased from Nilaco was used after cleaning of the metal surface in vacuum chamber in order to get rid of the oxide surface. Second harmonic of a pulsed Nd^{3+}:YAG laser (532 nm) was used to produce Al atoms. The laser power for the vaporization was 5-10 mJ/pulse. This laser beam was tightly focused on the Al rod, which was translated by a screw mechanism. The Al atoms were cooled by either Ne or He carrier gas and sent to the flow-tube, where sample (CH_3CN or NH_3) vapor was injected. Typical stagnation pressures for the rare gas and the sample were 600 Torr and 70 Torr, respectively. We have assumed that clusters in these conditions are produced in their electronic ground state and that the internal energy of these clusters are well described by a Maxwell-Boltzmann distribution of rotational states. This is because

clusters would have experienced multiple collisions with the carrier gas in the nozzle source. A cluster beam was skimmed, passed through the buffer chamber, and then introduced to the 2.10-m-long hexapole state-selector. This selector can focus a cluster which has permanent dipole moment and symmetric-top configuration onto the beam axis. The cluster beam transmitted through the hexapole field was ionized by a mildly focused ArF excimer laser at the detection chamber. ArF laser fluence was kept sufficiently low to avoid multiphoton processes. The cluster ions formed by photoionization were accelerated to about 800 eV at right angles to both directions of the cluster beam and the ionization laser. The ions were mass-analyzed by their time-of-flight and detected by a dual micro channel plates (MCP). Mass resolution of our TOF mass spectrometer was better than $\Delta m = 1$ in the present mass range. Mass spectra were stored and averaged by a digital oscilloscope and, if necessary, transferred to a personal computer for further analysis. Typically, 6000 mass spectra were averaged for improving signal-to-noise ratio at each hexapole-applied voltage. Focusing curves were measured by scanning the hexapole voltage from 0 to 12 kV. Electric dipole moments of the titled clusters were derived by trajectory simulations. For an exact simulation, it is necessary to obtain several other molecular constants. However, most of them are not available, because both clusters have not been studied well so far.

In order to estimate structural parameters of the clusters, and also to compare them with experimental results, *ab initio* calculation at the level of MP2 was performed as implemented in the Gaussian 94 program.[15] Cluster structures were optimized with 6-311++G** basis set by imposing the C_{3v} symmetry constrain. Furthermore, we did a natural population analysis of the optimized structure in order to get further insight to the role of the charge transfer within clusters, namely between Al and molecules.

4-1.3 Results and discussion

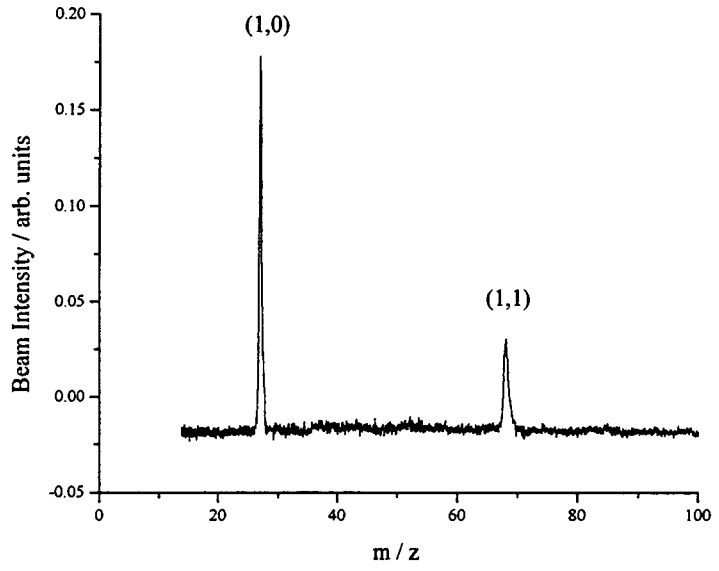

Figure 4-1-1. Time-of-flight mass spectrum of $Al_n(CH_3CN)_m$ clusters.

Figure 4-1-1 shows a time-of-flight mass spectrum of $Al_n(CH_3CN)_m$ clusters produced at a typical experimental condition. Peaks of the clusters are labeled based on

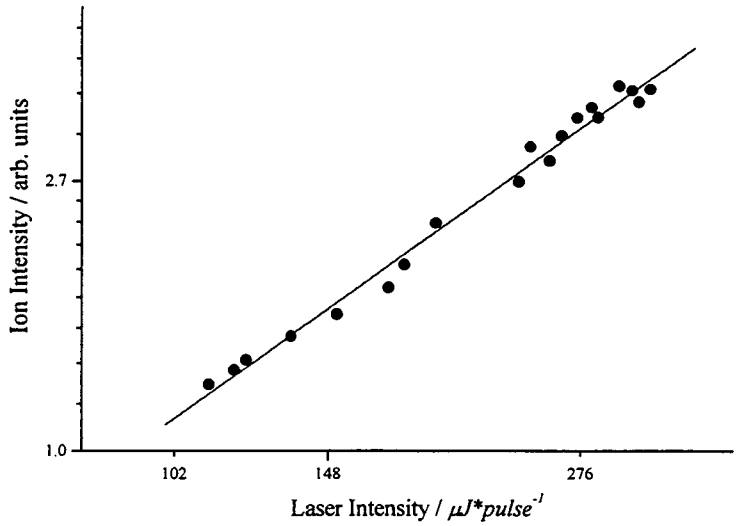

Figure 4-1-2. Logarithmic plots of the $Al_1(CH_3CN)_1^+$ beam intensity versus the ArF laser intensity.

the notation n and m, where n and m are denoted to the number of metal atoms and CH_3CN molecule, respectively. Under the present experimental conditions, clusters larger than (1-1) complex could not be detected. This can be attributed to relatively low stagnation pressure and/or short flow-reactor length. For the focusing curve measurement, experimental conditions were optimized for the (1,1) cluster formation.

Figure 4-1-2 shows the variation of $Al_1(CH_3CN)_1^+$ ion signal intensity as a function of ionization laser intensity. The ion signal increases linearly with the ionization laser intensity. This indicates that (1,1) cluster is ionized by single-photon process and its ionization potential is less than 6.4 eV.

Figure 4-1-3 shows the TOF spectrum of $Al_1(CH_3CN)_1$ cluster, obtained by scanning the ionization laser firing time. Time trigger was set to the Q-switch feed pulse of YAG laser. The velocity distribution was simulated, assuming the Maxwellian

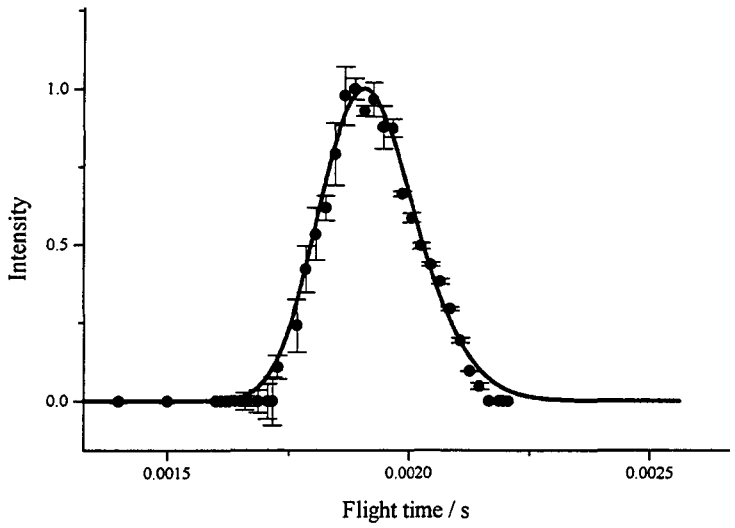

Figure 4-1-3. Time-of-flight spectra of $Al_1(CH_3CN)_1$ cluster

velocity distribution. The stream velocity and the spread of the velocity distribution were determined to be V_s = 1540 ms^{-1} and α_s = 110 ms^{-1}, respectively. This corresponds to the translational temperature of 50 K. Even after the plasma condition, it was found

that a molecular beam was sufficiently cooled down. This is ascribed to the effective cooling of the laser evaporated atoms with collisions with carrier gas and also the fact that supersonic expansion has occurred following the cluster formation. As we measured the focusing curves, the delay time of the ionizing laser was adjusted to the center of this beam pulse.

Figure 4-1-4(A) shows the experimental focusing curve of $Al_1(CH_3CN)_1$ with He carrier gas. In other words, $Al_1(CH_3CN)_1$ cluster beam intensity is shown as a function of hexapole rod voltage, V_0. Due to the resolution of the present hexapole assembly, not only one single $|JKM\rangle$ state but limited states are selected. Starting at V_0 = 5 kV, there is apparent increase in the beam intensity upon the increase of hexapole voltage. This beam enhancement indicates that this cluster has a symmetric top structure with a permanent dipole moment. This observation suggests that Al atom would be bound to either end of CH_3CN molecule.

Furthermore, the cluster is expected to have a prolate top type symmetry as suggested by *ab initio* calculation. In general, a prolate top molecule has relatively small rotational constant B compared with an oblate top. Ohoyama *et al.* suggested that a prolate top with small value of B, which is a rotational constant perpendicular to the highest symmetry axis of the molecule, could experience a finite second order Stark effect in the electrostatic field.[16] In the trajectory simulation, we took into account up to the second order Stark effect. The experimental conditions such as the velocity distribution and angular divergence of the cluster beam, and the experimental geometry of the hexapole assembly were also taken into account. We only varied the magnitude of dipole moment to optimize the fit between experimental data and simulated one. The best fit of the simulation, presented as a solid line in Fig. 4-1-4(A), suggests that the

permanent dipole moment of this cluster is 1.2 ± 0.1 D. To calculate rotational distribution, we assumed that the rotational temperature is equal to the measured translational temperature, which is a fairly typical observation for supersonic beam condition. It is found to be rather insensitive in reproducing a focusing curve. We conservatively ascribe the uncertainly of 0.1 D to our estimate for the dipole moment. Figure 4-1-4(B) shows the results of a similar measurement with Ne carrier gas was used. This measurement serves as to examine the electronically excited or other metastable states of the cluster. The data could be simulated with the same parameters as before except its own velocity distribution and rotational temperature. Since Ne carrier gas has smaller rotational cooling effect than He, translational and rotational temperatures are expected to be higher. Indeed, rotational temperature was 60 K and as a result, less cluster formation was observed.

It should be noted that we observed the same magnitude of dipole moments in

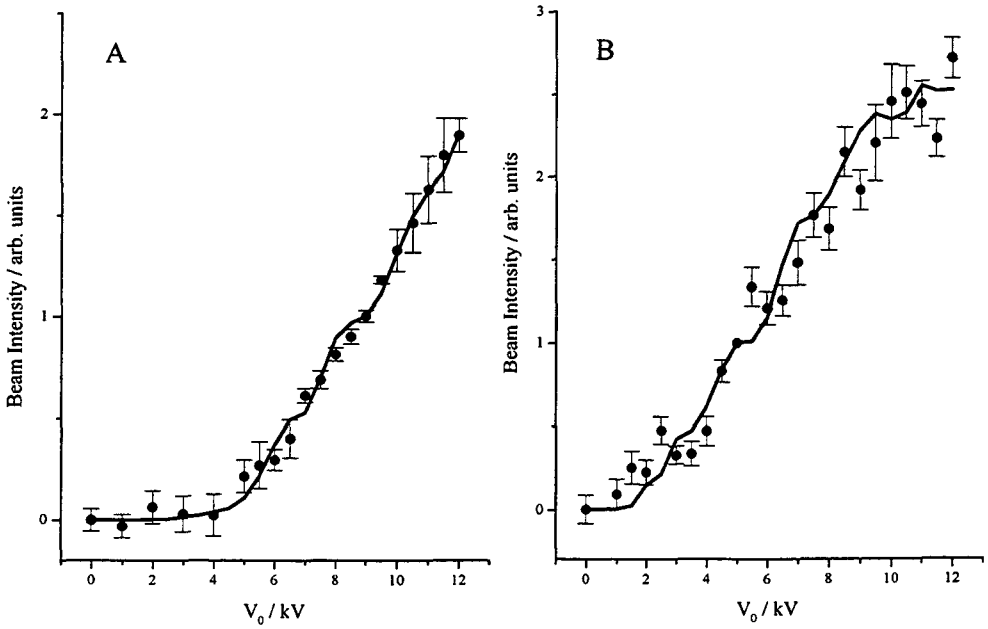

Figure 4-1-4. Focusing curve of the $Al_1(CH_3CN)_1$ cluster with (A) He carrier gas and (B) Ne carrier gas. The simulated curve is shown as a solid line.

both carrier gases. This observation suggests that in both cases, $Al_1(CH_3CN)_1$ clusters are mainly produced in the same electronic state, namely the ground state.

The same experimental setup was used to examine dipole moment of $Al_1(NH_3)_1$ cluster. For its focusing curve measurement, m/e = 44 ion was monitored and the results are shown in Fig. 4-1-5. The data were simulated by assuming rotational temperature of 30 K which is equal to translational temperature obseved, dipole moment of 2.7 D, and *JKM* states up to J = 19, K = 19 were taken into account as before. For both $Al_1(CH_3CN)_1$ and $Al_1(NH_3)_1$ focusing simulations, the rotational constant B and its temperature do not significantly affect the reproductivity of the experimental data.

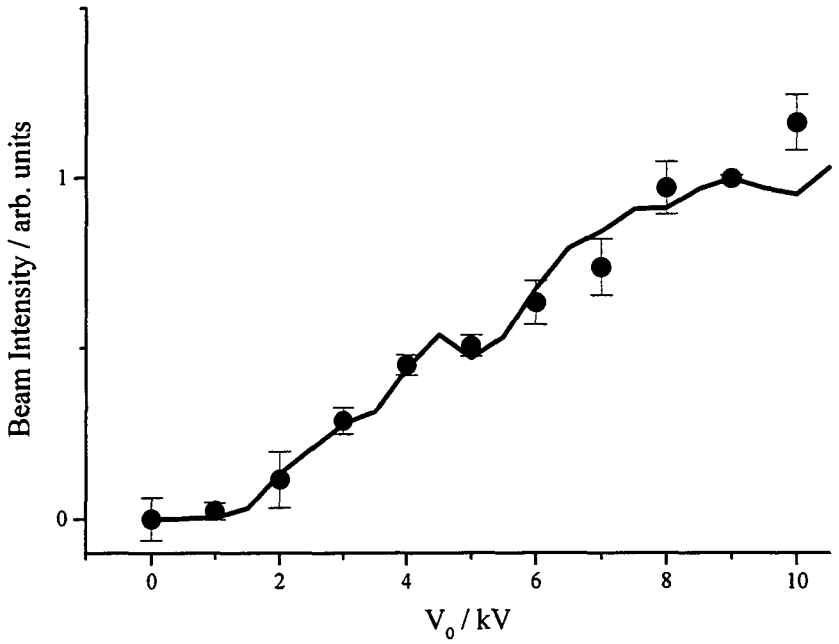

Figure 4-1-5. Focusing curve of the $Al_1(NH_3)_1$ cluster. The simulated curve is shown as a solid line.

There are several papers that have reported the reaction of Al with ammonia. Howard *et al.* suggested the formation of three mononuclear Al-NH_3 complexes, $Al(NH_3)_4$, $HAlNH_2$, and $Al(NH_3)_2$.[17] Recently, Davy and Jaffrey have performed *ab initio* calculations on three $AlNH_3$ isomers, that is, Al-NH_3, HAl-NH_2, and H_2Al-NH.[18]

The latter two isomers have been defined as insertion products. They suggested that although $HAlNH_2$ isomer showed global minima, this isomer might be unlikely to be formed though Al insertion into NH bond in NH_3 molecule because of its large barrier height, about 1.4 eV. Our observation of finite focusing of $Al_1(NH_3)_1$ results only from a symmetric or slightly asymmetric top isomer, which distorted slightly due to Jahn-

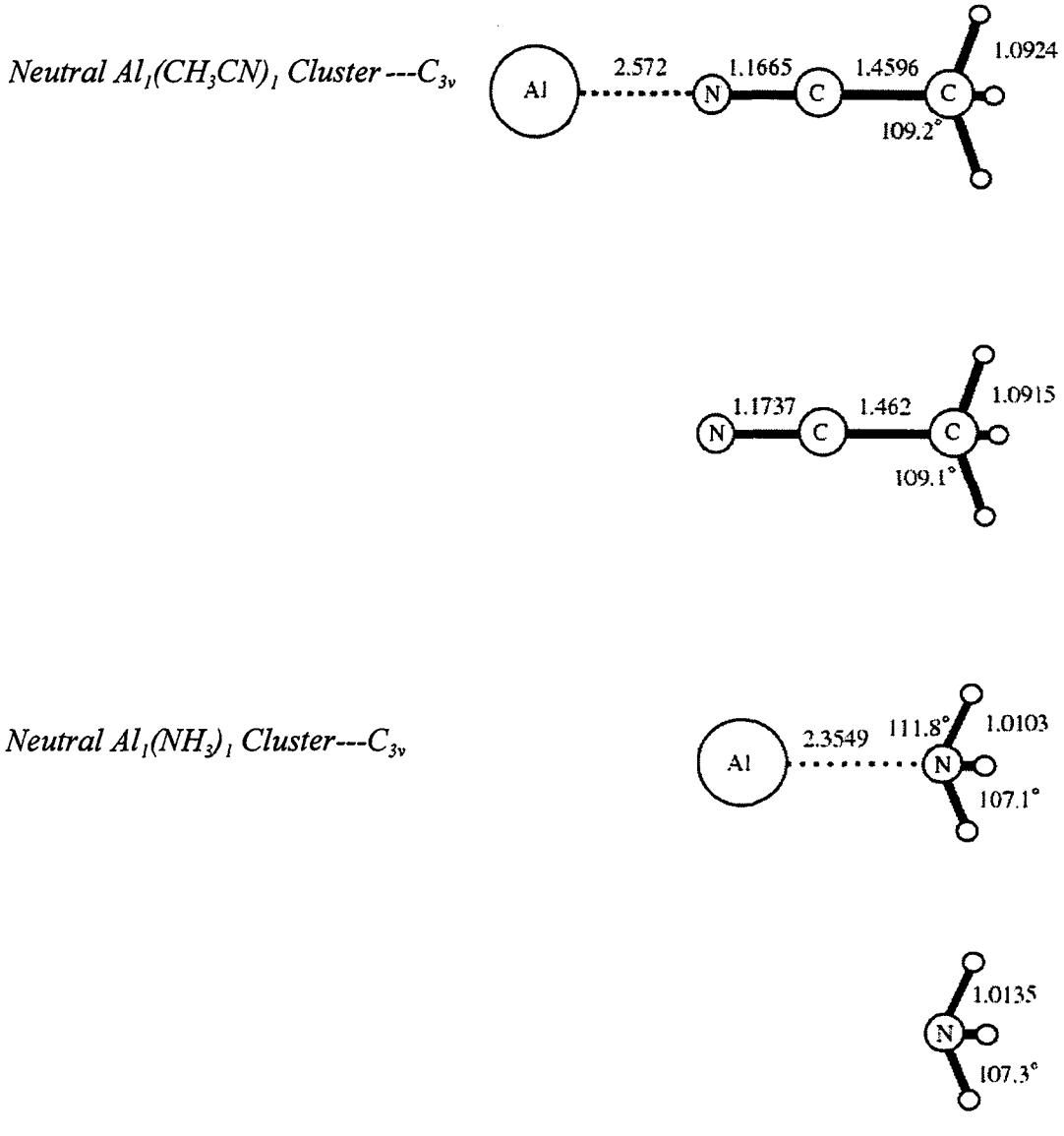

Figure 4-1-6. Optimized structure of neutral $Al_1(CH_3CN)_1$ and $Al_1(NH_3)_1$ calculated at MP2/6-311++G** level.

Teller effect. Alternatively, we measured a ratio of Al atom to $Al_1(NH_3)_1$ in molecular beam before and after the hexapole assembly. This ratio before the hexapole was in accord with that after the hexapole. It seems that these results indicate simple $Al_1(NH_3)_1$ adduct would be a major product in the present laser evaporation flow tube reactor, which means evaporated Al atoms would be effectively cooled down by collision with carrier gases. This is equivalent to recent observation of Palma *et al.*[10]

The optimized structures of $Al_1(CH_3CN)_1$ and $Al_1(NH_3)_1$ are shown in Fig. 4-1-6. There are no other optimized structures in the electronic ground state found in our calculations. Table 4-1 summarizes experimentally determined and theoretically calculated dipole moment together with the calculated binding energy.

Table 4-1. Calculated energetics and dipole moments of clusters and molecules

	D_e	$\mu_{calc.}$	$\mu_{exp.}$	$\Delta\mu_{exp.}$
NH_3	-	1.782	1.468[a]	-
$Al_1(NH_3)_1$	0.453	5.210	2.7 ± 0.2	1.2 ± 0.2
CH_3CN	-	4.301	3.92[a]	-
$Al_1(CH_3CN)_1$	0.236	7.095	1.2 ± 0.1	-2.7 ± 0.1

$\Delta\mu_{exp.} = \mu_{exp.}(Al\text{-}X) - \mu_{exp.}(X)$ (X=NH_3 or CH_3CN) [a]see Ref. 19

It is seen that this level of calculation tends to overestimate dipole moments of the molecules presented in Table 4-1, especially of clusters. It is known that theoretically calculated dipole moments show strong dependence both on basis set and methodology.[20] It should be noted that magnitude of dipole moment of $Al_1(NH_3)_1$ was enhanced both experimentally and theoretically due to the cluster formation, although experimentally determined dipole moment of $Al_1(CH_3CN)_1$ became small against the

prediction from the theoretical calculations. It is important to realize that experimental results suggest that the direction of charge transfer between metal and ligand molecule in $Al_1(NH_3)_1$ is opposite to that in CH_3CN. In addition, the results imply that aluminum in $Al_1(NH_3)_1$ should be slightly negatively charged, while it in $Al_1(CH_3CN)_1$ should be positively charged. Actually, the results of natural population analysis with UMP2/6-311++G(3df,3pd) // UMP2/6-311++G** well reproduce this bipolar nature of Al in these clusters.

Taking these results into account, we conclude that in the case that the Al atom forms a cluster with an ammonia molecule, the electron from ammonia molecule is transferred to Al. As a result, the dipole moment of cluster becomes larger than that of the original one. On the other hand, in the case of $Al_1(CH_3CN)_1$ cluster, 3p electron of Al is transferred to the CH_3CN molecule, and the dipole moment becomes small. These dipole alternations are attained by a basic nature of Al, namely its bipolar character. In addition, this aspect can be rationalized with electron affinities and proton affinities of the constituent molecules. In general, electron transfer from atom A to atom B requires energy of $(IP)_A$-$(EA)_B$, where $(IP)_A$ is the ionization potential of atom A, and $(EA)_B$ is the electron affinity of atom B. Inversely, in case an electron transfer occurs from B to A, $(IP)_B$-$(EA)_A$ is necessary. Then, the direction of electron transfer between A and B can be determined by a sign of the following equation:

$$[(IP)_A + (EA)_A] - [(IP)_B + (EA)_B] \qquad (4\text{-}1)$$

For the case of positive value of Eq. (4-1), an electron transfer occurs from A to B and for that of the negative, transfer from B to A is likely. We apply this relationship to

$Al_1(CH_3CN)_1$ and $Al_1(NH_3)_1$ clusters. As we regarded CH_3CN or NH_3 molecule as atom B, the sign of *Eq.* (4-1) was opposite for each molecule. This direction was consistent with the discussion from the dipole moments. It means that this simple relation expressed by *Eq.* (4-1) could predict the direction of charge transfer in these clusters. Physical aspects of the discussion above indicate that interaction between either occupied or unoccupied 3p orbital of Al and either LUMO or HOMO of molecule plays an important role in the formation and stabilization of these cluster.

References

1. A. deHeer, *Rev. Mod. Phys.*, **65**, 611 (1993).
2. M. Brack, *Rev. Mod. Phys.* **65**, 677 (1993).
3. K.E. Schriver, J.L. Persson, E.C. Honea, R.L. Whetten, *Phys. Rev. Lett.*, **64**, 2539 (1990); T.H. Upton, *J. Chem. Phys.*, **86**, 7054 (1987); E. Cottancin, M. Pellarin, J. Lerme, B. Baguenard, B. Palpant, J.L. Vialle, M. Broyer, *J. Chem. Phys.*, **107**, 757 (1997).
4. L.G.M. Pettersson, C.W. Bauschlicher, Jr, *J. Chem. Phys.*, **87**, 2205 (1987); R.O. Jones, *J. Chem. Phys.*, **99**, 1194 (1993).
5. O. Ingolfsson, H. Takeo, and S. Nonose, *J. Chem. Phys.*, **110**, 4382 (1999).
6. C.P. Schultz, R. Haugstaetter, H.U. Tittles, I.V. Hertel, *Phys. Rev. Lett.*, **57**, 1703 (1986); C.P. Schultz, R. Haugstaetter, H.U. Tittles, I.V. Hertel, *Z. Phys. D* **10**, 279 (1998).
7. M. Trenary, H.F. Schaefer III, *J. Chem. Phys.* **68**, 4047 (1978).
8. M. Trenary, H.F. Schaefer III, *J. Am Chem. Soc.*, **99**, 5833 (1990).
9. K. Ohoshimo, H. Tsunoyama, Y. Yamakita, F. Misaizu, K. Ohno, *Chem. Phys. Lett.*, **301**, 356 (1999).
10. T.D. Palma, A. Latini, M. Satta, M. Varvesi, A. Giardini, *Chem. Phys. Lett.*, **284,** 184 (1998).
11. J.H.B. Chenier, J.A. Howard, J.S. Tse, B. Mile, *J. Am. Chem. Soc.*, **107**, 7290 (1985); J.H.B. Chenier, J.A. Howard, B. Mile, *J. Am. Chem. Soc.*, **109**, 4109 (1987); J.A. Howard, H.A. Joly, B. Mile, M. Histed, H. Morris, *J. Chem. Soc. Fraday Trans. 1.* **84**, 3307 (1988); M. Histed, J.A. Howard, H. Morris, B. Mile, *J. Am. Chem. Soc.*,

110, 5290 (1988).

12. F.A. Balocchi, J.H. Williams, and W. Klemperer, *J. Phys. Chem.*, **87**, 2079 (1983).
13. S.R. Gandhi, R.B. Bernstein, *Chem. Phys. Lett.*, **143**, 332 (1988).
14. K. Imura, H. Ohoyama, T. Kasai, R. Naaman, *J. Chem. Phys.*, **110**, 355(1999).
15. M.J. Frisch, G.W. Trucks, H.B. Schlegel, P.M. W. Gill, B.G. Johnson, M.A. Robb, J.R. Cheeseman, T. Keith, G.A. Petersson, J.A. Montgomery, K. Raghavachari, M.A. Al-Laham, V.G. Zakrzewski, J.V. Ortiz, J.B. Foresman, J. Cioslowski, B.B. Stefanov, A. Nanayakkara, M. Challacombe, C.Y. Peng, P.Y. Ayala, W. Chen, M.W. Wong, J.L. Andres, E.S. Replogle, R. Gomperts, R.L. Martin, D.J. Fox, J.S. Binkley, D.J. Defrees, J. Baker, J.P. Stewart, M. Head-Gordon, C. Gonzalez, and J.A. Pople, GAUSSIAN 94, Revision D.2, Gaussian, Inc., Pittsburgh, PA, 1995
16. H. Ohoyama, T. Ogawa, T. Kasai, *J. Phys. Chem.*, **99**, 13606 (1995).
17. J.A. Howard, H.A. Joly, P.P. Edwards, R.J. Singer, and D.E. Logan, *J. Am. Chem. Soc.*, **114**, 474 (1992).
18. R.D. Davy and K.L. Jaffrey, *J. Phys. Chem.*, **98**, 8930 (1994).
19. C.H. Townes and A.L. Schawlow, "*Microwave Spectroscopy*" (McGraw-Hill, New York, 1955).
20. M.J. Frisch, J.A. Pople, J.E. Del Bene, *J. Phys. Chem.*, **89**, 3664 (1985).

Structural Selection of $Al_1(C_6H_6)_1$ Isomers

4-2.1 Introduction

Clusters of Al atom with simple organic molecules have been growing its interest, because of its related understanding of the elemental reaction mechanisms of catalysis, surface chemistry, and so on. The reaction of the ground state Al atoms with benzene molecule in neon matrices was first reported by Kasai and McLeod.[1] Reaction products were examined by ESR spectroscopy. The spectrum revealed interaction with

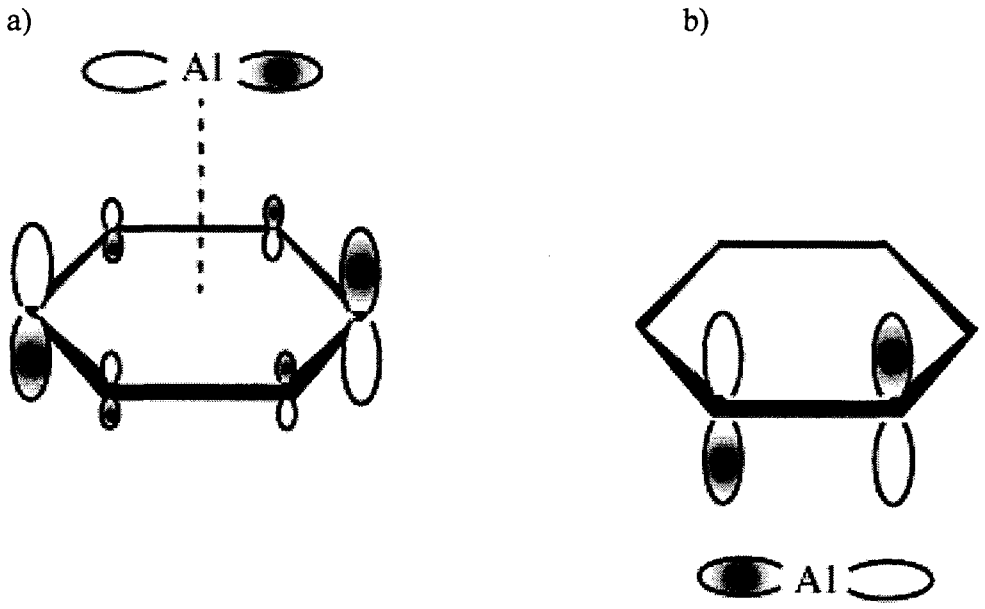

Figure 4-2-1. Schematic view of structures and frontier orbital diagrams of $Al_1(C_6H_6)_1$ isomers

only two of six protons of benzene. These authors suggested a p-coordination complex in which the $3p_x$ orbital of Al which contains the unpaired electron, interacts with one C=C units in benzene through the 2p orbital components of the LUMO of benzene as shown in Fig. 4-2-1(b). Alternatively, Howard *et al.* studied the same reaction at 77 K in benzene and inert hydrocarbon matrices on a rotating cryostat, and measured ESR

spectra at several temperatures.[2] $Al_1(C_6H_6)_1$ was the only paramagnetic product found. They proposed two bonding schemes of this product: (i) a η^2-complex with the Al positioned above one of the carbon-carbon bonds by interaction with the two para protons and (ii) a η^6-complex in which the Al lies along the C_6 axis and bridges two para carbons by interaction with two para protons. From the spectral changes with temperature, the authors suggested that structure (i) was likely at low temperature, 4 K, and the other one was more likely at higher temperature, 220 K.

In an attempt to shed more light on this complex, we have determined dipole moments of the $Al_1(C_6H_6)_1$ isomers by using an electrostatic hexapole focusing technique. In addition to this experiment, we have also performed density functional calculations in order to obtain better understanding for energetical stability of these isomers.

4-2.2 Experimental

The detailed experimental system has been already described in Chapter 2, then only brief description will be given here. Translating Al metal rod through rotation was vaporized by tightly focused 2nd harmonic YAG laser. Generated Al plasma was cooled down to near room temperature by He carrier gas. Produced Al atoms reacted with benzene vapors, which was differentially injected by a pulsed valve at about 70 Torr stagnation pressure. $Al_1(C_6H_6)_1$ cluster was produced in a cluster source, skimmed, and introduced into a hexapole field after passing through a buffer chamber. Focused cluster beam due to the Stark effect was ionized by a ArF excimer laser in a detection chamber. Typical ionization laser power employed was about 200 μJ/pulse to avoid

multiphoton processes and fragmentation. Size distribution of $Al_n(C_6H_6)_m$ cluster was measured by the time-of-flight mass spectrometer. Mass spectra were stored as a time-profile of signals in a digital oscilloscope. For the focusing curve measurement, typically 6000 time profiles were accumulated at each hexapole applied voltage, V_0. In order to average out fluctuations of probe laser power, stagnation pressure, and plasma conditions, normalization scheme was adopted, that is, every 600 sets of time profiles at each V_0 were normalized to those at 5 kV and also normalized to probe laser intensity. Trajectory simulations were carried out by using the same values of experimental parameters as in the determination of electric dipole moments of $Al_1(C_6H_6)_1$ isomers.

4-2.3 Results

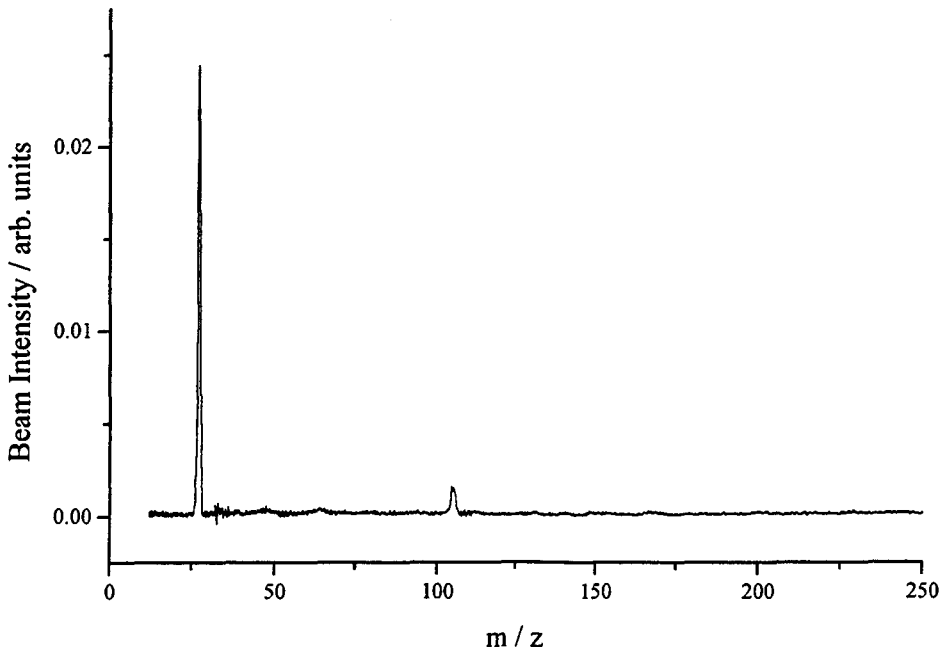

Figure 4-2-2. Time-of-flight mass spectrum of $Al_n(C_6H_6)_m$ clusters. Spectrum obtained at 700 Torr stagnation pressure of He and 70 Torr that of benzene.

Figure 4-2-2 shows a typical time-of-flight mass spectrum of $Al_1(C_6H_6)_1$ cluster. Under the present experimental conditions, stagnation pressure of carrier gas ranged from 500 to 2000 Torr and clusters larger than one to one complex were not observed. However, transition metal-C_6H_6 clusters of one to two, ferrocene type complex were formed more efficiently in this pressure range. This can be attributed to either instability or extremely weak bond for this ferrocene type structure since the ionization potential of one by two cluster would be lower than that of one by one cluster. Alternatively, we measured probe laser intensity dependence of $Al_1(C_6H_6)_1$ signal intensity. It was found

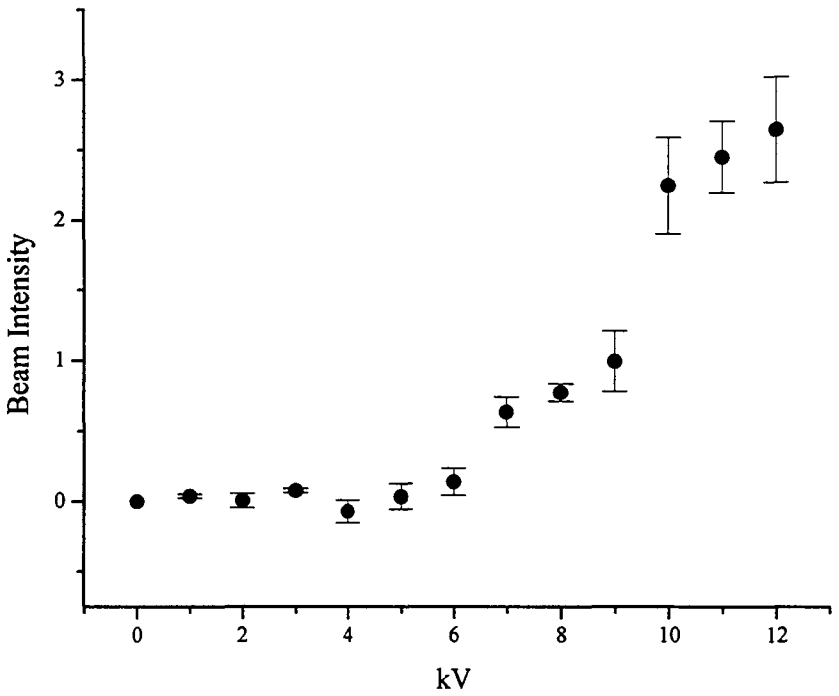

Figure 4-2-3. The measured beam intensity as a function of the potential on the hexapole (V_0) measured at m/e = 105, which corresponds to $Al_1(C_6H_6)_1$ parent ion.

that signal was linearly proportional to the probe laser intensity, this means that the mass spectra were obtained under one photon ionization regime.

Figure 4-2-3 shows the experimental focusing curve of $Al_1(C_6H_6)_1$ cluster when the $Al_1(C_6H_6)_1$ parent mass peak (m/e = 105) intensity was monitored. As can be easily

seen in the figure, there is a constant increase of signal intensity from 5 kV and especially, a steep increase around 10 kV. It seems that this focusing curve consists of two major components. Before discussing the focusing curve in detail, we demonstrate theoretical calculations for the structures of $Al_1(C_6H_6)_1$ isomers.

Structure calculations of $Al_1(C_6H_6)_1$ cluster

The structures of neutral $Al_1(C_6H_6)_1$ clusters were optimized without any symmetry restrictions by DFT program of Gaussain 94.[3] The 6-31G(d) basis set was

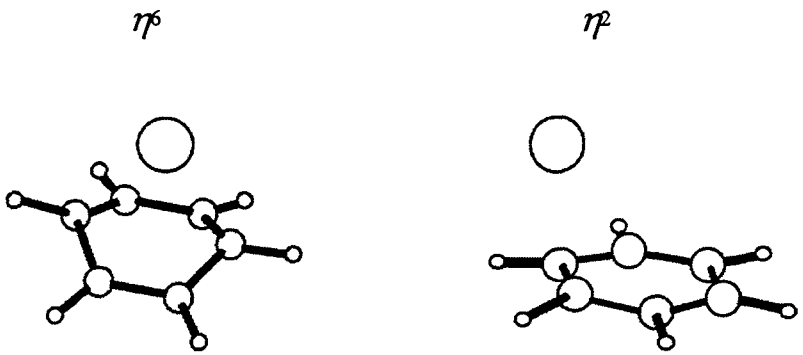

Figure 4-2-4. Optimized structures of $Al_1(C_6H_6)_1$ isomers calculated at the UB3LYP/6-31G* level. Geometrical parameters are given in angstroms and degrees.

used for these calculations. As suggested previously,[4,5] basis set requirements are much less stringent for DFT than for post-HF methods regarding the structure analysis. We found that optimized structures would not be so different from those from higher level of calculations. The B3LYP functional was utilized in the present calculations. The geometries of two isomers optimized with B3LYP/6-31G(d) are shown in Fig. 4-2-4. It was found that η^2 isomer gives the global minima, which is 0.138 eV more stable than η^6 isomer, and that there were no other optimized structures. The calculated binding

energy of η^2 isomer was 0.08 eV.

4-2.4 Discussion

In trajectory simulation, we took into account the contributions from two isomers, one is η^6-type nearly symmetric top and the other one is η^2-type asymmetric top. We regard a nearly symmetric top cluster as a symmetric top because the energy barrier to rotation of the bonding across the para positions around the ring should be small due to the weak nature of the C-Al bonds. This is a quite reasonable assumption since Howard *et al.* has succeeded in simulating ESR spectra at 220 K by assuming C_{6v} structure and suggested that η^2-η^2 rotation conversion barrier height was about 4-8 kJ/mol. In practice, the frontier orbital description of the Al atom and benzene molecule given in Fig. 4-2-1 shows it to be symmetry allowed with LUMO and HOMO orbitals of both able to correlate. For the η^6 symmetric top isomer, a trajectory simulation was performed in usual manner; namely first Stark effect was considered, where rotational temperature was assumed to be 76 K, *JKM* states up to $J = 15$, $K = 15$ were taken into account, and electric dipole moment was only one fitting parameter. Beam enhancement at lower V_0 was fit by this isomer with dipole moment of 1.5 D as shown in Fig. 4-2-5. For the asymmetric top cluster, we divide its Stark effect into two cases, (1) non-degenerate levels and (2) nearly degenerate levels.

(1) For the usual case of Stark effect in asymmetric top molecule,[6,7,8,9] near degeneracy does not occur and the Stark energy can be expressed by *Eq.* (4-2). This equation consists the sum number of terms containing matrix elements between rotational states.

$$\Delta W_2 = \sum_{n'} \frac{|\mu_{nn'}|^2 E^2}{W_n - W_{n'}} \tag{4-2}$$

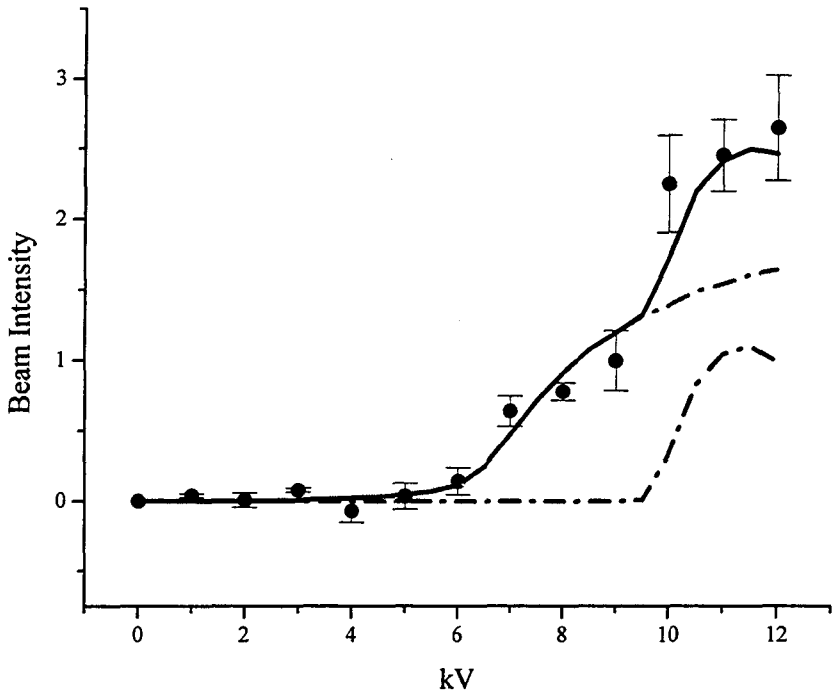

Figure 4-2-5. The results from simulation assuming the C_{6v} structure and a dipole moment of 1.5 D are shown as a dotted line. The results from a simulation based on a slight symmetric top structure, η^2, and assuming a dipole moment of 1.5 D is shown as a dashed line. The solid line is the sum obtained by adding the contribution from the two isomers.

where W_n is the energy of undistributed state and $W_{n'}$ is the energy of any other state unperturbed by the electric field. The direction matrix elements take simple form only when the rotor is approximately symmetric, which is shown in Table 4-2-1. The direction matrix element for an asymmetric top can be broken down into several factors as the following.

Table 4-2-1. Values of factors of the direction-cosine matrix elements

Matrix element factor	Value of J'		
	J+1	J	J-1
$\phi_{JJ'}$	$[4(J+1)\{(2J+1)(2J+3)\}^{1/2}]^{-1}$	$[4J(J+1)]^{-1}$	$[4J(4J^2-1)^{1/2}]^{-1}$
$(\phi_a)_{JKJ'K}$	$2[(J+1)^2-K^2]^{1/2}$	$2K$	$+2[J^2-K^2]^{1/2}$
$(\phi_b \text{ or } \pm i\phi_c)_{J,K,J',K\pm1}$	$\mp[(J\pm K+1)(J\pm K+2)]^{1/2}$	$[(J\mp K)(J\pm K+1)]^{1/2}$	$\pm[(J\mp K)(J\mp K-1)]^{1/2}$
$(\phi_z)_{JMJ'M}$	$2[(J+1)^2-M^2]^{1/2}$	$2M$	$+2[J^2-M^2]^{1/2}$
$(\phi_x \text{ or } \mp i\phi_y)_{J,M,J',M\pm1}$	$\mp[(J\pm M+1)(J\pm M+2)]^{1/2}$	$[(J\mp M)(J\pm M+1)]^{1/2}$	$\pm[(J\mp M)(J\mp M-1)]^{1/2}$

The dipole moment matrix element is $\mu\phi_{JJ'}\phi_{JKJ'K'}\phi_{JMJ'M'}$. Subscript a applies to cases where μ is along the molecular axis, b or c to cases where μ is perpendicular to this axis. Subscript x, y, or z apply for μ_x, μ_y, or μ_z, which are the appropriate elements for polarization along the x, y, or z directions, respectively. The phases chosen are consistent with reference. Matrix elements listed are appropriate for a prolate symmetric top (with a the symmetric axis). For an oblate symmetric top, ϕ_a should be replaced by ϕ_c, ϕ_c by ϕ_b, and ϕ_b by ϕ_a.

$$< J\tau M|J'\tau' M'>= < J|\Phi|J'> < JM|\Phi|J'M'>\sum_{\tau'} < J\tau|\Phi|J'\tau'> \qquad (6\text{-}2)$$

where $\tau(= K_{-1} - K_1)$ is the pseudo-quantum number. (K_{-1} is the quantum number in the prolate top limit and K_1 is in the oblate limit.) These terms are listed in Table 4-2-1; an electric field can mix only $\Delta J = 0, \pm 1$, $\Delta K = 0$, and $\Delta M = 0$, so that the entire Stark energy in the case of no degeneracy can be written as:

$$\Delta W_2 = \sum_{x=a,b,c} \frac{\mu_x^2 E^2}{2J+1} \sum_{\tau'} \left[\frac{J^2 - M^2}{J(2J-1)} \frac{{}^x S_{J\tau,J-1\tau'}}{W_{J\tau} - W_{J-1\tau'}} + \frac{M^2}{J(J+1)} \frac{{}^x S_{J\tau,J\tau'}}{W_{J\tau} - W_{J\tau'}} + \frac{(J+1)^2 - M^2}{(J+1)(2J+3)} \frac{{}^x S_{J\tau,J+1\tau'}}{W_{J\tau} - W_{J+1\tau'}} \right]$$

where a, b, and c indicate the direction of the three principal axes of moment of inertia and E is the electric field. Although ${}^x S_{J\tau,J'\tau'}$ matrix elements in the equation above have to be computed in connection with an evaluation of the transition intensities, these elements have been already tabulated.[6,8] The asymmetric rotor contains up to three nonzero permanent electric dipole moment component μ_x coincident with three principal axes (a, b, c).

Table 4-2-2. Selection rules for asymmetric tops: In all cases $\Delta J = 0, \pm 1$

Axes parallel to dipole moment	Allowed transitions
a (least)	$ee \leftrightarrow eo$ $oo \leftrightarrow oe$
b (intermediate)	$ee \leftrightarrow oo$ $eo \leftrightarrow oe$
c (greatest)	$ee \leftrightarrow oe$ $oo \leftrightarrow eo$

Symmetry properties have been discussed in terms of the evenness or oddness of K_{-1} and K_1, which are indicated by e or o.

In this thesis, an *a*-type, *b*-type, or *c*-type rotor is classified as an asymmetric rotor containing a single dipole moment component which is directed along the *a*, *b*, or *c* principal axis, respectively.[10] According to our *ab initio* calculations, η^2 cluster was defined as a *b*-type rotor. In addition, Table 4-2-2 summarizes the selection rules in terms of parity changes in the *K*'s makes above equation relatively simpler. Actually, this is not the present case, but the above notation is very useful for nearly degenerate case as in the following.

(2) Some energy levels are sometimes nearly coincident and linked by non-zero transition moments. As a consequence, the second order expression in case (1) breaks down and we have to diagonalize Stark interaction matrix for the two interacting levels exactly in the same fashion in the case of NH_3. Physically what happen is that the Stark interaction energy increases and becomes large compared to the unperturbed level

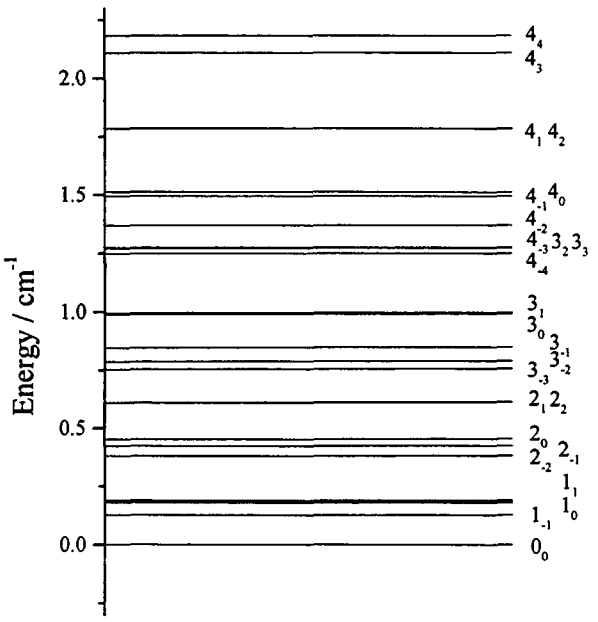

Figure 4-2-6. Rotational energy levels of $Al_1(C_6H_6)_1$ cluster

separation. These levels are essentially degenerate and the Stark effect becomes first order as in the symmetric rotor.

It is easily recognized that such a situation occurs at several rotational levels in η^2-$Al_1(C_6H_6)_1$ isomer as can be seen in Fig. 4-2-6. In fact, many levels are almost degenerate and linked to non-zero transition moment. It should be noted that although energy levels of different J quantum numbers lie relatively far apart from one another, those between identical J numbers do closer, especially regarding with low J quantum numbers. Stark energy for these rotational levels can be written as:[7]

$$\Delta W = \frac{(W_{J\tau} - W_{J\tau'})}{2} \pm [\frac{(W_{J\tau} - W_{J\tau'})^2}{2} + \mu^2 E^2 \frac{{}^b S_{J\tau,J\tau'} M^2}{J(J+1)(2J+1)}]^{\frac{1}{2}}$$

This Stark energy would become larger as energy difference of $W_{J\tau}$-$W_{J\tau'}$ decreases. If these two energy levels are supposed to degenerate, as a general trend, Stark energy would decrease with increasing J value. Then, for this simulation, rotational states only up to J = 4 were taken into account, since practically higher levels than these states would not be focused within our experimental conditions any way.

As seen in Fig. 4-2-5, an asymmetric cluster with almost the same magnitude of dipole moment, 1.5 D is only focused at $V_0 > 10$ kV and the steep enhancement of the beam was well reproduced. The measured focusing curve could be reproduced nicely by assuming contributions from two isomers. These findings suggest that η^2 and η^6 isomers may not be converted to each other due to either in our observation time that it is about 2 ms, or to temperature of cluster itself. Hence, the existence ratios of these isomers can be determined immediately just after the adiabatic expansion from the cluster source, it indicates that inter-conversion reaction would not occur within our beam temperature.

4-2.5 Conclusion

We have demonstrated structure selection of $Al_1(C_6H_6)_1$ cluster by using the electrostatic hexapole field. From the focusing curve measurement of this cluster, we simultaneously observed two isomers, one has a symmetric top structure, η^6, and the other one is a slightly symmetric top structure, η^2. The existence ratio was about 6-10, which might reflect the temperature in the cluster formation. *Ab initio* calculations have been also performed to investigate these structures. It was found that the energy difference between η^2 and η^6 isomers was 0.138 eV. Hence, a barrier height of internal conversion between them is larger than 0.138 eV, which indicates that internal conversion would not occur in the range of our beam temperature. On the other hand, as an energy barrier for η^2-η^2 is rather small, rotational conversion can occur even in our beam temperature. This is the first demonstration of structure selection of neutral cluster. We proposed the new application of the hexapole field technique. This method even allows us to obtain some dynamical information of these systems.

References

1. P.H. Kasai and D. McLeod, Jr., *J. Am. Chem. Soc.*, **101**, 5860 (1979).
2. J.A. Howard, H.A. Joly, and B. Mille, *J. Am. Chem. Soc.*, **111**, 8094 (1989).
3. M.J. Frisch, G.W. Trucks, H.B. Schlegel, P.M.W. Gill, B.G. Johnson, M.A. Robb, J.R. Cheeseman, T. Keith, G.A. Petersson, J.A. Montgomery, K. Raghavachari, M.A. Al-Laham, V.G. Zakrzewski, J.V. Ortiz, J.B. Foresman, J. Cioslowski, B.B. Stefanov, A. Nanayakkara, M. Challacombe, C.Y. Peng, P.Y. Ayala, W. Chen, M.W. Wong, J.L. Andres, E.S. Replogle, R. Gomperts, R.L. Martin, D.J. Fox, J.S. Binkley, D.J. Defrees, J. Baker, J.P. Stewart, M. Head-Gordon, C. Gonzalez, and J.A. Pople, GAUSSIAN 94, Revision D.2, Gaussian, Inc., Pittsburgh, PA, 1995
4. V. Baron, *Chem. Phys. Lett.*, **226**, 392 (1994).
5. G.L. Laming, V. Termath and N.C. Handy, *J. Chem. Phys.*, **99**, 5612 (1993).
6. C.H. Townes and A.L. Schawlow, *"Microwave Spectroscopy"* (Dover publications, New York, 1975.)
7. H.W. Kroto, *"Molecular Rotation Spectra"* (Dover publications, New York, 1992).
8. P.C. Cross, R.M. Hainer, G.W. King, *J. Chem. Phys.*, **12**, 210 (1944).
9. S.Golden, E.B. Wilson, Jr, *J. Chem. Phys.*, **16**, 669 (1948).; S.A. Mitchell, B. Simard, D.M. Raynor, and P.A. Hackett, *J. Phys. Chem.*, **92**, 1655 (1988).
10. T.D. Hain, R.M. Moision, T.J. Curtiss, *J. Chem. Phys.*, **111**, 6797 (1999).

Structures and Dipole Moments of Metal-Benzene Half-Sandwich Clusters

4-3.1 Introduction

In the last two decades, the development of laser evaporation method has enabled us to synthesize organometallic compounds in the gas phase.[1-7] It should be noted that some of these compounds can not be synthesized by a crucible method due to the difficulty in producing well-cooled metal atoms. One of the most important features of this method is that the interaction of metal atoms with ligand molecules can be investigated without any perturbation from solvent. Most of studies related to organometallic clusters have focused on the generation and investigation of larger clusters in order to compensate the gap between gas phase and solid phase chemistry and physics.[7-9]

Kaya and co-workers have reported the preparation of several transition metals and benzene clusters.[7-9] Structures of these clusters are a basically sandwich type in analogy to ferrocene in the range of small sizes. Due to the fact that the mass spectra exhibiting magic number behavior, their reactivity toward CO and NH_3, and their ionization energies, it was concluded that the $V_n(C_6H_6)_m$ clusters take multiple-decker sandwich structures of alternating vanadium and benzene molecules while substitution of V atoms by another transition metals is unlikely to lead to multi-decker structure formation. Yasuike *et al.* examined this metal specificity and their growth mechanism by quantum chemical calculations.[10,11] The calculation results suggest that total spin conservation in growth process plays an important role and the production in the sandwich clusters particularly favors a process through lower spin states.

In the present study, we generated several M(Ti, V, Co, Ni)$_1$-$(C_6H_6)_1$ cluster

and examined their structures and electric dipole moments by using a hexapole beam focusing technique in order to obtain the physical trend and new aspects of the transition metal and benzene cluster. The results showed that the early transition metal atoms such as Ti and V with benzene binary complex have a nearly C_{6v} structure and relatively large electric dipole moment. On the other hand, the late transition metals such as Co and Ni with benzene cluster have small dipole moment.

4-3.2 Experimental

Details of the experimental setup have been already provided in Chapter 2. Briefly, transition metal (Ti, V, Co, Ni)-C_6H_6 clusters were generated by a laser evaporation-flow-reactor method. Vaporization of the metal rod was effected with a pulsed second harmonic of YAG laser tightly focused onto the target rod and typically run at 10 Hz with power of 5-10 mJ. The desorption plasma was cooled in a pulsed carrier He gas jet. The metal atoms were sent to the flow tube reactor, where benzene vapor is injected. Passing through a buffer chamber, produced metal- C_6H_6 clusters were introduced to a hexapole electrostatic field, where some of clusters were exerted torque due to the Stark effect. Clusters transmitted through a hexapole exit collimator were ionized by an ArF excimer laser. Signal dependence upon the laser intensity revealed that ionization occurred under single photon process. The ions were mass-analyzed by a time-of-flight mass spectrometer and detected by a multi-channel plate. Mass spectra were accumulated and stored in a digital oscilloscope for further analysis. Focusing curves were measured at signal of $M_1(C_6H_6)_1$ parent ions in a mass spectrum by scanning the hexapole-biased voltage.

4-3.3 Results and discussion

Figure 4-3-1 shows time dependent TOF-MS spectrum of the $Ti_n(C_6H_6)_m$

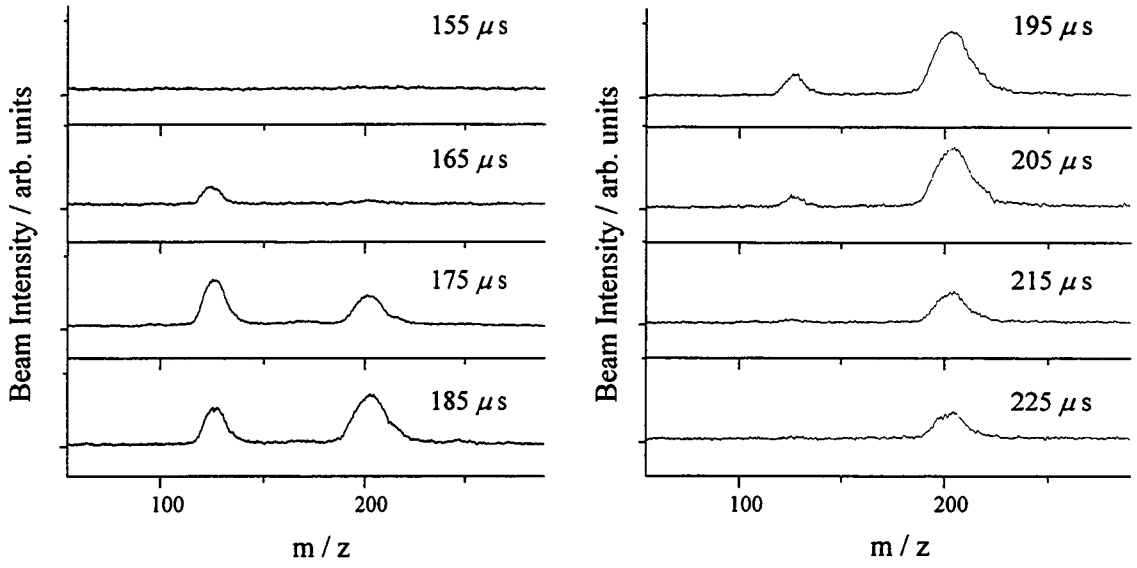

Figure 4-3-1. Time variation of time-of-flight mass spectra of $Ti_n(C_6H_6)_m$ clusters

clusters measured at a buffer chamber. Short time-of-flight length caused a rather poor mass resolution. Time in Fig. 4-3-1 was defined by the difference between pump and probe laser firing time. a trigger was set to firing time of pump laser and then spectra were measured by scanning the probe laser delay against the time-fixed pump laser. As can be seen in the figure, when scanning the time delay of probe laser, relative intensities of (1,1) and (1,2) clusters varied drastically. This feature could be also seen in the other metal-C_6H_6 clusters. This observation indicates that (1,2) cluster is not produced by the reaction of a Ti atom with a benzene dimer, but by a sequential process,

namely $Ti_1(C_6H_6)_1$ combining with another benzene molecule. It is easily realized that

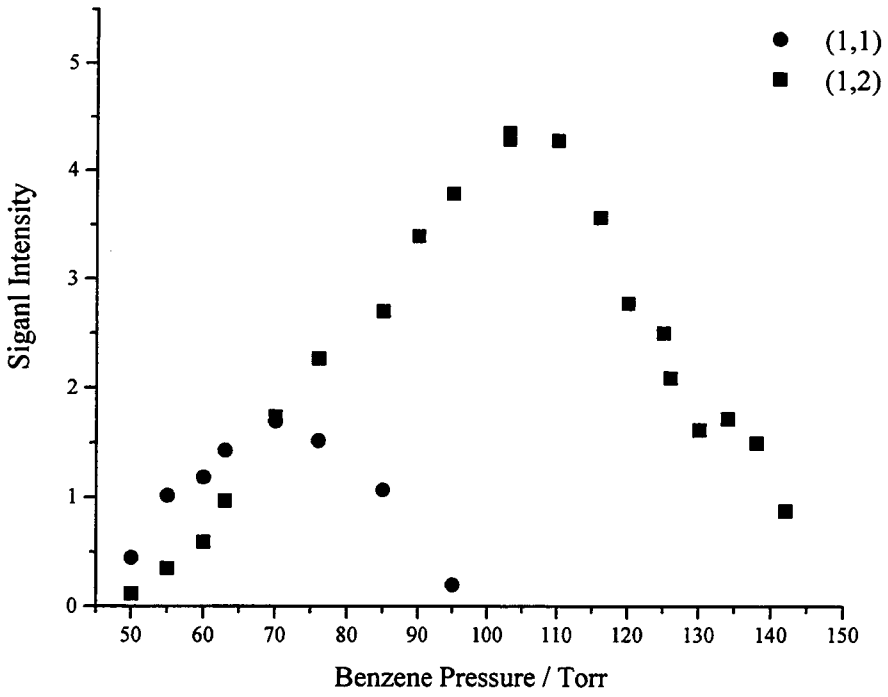

Figure 4-3-2. The pressure dependence of the signal of (1,1) and (1,2) clusters obtained at a fixed vaporization-probe laser time delay.

the longer reaction channel, the larger clusters to be produced. In fact, Kaya and co-workers was succeeded in producing $V_n(C_6H_6)_{n+1}$ clusters up to $n = 7$ by using a longer reaction cell than ours.[7]

Figure 4-3-2 shows the benzene pressure dependence of production of (1,1) and (1,2) clusters for $Ti_n(C_6H_6)_m$. As can be seen in the figure, (1,1) cluster formation is dominant at lower stagnation pressure of benzene and (1,2) cluster formation turns out to be exclusively dominant at higher pressure of benzene. This observation again suggested that (1,2) clusters were formed through a sequential process because at higher benzene pressure, (1,1) cluster could react with an another benzene molecule. It should be realized that under present experimental conditions for benzene, less benzene cluster

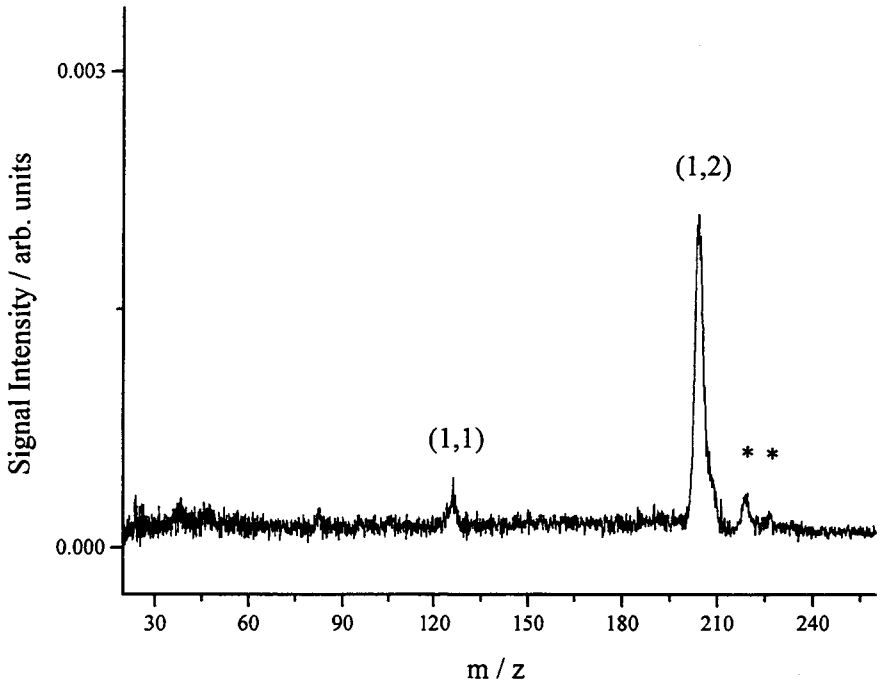

Figure 4-3-3. Time-of-flight mass spectrum of $Ti_n(C_6H_6)_m$ clusters measured at detection chamber. * are back-ground signal which may originate from diffusion oil.

formation is expected. The same pressure dependence of the cluster formations was examined for all the other metals. The above tendency was the same for the other metals. It was found that for the early transition metals such as V and Ti, production ratios of (1,1) to (1,2) clusters were very sensitive to the benzene pressure. On the other hand, for the late transition metals such as, Ni and Co, this production ratio was less affected by the benzene pressure. These observations can be rationalized with the well-known 18-electrons rule. Although $Ti_1(C_6H_6)_2$ and $V_1(C_6H_6)_2$ lack 1 or 2 electrons of 18 electrons, respectively, they are well stabilized through de_2 to Le_2 back donation (valence electrons of metal occupy the bonding orbitals.) In fact, these clusters have been synthesized in bulk.[13] On the other hand, the complex of the late transition metal with two benzene molecules has more than 18 electrons. As a result, the total stabilization energy is expected to become smaller because additional electrons from 18-electron

have to occupy the anti-bonding orbital. As this is the case, the stability of (1,2) cluster is no more different from that of (1,1) cluster. Indeed, the production of (1,2) cluster of the late transition metals were about 20 – 50% less than that of the early transition metals. Although we also tried to generate either Fe or Cu atom with benzene clusters, it was not succeeded besides repeated efforts. It seems to be ascribed that these clusters are not stable, or that ionization potentials of these clusters is higher than photon energy of an ArF laser, 6.42 eV.

Time of flight mass spectrum measured at a detection chamber is shown in Fig.

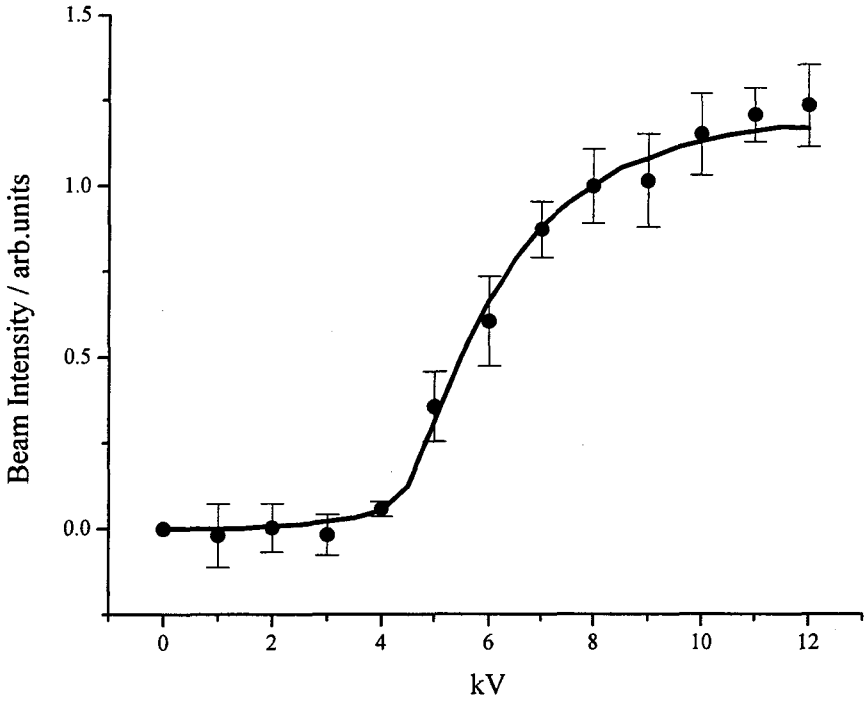

Figure 4-3-4. Focusing curve of $Ti_1(C_6H_6)_1$ seeded in He. The closed circles are experimental data, while the solid line is a trajectory simulation assuming a dipole moment of 2.4 D.

4-3-3. It was confirmed that signals correspond to (1,1) and (1,2) clusters observed as well as before. Mass resolution is much better than that at a buffer chamber because of the longer ion drift region. The results indicate that both clusters are stable in the

molecular beam and have longer lifetime than several milliseconds, which roughly corresponds to a flight time from a cluster source to a detection point.

Figure 4-3-4 shows the focusing curve of $Ti_1(C_6H_6)_1$ cluster at 700 Torr stagnation pressure of He carrier gas and 70 Torr of benzene. It is easily recognized that there is a vast focusing effect at higher hexapole voltages. It indicates that this cluster has a symmetric top structure with higher symmetry than C_{3v} symmetry and that experiences a first Stark effect in the hexapole field. In trajectory simulation, we took into account rotational states up to $J = 15$, $K = 15$, and assumed observed translational temperature was equal to the rotational temperature as usual. The only one parameter to reproduce the experimental focusing curve was an electric dipole moment of the cluster. It was found that rotational temperature was not so sensitive in the fitting procedure of the experimental data. The optimized dipole moment was 2.4 D for the $Ti_1(C_6H_6)_1$ cluster. Exactly the same procedure was applied to $V_1(C_6H_6)_1$ cluster and determined its dipole moment as 1.0 D. For these early transition metal-C_6H_6 clusters showed large focusing behavior at higher hexapole voltages. Although we applied the same methodology to the late transition metal with benzene binary clusters, focusing effect was so small that only the upper limit of dipole moment could be estimated. All the determined dipole moments of $M_1(C_6H_6)_1$ clusters are summarized in Table 4-3-1.

Table 4-3-1. Summary of experimentally determined dipole moment of $M_1(C_6H_6)_1$ cluster

$M_1(C_6H_6)_1$	$\mu_{exp.}$ / D
Ti	2.4 ± 0.3
V	1.0 ± 0.3
Co	< 0.4
Ni	< 0.6

For all the simulations, we assumed that $M_1(C_6H_6)_1$ cluster has a symmetric top structure, it means that a metal atom lies on the C_6 rotational axis of benzene. Although $Al_1(C_6H_6)_1$ cluster has two structural isomers, that is, η^2 and η^6, there have never reported on corresponding η^2 isomer for transition metal with benzene cluster so far. It is important to realize that in case of η^2-type cluster of $Al_1(C_6H_6)_1$, p-orbitals of both metal and benzene are expected to play a central role for bonding and stabilization. This is not peculiar to the case for transition metal-C_6H_6 binary clusters, therefore our assumption above is quite reasonable.

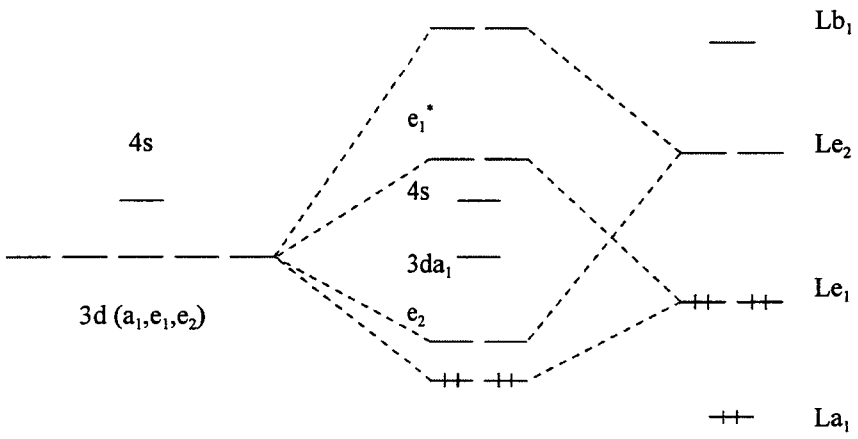

Figure 4-3-5. Schematic orbital interaction diagram with the extended Hückel method for $M_1(C_6H_6)_1$. Only ligand electrons are shown in figure, and the metal valence electronic configurations are determined by the Aufbau principle.[10,11]

It is generally expected that molecules in the condensed phase be in the ground states. It is also true that $M_1(C_6H_6)_1$ clusters under our experimental conditions are generated in the electronic ground states as proved in the previous sections. Figure 4-3-5 shows the orbital interaction diagram of $M_1(C_6H_6)_1$ cluster, where 3d orbitals of a metal atom were divided into one $3da_1$ (dz^2), two de_1 (dxz and dyz), and two de_2 (dxy

and dx^2-y^2) orbitals when molecular z axis was defined as to coincide with the C_6 axis of benzene. L indicates the molecular orbitals of a benzene molecule. Thus, electrons most favor to occupy the de_2 orbitals, as this maximizes the attractive interaction with Le_2 orbitals. A $3da_1$ AO of a transition metal does not have a strong interaction with La_1 orbital of a benzene molecule since it directs to the "hole" in the center of benzene and it has a negligibly small interaction with the La_1 orbital. Therefore, the $3da_1$ orbital then remains as the non-bonding atomic $3da_1$ orbital in $M_1(C_6H_6)_1$. Due to the symmetry, it is not possible to donate into the Lb_1 orbital. It is easy to recognize that electrons of early transition metal with benzene clusters do not have to occupy e_1^* anti-bonding orbital in the electronic ground state while on the other hand, electrons of corresponding clusters of late transition metals have to occupy e_1^* even in the electronic ground state.

It should be noted that $Le_1 \rightarrow de_1$ donation and $de_2 \rightarrow Le_2$ back-donation within M- C_6H_6 complex play a significant role to stabilize the complex for the early transition metals. However, only $de_2 \rightarrow Le_2$ back-donation stabilizes the late transition metal-C_6H_6 complexes. Since the e_1^* orbital is already occupied by electrons of the late transition metal, the donation from Le_1 MO seems unlikely.

Classically, as charges such as η_1, η_2, ... are distributed on coordinates, $\boldsymbol{r}_1$, $\boldsymbol{r}_2$, ... in a molecule, an electric dipole moment of the molecule is written as well-known formula:

$$\mu = \sum_i \eta_i \boldsymbol{r}_i$$

Quantum mechanically, it is a expectation value and it can be expressed as:

$$\mu = -e\int \Phi^* \sum_i \boldsymbol{r}_i \Phi d\tau + e\sum_\mu Z_\mu \boldsymbol{R}_\mu$$

where Φ is the total wavefunction of an electron, r_i is the i-th electron coordinate, R_μ expresses μ-th coordinate of a nuclei. The latter term expresses a dipole moment due to charged nucleus. Each molecular orbital ϕ_i can be expanded by the LCAO approximation. Then,

$$\int \Phi^* \sum_i \boldsymbol{r}_i \Phi d\tau = \sum_i v_i \int \varphi_i^*(1)\boldsymbol{r}(1)\boldsymbol{R}_\mu \varphi_i(1) d\boldsymbol{r}_I$$

$$= \sum_s \sum_i v_i C_{is}^{\ 2} \int \chi_s^*(1)\boldsymbol{r}(1)\chi_s(1) d\tau_1 + 2\sum_{s>t} \sum_i v_i C_{is} C_{is} \int \chi_s^*(1)\boldsymbol{r}(1)\chi_t(1) d\tau_1$$

$$= \sum q_s \langle s|\boldsymbol{r}|s\rangle + 2\sum_{s>t} p_{st} \langle s|\boldsymbol{r}|t\rangle$$

where $\langle s|\boldsymbol{r}|t\rangle$ is a so-called dipole moment integral. It is known that this integral can be divided into a π-dipole moment and a σ-dipole moment, which result from the localization of π and σ electrons, respectively. It is known that bond character of $3da_1$, e_1, and e_2 orbitals are able to be classified as σ-, π-, and δ-bond, respectively. As mentioned above, $3da_1$ orbital does not play so much for stabilizing $M_1(C_6H_6)_1$ cluster. As a result, a σ-dipole moment contributes only small amount to electric dipole moment. Then, we could only observe very small dipole moment of a late transition metal with a benzene molecule cluster. On the other hand, a π-dipole moment also must be taken into account in the case of the early transition metal clusters since de_1-Le_1 interaction occurs for the early transition metal in $M_1(C_6H_6)_1$ cluster. In fact, dipole moments of these

clusters become larger. It suggests that π-dipole moment is larger than σ-dipole moment in the clusters of the early transition metals. This is the first determination of the dipole moment of these clusters and enables us to obtain the bonding characters of the clusters.

References

1. C.S. Yeh, K.F. Willey, D.L. Robbins, J.S. Pligrim, M.A. Duncan, *Chem. Phys. Lett.*, **233**, 196 (1992).
2. P.M. Holland, A.W. Castleman, *J. Chem. Phys.*, **76**, 4195 (1982).
3. E.S. Robels, A.M. Ellis, T.A. Miller, *J. Phys. Chem.* **96**, 8791 (1992).
4. F. Misaizu, M. Sanekata, K. Fuke, S. Iwata, *J. Chem. Phys.*, **100**, 1161 (1994).
5. B.S. Larsen, D.P. Ridge, *J. Am. Chem. Soc.*, **106**, 1912 (1984).
6. D.B. Jacobson, B.S. Freiser, *J. Am. Chem. Soc.*, **107**, 1581 (1986).
7. K. Hoshino, T. Kurikawa, H. Takeda, A. Nakajima, K. Kaya, *J. Phys. Chem.*, **99**, 3053 (1995).
8. M. Hirano, K. Judai, A. Nakajima, K. Kaya, *J. Phys. Chem. A*, **101**, 4893 (1997).
9. T. Kurikawa, M. Hirano, H. Takeda, K. Yagi, K. Hoshino, A. Nakajima, K. Kaya, *J. Phys. Chem.*, **99**, 16248 (1995).
10. T. Yasuike, A. Nakajima, S. Yabushita, K. Kaya, *J. Phys. Chem. A*, **101**, 5360 (1997).
11. T. Yasuike, S. Yabushita, *J. Phys. Chem. A*, **103**, 4533 (1999).
12. M.J. Frisch, G.W. Trucks, H.B. Schlegel, P.M.W. Gill, B.G. Johnson, M.A. Robb, J.R. Cheeseman, T. Keith, G.A. Petersson, J.A. Montgomery, K. Raghavachari, M.A. Al-Laham, V.G. Zakrzewski, J.V. Ortiz, J.B. Foresman, J. Cioslowski, B.B. Stefanov, A. Nanayakkara, M. Challacombe, C.Y. Peng, P.Y. Ayala, W. Chen, M.W. Wong, J.L. Andres, E.S. Replogle, R. Gomperts, R.L. Martin, D.J. Fox, J.S. Binkley, D.J. Defrees, J. Baker, J.P. Stewart, M. Head-Gordon, C. Gonzalez, and J.A. Pople, GAUSSIAN 94, Revision D.2, Gaussian, Inc., Pittsburgh, PA, 1995

13. D.M.P. Mingos, "*Comprehensive Organometallic Chemistry*", 1st. Eds. G. Wilkinson, F.G.A. Stone, E.W. Abel, Eds.; Pergamon press: New York, vol. **3**, Chapter 19, (1982).

Chapter 4 is mainly based on the following articles:

K. Imura, T. Kawashima, H. Ohoyama, T. Kasai, *J. Am. Chem. Soc.*, to be submitted.

K. Imura, T. Kawashima, H. Ohoyama, T. Kasai, *J. Chem. Phys.*, to be submitted.

T. Kawashima, K. Imura, H. Ohoyama, T. Kasai, *J. Phys. Chem. A*, to be submitted.

Chapter 5 The Reaction of size-selected HCl dimer with Ne^* atom

5-1 Introduction

It is known that the reaction of Ne(^3P) with HCl molecule produces the electronically excited $HCl^+(A)$ in $v' = 2, 1, 0$ vibrational state.[1,2,3,4,5] Although many researches suggested that reaction of HCl clusters with Ne* would not produce $HCl^+(A)$ results from the competition with other channel, it has never done on the reaction of HCl clusters with Ne*, due to the difficulty of neutral HCl cluster size selection. In the line study of HCl cluster reactivity, very recently, Naaman and co-workers indicated that these reactivity drastically depended on the counter reactant. In case of the reaction with O(^3P), reactivity of HCl cluster enhanced more than two order of magnitude and produced rotationally cold products compared with that of HCl monomer.[6] On the other hand, reaction with O(^1D), both reactivity and internal energy distribution of products were not affected at all because of the incorporation of HCl into a van der Waals complex. McCoy and co-workers have performed quasiclassical trajectory calculation on these systems.[7] It is found that when the van der Waals complex is longer lived than the collision complex, rotational and vibrational cooling are observed. In contrast, when the dissociation of the van der Waals complex is prompt, compared to the collision complex lifetime, the effects of complex formation on the internal energy of the product become negligible. In case of title reaction, we can not discuss the reactivity change due to clusterization, since many other channels would be opened, nevertheless, some dynamical aspect of HCl dimer can be extracted from the observation of the internal distribution of reaction products. In this section, Penning ionization optical spectroscopy was performed to investigate the dynamics of title reaction.

5-2 Experimental

For the spectroscopic measurement, the crossed molecular beam apparatus has been used. It consists of three deferentially pumped chambers, metastable source, buffer, and detection. In the source chamber, metastable Ne atoms were generated by the glow discharge in the supersonic expansion. At the buffer chamber, ion species were removed by the reflector. Molecular beams were intersected each other at the detection chamber, and then chemiluminescence from reaction products were detected by a photomultiplier after passing through monochromator. Typically, emission were accumulated several hundred shots at each wavelength by using a gated photon counting techniques and swept in the range from 310 to 380 nm. In addition, we measured the chemiluminescence arising from the reaction of size selected HCl dimer by using a 60 cm long hexapole field with Ne^*. It is easy to realized that signal comes from dimers depends on the hexapole biased voltage. Namely, emission enhancement due to hexapole applied voltage was assigned to only due to HCl dimer intensity increase in the beam. For this measurement, instead of monochromator, optical filter was used because of very poor emission signal intensity.

5-3 Results and discussion

Fluorescence spectra of reaction product were obtained at 40 and 70 Torr stagnation pressure of HCl. Spectrum for lower stagnation pressure could be reproduced using reported vibrational and rotational distribution in the usual manner. It is found that internal distribution of product is consistent with that of monomer. Alternatively

spectrum was measured at higher stagnation pressure of HCl, therefore higher cluster formation is likely. Obtained spectrum could be reproduced as same manner as before except rotational vibrational distribution. At this reaction condition, internal distribution was found to be less internally excited than that of monomer. This observation seems that reaction with HCl clusters leads to less internally excited products. The results are summarized in Table 5-1.

Table 5-1. Relative vibrational populations and rotational temperature of $HCl^+(A)$ product at lower and higher HCl stagnation pressures.

HCl pressure / Torr	Relative Population			Rotational Temperature / K		
v =	0,	1,	2	0,	1,	2
40	55 ± 10	100	85 ± 15	800 ± 200	750 ± 200	450 ± 150
70	70 ± 15	100	80 ± 15	500 ± 100	450 ± 200	350 ± 150

The size selected reaction study can directly investigate if the HCl dimer can produce the HCl^+ ion. The fact, signal increases with increasing the hexapole applied voltage, is that a clear evidence that HCl dimer can produce HCl^+ as well as HCl monomer. Base on these findings, we propose following reaction mechanism for HCl dimer penning ionization with Ne^*.

$$Ne^* + (HCl)_2 \rightarrow [Ne\cdots(HCl)_2]^{**}$$
$$\rightarrow [Ne\cdots HCl^+(A)\cdot HCl] + e^-$$
$$\rightarrow Ne + HCl^+(A)\cdot HCl + e^-$$
$$\rightarrow Ne + HCl^+(A) + HCl + e^-$$

First, reactants form reaction complex, and immediately one of the cluster moiety will be ionized. It probably occurs within ps order. Before cluster dissociate into the products, dissociation of reaction complex would occur. This is the only case we can observe internally cold distribution of products for reaction involving cluster.

Very recently, Castleman and coworkers studied the dissociation of HCl dimer.[8] Dimer was photo ionized by three photons regime (13.81 eV). They proposed that the dissociation of the dimer $(HCl)_2^+$ could occur through the following two channels:

$$(HCl)_2^+ \rightarrow (H_2Cl)^+ + Cl$$

$$(HCl)_2^+ \rightarrow (HCl)^+ + HCl$$

Because of the small difference between the reaction barriers involved in the above mentioned dissociation channels, both should be observable in the dissociation process, with the Cl loss channles more favored. However, only the HCl^+ fragment was clearly identified. While energy of Ne^* is about 3 eV larger, our experimental observation of HCl^+ fragment is constent with the results of photo dissociation study. It is very interesting that both experiment produced same fragment. It seems to be a token that at the Penning ionization, ionization occurs relatively long impact parameter and the de-excitation of metastable rare gas atom would not affect so much following reaction proceedings. These findings supports our proposed mechanism again.

From the study of reaction of HCl dimer with Ne^*, it was revealed that HCl dimer could also produce $HCl^+(A)$ as well as HCl monomer, although it was believed that dimer would not produce it.

References

1. A.A. Navarro, B. Brunetti, S. Falcinelli, M. Gonzalez, and F. Vecchiocattivi, *J. Chem. Phys.*, **96**, 433 (1992).
2. B. Brunetti, R. Cambi, S. Falcinelli, J.M. Farrer, and F. Vecchiocattivi, *J. Phys. Chem.*, **97**, 11877 (1993).
3. H.L. Snyder, B.T. Smith, and R.M. Martin, *Chem. Phys. Lett.*, **94**, 90 (1983).
4. G.W. Tyndall, M.S. de Vries, and R.M. Martin, *Chem. Phys. Lett.*, **110**, 400 (1984). M.S. de Vries, G.W. Tyndall, and R.M. Martin, *J. Chem. Phys.*, **80**, 1366 (1984).
5. M. Tsuji, J.P. Maier, H. Obase, Y. Nishimura, *Chem. Phys. Lett.*, **110**, 17 (1986).
6. Y. Hurwitz, P.S. Stern, R. Naaman, A.B. McCoy, *J. Chem. Phys.*, **106**, 2627 (1997).
7. A.B. McCoy, M.W. Lufaso, M. Veneziani, S. Atrill, R. Naaman, *J. Chem. Phys.*, **108**, 9651 (1998).
8. Q. Zhong, L. Poth, J.V. Ford, A.W. Castleman Jr., *Chem. Phys. Lett.*, **286**, 305 (1998).

Chapter 4 is mainly based on the following articles:

K. Imura, H. Ohoyama, T. Kasai, *Chemistry letters* to be submitted.

Chapter 6 The Reaction of $O(^1D)$ with H_2O, D_2O Monomers and Clusters and the Intracomplex Reaction in N_2O-X_2O (X = H, D) Photo-initiated at 193 and 212.8 nm.

6-1 Introduction

Reaction of $O(^1D)$ with water monomers and clusters has been studied extensively owing to its importance in atmospheric and combustion chemistry, and because of its interesting dynamics. One can distinguish two types of processes, the bimolecular reaction in which a free oxygen atom reacts with a molecule or cluster, or intracluster process in which the reaction is induced inside a single complex. In most of these studies the $O(^1D)$ atoms has been produced by dissociating either ozone at 248 or 266 nm or N_2O at 193 nm. As a continuation of ongoing study on the effect of cluster formation on the reactions of $O(^1D)$ atoms, we visited some of these studies and explored the reaction of this atom with both H_2O and D_2O monomers and clusters at different kinetic energies and the intracluster reaction in N_2O-X_2O (X= H, D) photo-initiated both at 193 and at 212.8 nm.

The reaction of $O(^1D)$ with H_2O monomer has been studied by monitoring the OH product and its internal energy.[1,2,3] Two "types" of OH are formed in the process, the "new" OH and the remained OH from the water molecule, the "old" one. In some of the experiments, these species have been probed separately by isotope substitution. Despite the multiple studies, no conclusion has been reached regarding the reaction mechanism. While one study concluded that the reaction occurs through a relatively short lived collision complex and insertion of the $O(^1D)$ into the water molecule,[1] another study suggested that a long-lived insertion complex or direct stripping mechanisms can be ruled out, and no evidence to support any archetype mechanism (insertion or abstraction) could be found.[2]

The reaction of $O(^1D)$ with water clusters in a crossed molecular beam revealed

a distinct cluster size dependence of the rotational energy distribution of the OH product.[4] The intracluster reactions were investigated either by photodissociating the ozone in the O_3-H_2O cluster with 266 nm laser[5] or by photodissociation of N_2O in the N_2O-H_2O complex with 193 nm laser.[6] In all the reported reactions of clusters, either intra-complex or in crossed beam, the rotational temperature of the OH products was found to be colder than in the monomeric process. Recently it has been shown that this "rotational cooling" is not a result of geometrical restriction but rather a result of rotational to translational energy transfer in the collision complex.[4] This effect occurs whenever the OH product leaves the collision complex first, before all other components. The affect of van der Waals complex on vibrational energy distribution is by far less established. While, in the case of O_3-H_2O dissociation at 266 nm, the OH product was found to be much colder vibrationally than the product obtained from the monomeric process,[5] in the case of N_2O-H_2O photodissociation at 193 nm, OH in $v = 1$ was reported.[6]

In what follows we shall present results on the energy distribution of OH and OD obtained by photodissociating N_2O-H_2O and N_2O-D_2O respectively, at 193 and 212.8 nm. The results will be compared to that obtained from the monomeric processes. The fact that in the current study the experiments were performed at two collision energies allows us to provide more insight on the reaction mechanism for the monomer.

6-2 Experimental

The experimental system has been described in Chapter 2. The molecular beam was produced by expanding a mixture of N_2O and H_2O or D_2O, whose reservoir

temperature was kept at 298 K, through a 10 Hz pulsed nozzle (general valve, 0.5 mm diameter). The pressure in the reaction chamber was kept below 5 x 10^{-5} Torr. The $O(^1D)$ atoms were produced by photolysis of N_2O either by ArF excimer laser (Lamda physics, COMPEX) at 193 nm or by the 5th harmonic of a Nd:YAG laser at 212.8 nm. After certain time delay, frequency doubled dye laser (surforhodamine 640 or DCM pumped by second harmonic of YAG) with BBO crystal was fired to excite the OH or OD products. The photolysis (pump) and the probe laser beams were counter propagated through buffles arms and intersect the molecular beam at about 8 mm downstream from the nozzle.

The detection of the OH and OD was performed through the laser induced fluorescence spectrum of the $A\ ^2\Sigma^+$ - $X\ ^2\Pi$ transition, either through the 0-0 or 1-1 manifold, for monitoring the $v = 0$ or $v = 1$ population respectively. The probe pulse energy was kept at 40 μJ in a 2 mm diameter beam, to prevent saturation. The fluorescence was detected by a photomultiplier (HAMAMATSU, R562) with optical narrow band pass filter (centered at 312.8 nm, or 311.8 nm) positioned perpendicular to the molecular and laser beams. The signal was processed by a boxcar integrator and transferred to a computer. The delay time between the two lasers was adjustable with a digital delay generator.

The rotational populations of the OH or OD products were determined from LIF signal intensity by using line assignments,[8] tabulated Einstein coefficients[9] and the LIF detection efficiency. (Einstein coefficients for (1-1) band of OD were calculated from the expression given in Ref. 9). We assumed that the life time of the excited OH and OD does not vary for the rotational states probed. This assumption is justified based on studies shown change in lifetime only for $N > 15$.[10]

At the experimental condition applied in this study and with maximum pump-probe laser delay of 600 ns, only less than 2% of the excited OH (or OD) molecules are suffering from collisional quenching.[11] Hence, we do not expect to observe any collision effect on the populations of rotational and vibrational levels in the OH (or OD) within our experimental uncertainty.

6-3 Results

6-3.1 Photodissociation at 193 nm

When a beam containing a mixture of N_2O and H_2O is exposed to a 193 nm laser, OH can be formed through several processes.

1. $H_2O + h\nu(193\ nm) \rightarrow OH\ (v,N) + H$

2. $H_2O + N_2O + h\nu(193\ nm) \rightarrow OH\ (v,N) + H + N_2O \rightarrow OH(v,N) + OH(v',N') + N_2$

3. $H_2O + N_2O + h\nu(193\ nm) \rightarrow H_2O + N_2 + O \rightarrow OH(v,N) + OH(v',N') + N_2$

4. $(H_2O)_m + (N_2O)_n + h\nu(193\ nm) \rightarrow (H_2O)_{m-1} + OH\ (v,N) + H + (N_2O)_n \rightarrow$
$OH\ (v,N) + OH(v',N') + (N_2O)_{n-1} + N_2$

5. $(H_2O)_m + (N_2O)_n + h\nu(193\ nm) \rightarrow (H_2O)_m + (N_2O)_{n-1} + O + N_2 \rightarrow (H_2O)_{m-1} +$
$OH\ (v,N) + OH(v',N') + (N_2O)_{n-1} + N_2$

6. $H_2O{\cdot}N_2O + h\nu(193\ nm) \rightarrow OH\ (v,N) + H + N_2O \rightarrow OH(v,N) + OH(v',N') + N_2$

7. $H_2O{\cdot}N_2O + h\nu(193\ nm) \rightarrow H_2O + N_2 + O \rightarrow OH(v,N) + OH(v',N') + N_2$

8. $(H_2O)_m{\cdot}(N_2O)_n + h\nu(193\ nm) \rightarrow (H_2O)_{m-1} + OH\ (v,N) + H + (N_2O)_n \rightarrow$
$OH\ (v,N) + OH(v',N') + (N_2O)_{n-1} + N_2$

9. $(H_2O)_m{\cdot}(N_2O)_n + h\nu(193\ nm) \rightarrow (H_2O)_m + (N_2O)_{n-1} + O + N_2 \rightarrow$

$(H_2O)_{m-1} + OH\ (v,N) + OH(v',N') + (N_2O)_{n-1} + N_2$

From the results discussed below we will prove that direct dissociation of water is not contributing significantly to our observations. Hence, processes number 1,2, 4 and 6 from the above list can be excluded. Based on pressure dependence studies we will

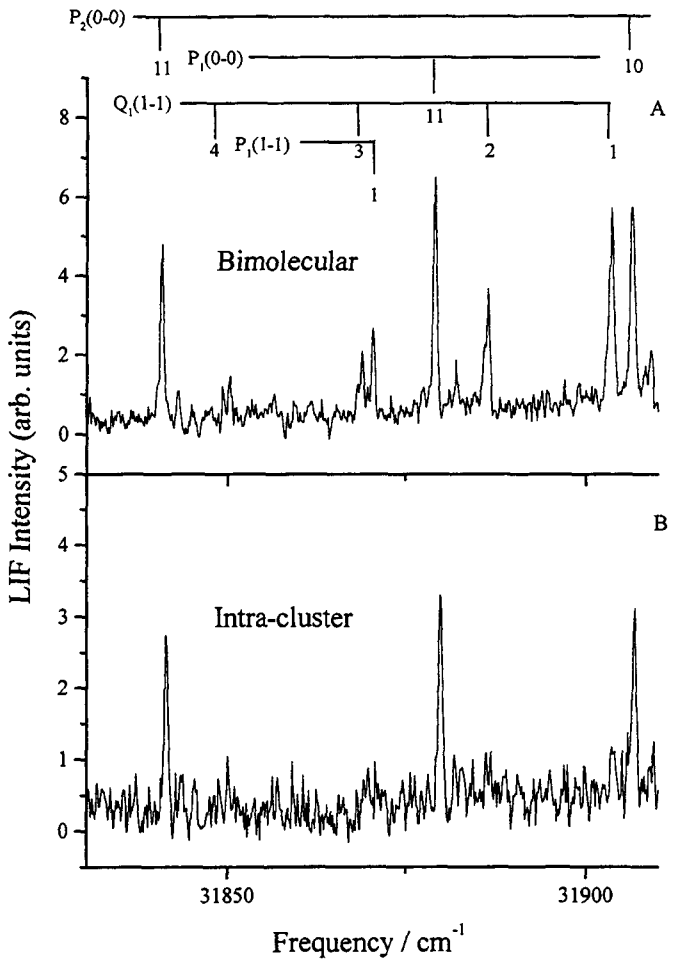

Figure 6-1. Part from the LIF spectra of OH(v = 0,1) obtained for delay of 600 ns (A) and 200 ns (B) between the pump and probe lasers. Note the differences in the intensity of lines belonging to OH(v = 1) in the two cases.

suggest that process number 5 is not contributing to the signal and that we study either the bimolecular reaction (process number 3) or the intracluster reaction (process no. 7).

In what follows we shall discuss each possibility and will attempt to relate the observed OH internal energy distribution to a specific process. The same discussion is

valid for D_2O.

We have studied separately the photodissociation of water at 193 nm and found a very cold rotational distribution in OH produced from H_2O.[12] OH only up to $N = 6$ is

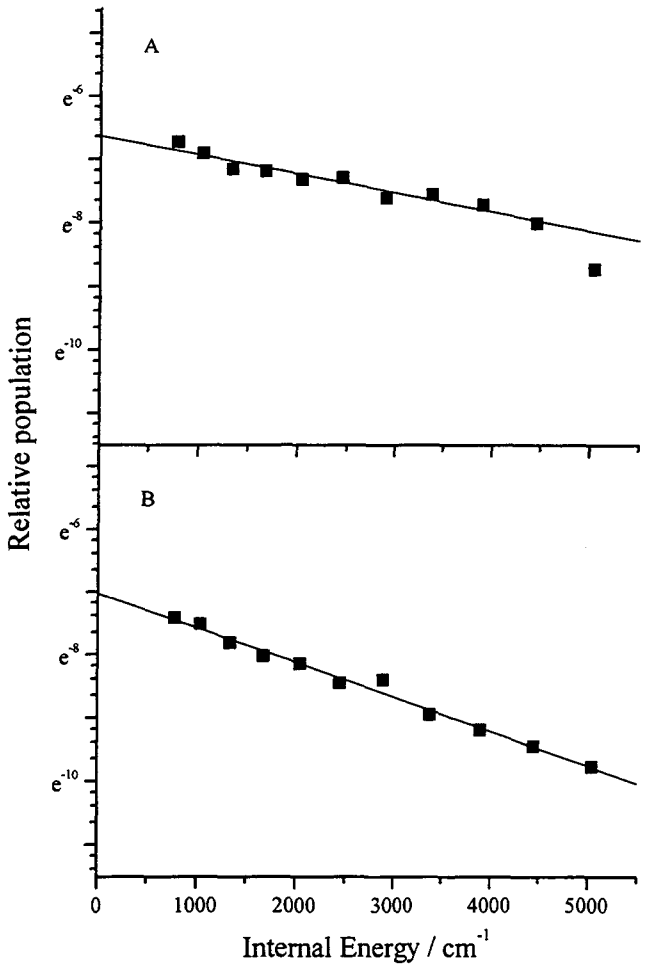

Figure 6-2. The rotational distribution of OH obtained for delay of 600 ns (A) and 200 ns (B) between the pump and probe lasers. The Q_1 branch was monitored. The solid line, derived from linear least square fit, represents the Boltzmann distribution that can be fitted by a rotational temperature of 5000 K, (A), and 2600 K, (B).

formed and therefore in the analysis of the reaction product the low rotational states were ignored. The absorption cross section of D_2O at 193 nm is smaller by about factor of 64 compared to H_2O,[13] hence its contribution to the observed OD signal is even

smaller.

Figure 6-1 shows the laser induced fluorescence spectrum of OH obtained by monitoring the 0-0 and 1-1 transitions at different delays between the photodissociation and probe lasers. An apparent reduction in the population of $v = 1$ is seen upon changing the delay from 600 to 200 ns (Fig. 6-1 A and B respectively).

Figure 6-2 presents the Boltzmann plots of OH rotational populations in $v = 0$ for 600 and 200 ns delay between the pump and probe lasers. In the case of long delay (Fig. 6-2 A) the rotational distribution can be fitted to 5000 K, while for the short delay

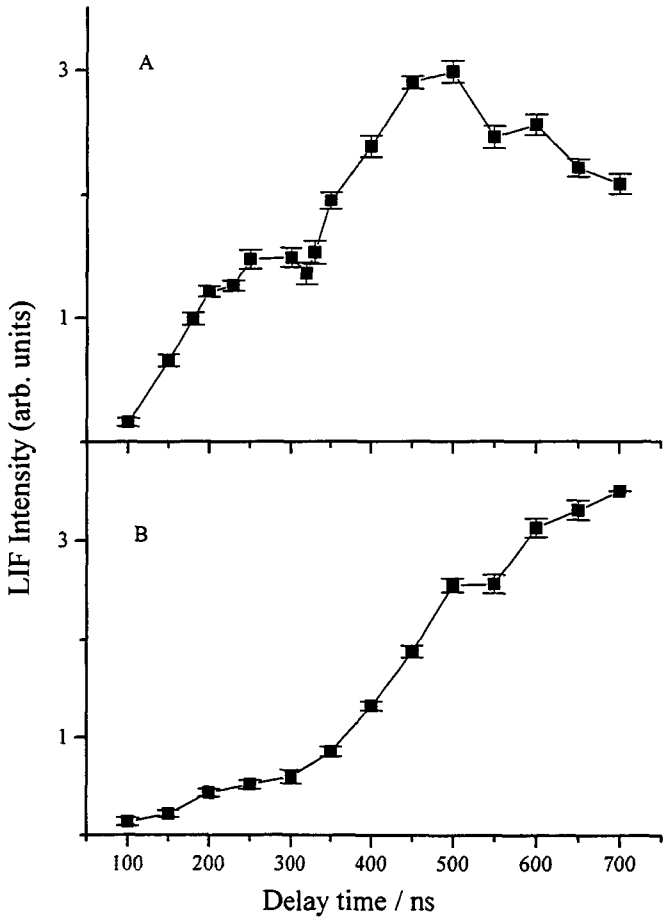

Figure 6-3. The intensity of the $P_2(10)$ transition in OH($v = 0$) (A), and the $Q_1(1)$ transition in OH($v = 1$) (B) as a function of the delay between the pump-probe lasers.

(Figure 6-2 B) it fits 2600 K (see Table 6-1). In the case of D_2O the distributions could be fitted to about 2500 K and 2000 K for the long and short pump-probe delays respectively.

Figure 6-3 A shows the $P_2(10)$ line intensity dependence upon the pump-probe laser delay measured at stagnation pressure of 60.0 kPa. A clear bimodal distribution is seen with one peak at about 250 ns and the second at about 500 ns. Figure 6-3 B shows

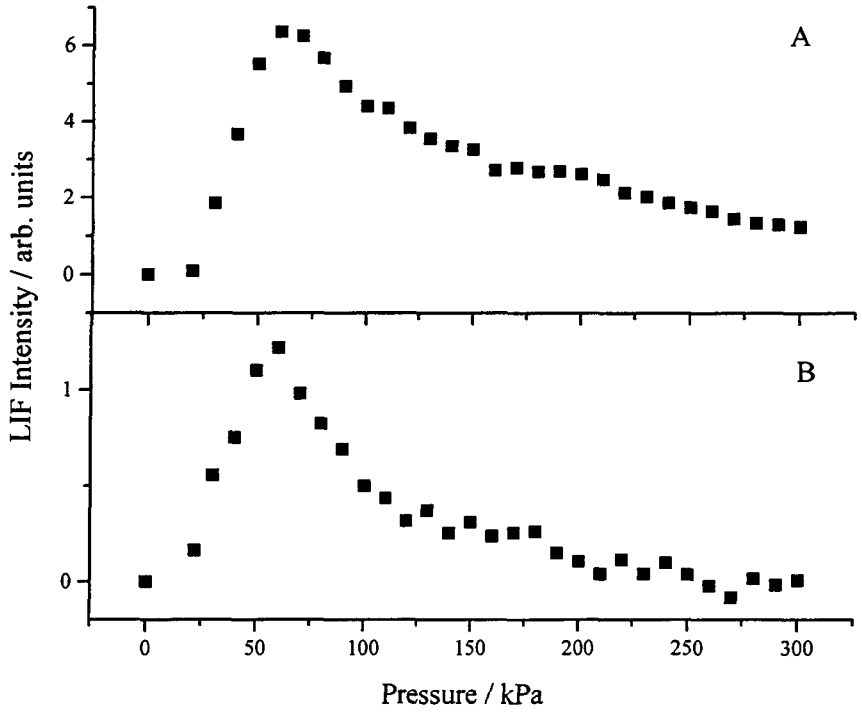

Figure 6-4. The pressure dependence of the signal obtained by probing the $Q_1(1)$ transition from the vibrational ground state at pump probe laser delay of 600 ns (A) and 200 ns (B). The experiments were carried out with a constant water pressure of 3.5 kPa and by increasing the N_2O pressure.

a similar measurement obtained when the $Q_1(1)$ transition is monitored, in the first vibrational excited state. Up to 300 ns the OH signal rises very slowly while after a delay of about 300 ns there is an apparent increase in the signal.

We interpret the observation in Fig. 6-3 as due to a switching between

intracluster reaction, occurring at a short delay and collision of the free atom with molecules in the beam that occurs at longer delay. This delay time is consistent with the signal increase due to bimolecular reaction in Fig. 6-3 A. This conclusion is consistent with the colder rotational and vibrational distributions obtained for the shorter delay time.

Figure 6-4 shows the pressure dependence of the signal obtained by probing

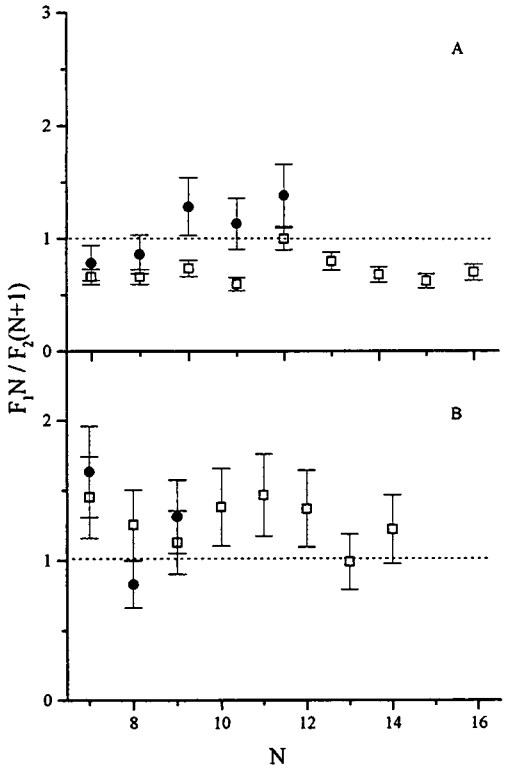

Figure 6-5. The ratio of spin-orbit component of OH (v = 0), obtained for a pump-probe delay of 600 ns (A), and 200 ns, (B). The signal is corrected with the statistical factor $N / (N + 1)$, where the results for the $\Pi(A')$ and $\Pi(A'')$ Λ states are presented as solid circle and open square, respectively. The dashed line represents the calculated statistical distribution.

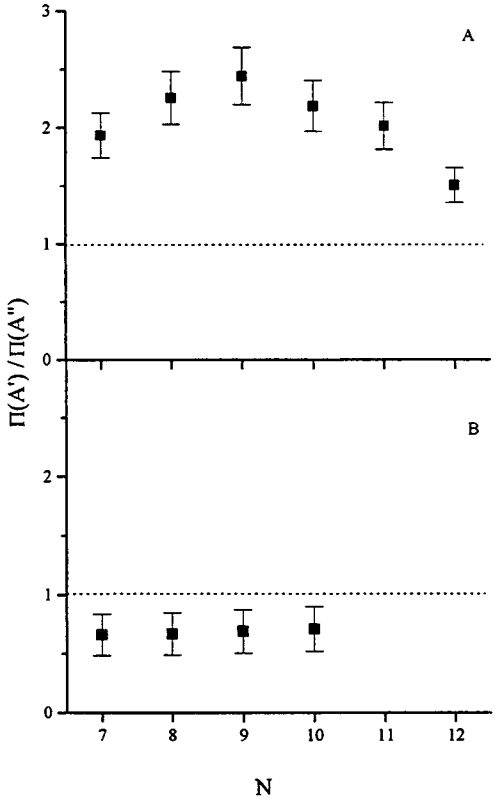

Figure 6-6. The Λ-doublet population ratio, $\Lambda(A') / \Lambda(A'')$ in OH(v = 0), obtained from delay of 600 ns (A) and 200 ns (B) between the of pump-probe lasers

the $Q_1(1)$ transition from the vibrational ground state at two different pump-probe delays. The experiments were carried out with a constant water pressure (3.5 kPa) and by increasing the N_2O pressure. The signal reached a peak at about the same pressure for both delays, at about 60 kPa. We have found before that large clusters of water do not produce OH following the reaction with $O(^1D)$.[4] Therefore we conclude that at about 60 kPa only relatively small clusters are formed. In order to verify it, the $P_2(10)$ transition dependence on the concentration of water and N_2O was examined by changing the temperature of water reservoir and by changing the concentration of N_2O. The signal was found to depend linearly on both concentrations within experimental error. This experiment was performed at both short and long delays. It indicates that at short delay the intracluster process is measured in the N_2O-H_2O complex, while at long delay the reaction of $O(^1D) + H_2O$ is monitored. Therefore also process (5) can be ruled out.

Figures 6-5 A and 6-5 B show the OH population ratio between the two spin orbit states $\Pi_{3/2}$ and $\Pi_{1/2}$, F_1 and F_2 respectively, for each Λ-doubling states, at a long and short pump-probe delays respectively. The ratios are corrected for the state degeneracy by $N/(N+1)$. A ratio of unity reflects complete statistical population. In the case of long pump-probe delay, namely collisions between oxygen atom and water molecules, the result indicates non-statistical distribution between the two spin orbit states only for the Λ-doubling A'' state. In this case we observe an average ratio of 0.8, indicating a preference for the population of the $\Pi_{1/2}$. In the case of intracluster reaction condition, there is small preference for populating the lower spin orbit state, $\Pi_{3/2}$ and the ratio is 1.2. In the case of OD no preference for the spin orbit states was found.

Figure 6-6 shows the OH Λ-doublet distribution ratios determined by utilizing the *P* and *Q* transitions in the vibrational ground states. Although the Λ(*A'*, *A''*) notation is meaningful only at higher rotational state, it is used here for all N states. In the case of long pump-probe delay, the bimolecular reaction has propensity to be formed the *A'* state, in agreement with the results obtained in the O_3 / H_2O system. However, in case of

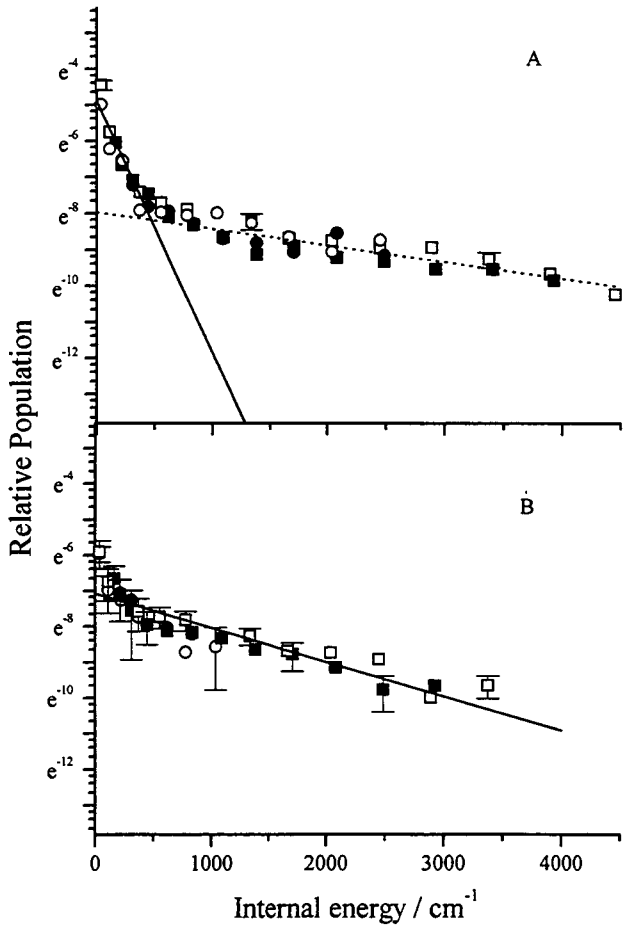

Figure 6-7. The rotational distribution of OH obtained by dissociation at 212.8 nm and a pump-probe laser delays of 600 ns (A) and 200 ns (B). The signal was by monitorring several branches P_1(○), P_2(●), Q_1(□), Q_2(■).

short pump-probe delay, intracluster reaction, there is small preference for populating the *A''* state. In the case of OD preference for the *A'* Λ-doubling component is observed

only for the long pump-probe delay. The ratio between the population in A' and A'', in this case, is about 1.5.

In the case of the bimolecular reaction, the ratio between the population in the $v = 1$ and $v = 0$ states in OH is 0.8 ± 0.2 and in OD is less than 0.05. For intracluster reaction we do not observe any vibrational excited OH products. This is in contrast with former study[6] despite our attempt to reproduce exactly the conditions at this study. The results obtained using 193 nm dissociation laser are summarized in Table 6-1.

6-3.2 Photodissociation at 212.8 nm

Figure 6-7 presents the rotational distribution of OH obtained for long (A) and short (B) pump-probe delays. In the case of long delay, bimolecular reaction condition, a bimodal rotation distribution is obtained which can be fitted by assuming two thermal distributions of 210 K and 2750 K. It is important to realize that at this energy water does not dissociate at all.[14,15] Since the absorption cross section of N_2O at this wavelength is about one order of magnitude smaller than that at 193 nm, small signal to noise ratio did not enable us to obtain the rotational distribution in the vibrational excited state with high precision. For the same reason we could not obtain the population ratio for the spin-orbit or Λ-doubling states in bimolecular and intracluster reactions. However, we roughly estimated the relative vibrational population in the bimolecular reaction by using Q_1, P_1, and R_1 series in the vibrational excited states. We found that the ratio of the population at $v = 1$ to the population at $v = 0$ to be 0.15 ± 0.08. In the case of the intracluster complex, no population in the vibrational excited state was found.

Table 6-1: Rotational temperature, T_R, and relative vibrational populations (ρ_1 / ρ_0) of OH produced by bimolecular and intracluster reactions induced by 193 nm photolysis laser

	This work		Ref. [1, 2]		
	Bimolecular	Intracluster	Bimolecular		Intracluster
$T_R(v = 0)$ / K	5000 ± 200	2600 ± 100	New	6000	1700
			Old	2600	1600
$T_R(v = 1)$ / K	2300 ± 300	-	New	2200	1700
			Old	2200	-
ρ_1 / ρ_0	0.8 ± 0.2	0	New	0.68	0.41
			Old	0.04	0

Table 6-2: Rotational temperature, T_R, and relative vibrational populations of OH and OD produced from bimolecular and intracluster reactions induced with 193 nm photolysis laser.

	$H_2O + O(^1D)$ at 193 nm		$D_2O + O(^1D)$ at 193 nm	
	Bimolecular	Intracluster	Bimolecular	Intracluster
$T_R(v = 0)$ / K	5000 ± 200	2600 ± 100	2520 ± 200	2060 ± 120
$T_R(v = 1)$ / K	2300 ± 300	-	less than 100	-
ρ_1 / ρ_0	0.82 ± 0.06	0	< 0.05	0
$F_1N / F_2(N+1)$	0.8 ± 0.2	1.20±0.08	1.15 ± 0.15	1.29 ± 0.14
$\Lambda(A') / \Lambda(A'')$	1.97 ± 0.10	0.70 ± 0.02	1.57 ± 0.10	0.950 ± 0.05

6-4 Discussion

Always when clusters are involved in reactions of neutral species, defining the actual species involved in the reaction is a major challenge. The situation becomes even more complex when the experiment is carried in a single beam arrangement. Luckily, in a state-resolved study, the energy distribution in the products and its dependence on the pressure behind the nozzle provides indications on the species involved in the reaction. From the results presented above we conclude the followings;

1. The OH / OD monitored resulted from reaction. The contribution of direct dissociation of water is minimal and has to be taken into account only at very low N states.

2. At the pressure applied (3.5 kPa water and 56.5 kPa N_2O), mainly water-N_2O one to one complexes are formed.

3. At the given pressure and short pump-probe lasers delay (200 ns), most of the OH is produced from intracluster reactions. We shall refer to this process as "intracluster" reaction.

4. At the given pressure and long delays (600 ns) most of the probed OH is produced from reaction of $O(^1D)$ (produced by dissociation of N_2O) with monomers of water. We shall refer to this process as "bimolecular reaction".

In what follows the discussion will be divided to the bimolecular process and the intracluster reaction. In Table 6-2 the results obtained from the bimolecular and from the intracluster processes are compared to results obtained in former studies. Table 6-3 compared the results obtained applying the two wavelengths.

Table 6-3: The observed rotational temperature and relative vibrational populations of OH produced from bimolecular and intracluster reactions at two different photodissociation wavelengths.

	193 nm		212.8 nm	
	Bimolecular	Intracluster	Bimolecular	Intracluster
$T_R(v = 0)$ / K	5000 ± 200	2600 ± 100	2800 ± 200	1500 ± 130
			210 ± 20	
$T_R(v = 1)$ / K	2300 ± 300	-	800 ± 500	-
ρ_1 / ρ_0	0.8 ± 0.2	0	0.15 ± 0.08	0
E_{avail} / kJ mol^{-1}	163.3		154.2	
v_{col} / km s^{-1}	3.10		2.74	

Appendix:

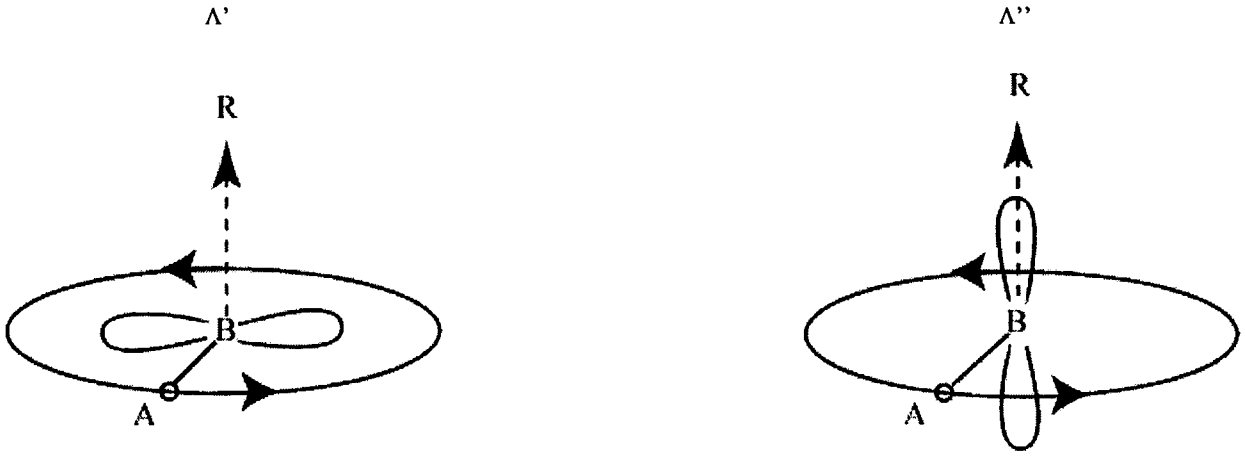

6-4.1 The bimolecular reaction

The experiments were performed at two different kinetic energies. When the dissociation is at 193 nm, the O(^1D) atoms are produced with a kinetic energy of 77.2 kJ/mol.[16] The kinetic energy of the oxygen was not measured directly for the case of dissociation at 212.8 nm, however Springsteen *et al.*,[17] suggested that energy partitioning in the photodissociation process does not change drastically between 193 nm and 205 nm. Since the absorption at 212.8 nm is also into the same continuum peaking near 182 nm,[18] we assumed that the energy partitioning is not changing drastically compared to that at 193 nm. Therefore, about 40% of the available energy is in the translational energy of the fragments. Hence, the kinetic energy of the O(^1D) atoms is about 60 kJ/mol. The average relative velocities in the collision of the oxygen atoms with H_2O are 2.7 km/sec and 3.1 km/sec for the atoms produced at 212.8 and 193 nm respectively.

Hanazaki *et al.* have studied this reaction and distinguished newly formed and old OH from the reaction by using isotopically labeled water molecules.[3] They found that newly formed OH has distributions of rotational and vibrational at a higher temperature. In our study we did not observe a distinct bimodal distribution of rotational energy (Figure 6-2 B), which is very close to the averaged distribution of the rotational energy for newly and old OH that they have reported. They reported that their experimental conditions were such that the products could collide before being detected. This collision did not affect, most probably, the rotational population but could affect the spin-orbit state population and the Λ-doubling population ratio.

Our present result is less affected by the collisional relaxation. Hence, the Λ states ratio shows the *A'* state has a small propensity to be produced in the reaction of

$O(^1D)$ with either H_2O or D_2O. Taking into account the OH vibrational excitation and the strongly non-statistical rotational population, we suggest that this reaction occurs through a non-planar transition state. The fact that the present study shows a drastic decrease, by almost a factor of five, in the vibrational excitation of OD following the reaction of $O(^1D)$ with D_2O compared to the reaction with H_2O farther supports our model. The near planar transition state model suggested in reference 3 would result in highly vibrational excited OD, similar to the vibrational excitation of the OH. The rate of Λ state population obtained was about two. As was discussed before this ratio indicates an unconstrained dynamics in which the OH (or OD) rotates almost freely in the transition state.[19] While this model can be adapted directly for the "old" OH, undoubtedly it is not valid for the newly formed OH in the reaction, whose rotational plane is determined by the velocity of the approaching oxygen atom. Therefore, we do not expect any propensity for Λ state for the "new" OH. Hence, the fact that some propensity is observed indicates that the actual propensity for the A' state is slightly larger than 2 in the "old" OH. These results again support a non-planar collision complex.

The other question remaining open from the previous studies is whether the reaction proceeds through abstraction or insertion mechanism. In order to distinguish between the two mechanisms, the dependence of the internal energy distribution in the products on the collision energy will be seen in the followings. In case of abstraction, strong correlation is expected between the vibrational energy deposited in the product and the collision energy, while in the case of insertion process, no dependence is expected. Our results clearly show that the population of vibrational energy in OH (v = 1) drops by a factor of five upon reducing the collision energy by 9 kJ/mole. Therefore,

we conclude that the reaction occurs by abstraction. The non-statistical energy distribution indicates that the lifetime of the collision complex is too short to redistribute the kinetic energy.

6-4.2 Intracluster reaction

Two important questions are raised regarding the intracluster reaction. The first one is for the relation between the structure of the complex and the energy distribution in the product and secondly what is the effect of the photodissociation wavelength on the reaction.

The structure of N_2O-H_2O has been studied experimentally and theoretically. Experimentally, the structure was determined using the molecular beam electric resonance technique.[20] A planar equilibrium structure as shown in Fig. 6-8 was suggested where the N_2O sub-unit is tilted by about 9° away from the T-shaped structure, and the C_{2v} axis of water sub-unit is at about 20° off the complex ***a*** axis. Recently *ab-initio* calculation were performed by using MP4(SDTQ)/6-311G** with Gaussian 92.[6]

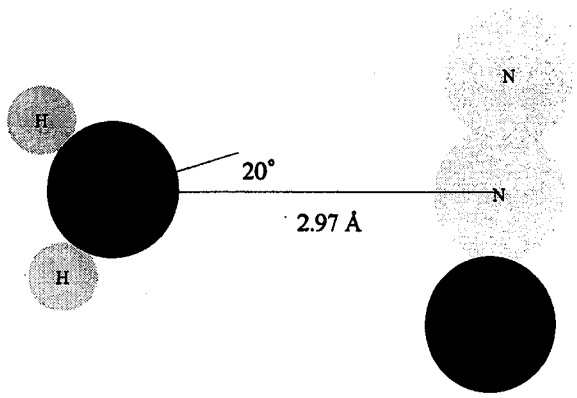

Figure 6-8. Schematic view of N_2O-H_2O cluster equilibrium structure, determined by experimentally.[19] Bond distance and angles are given in units of angstrom and degree, respectively.

As depicted in Fig. 6-9, it was found that all the atoms in the complex are in a plane. As is easily recognized from the two figures, the two suggested structures are very different, except for both being planar. Both of the structures cannot explain the observed products, since the oxygen atom of the N_2O unit is pointing away from the hydrogens on the water.

As suggested before the equilibrium structure of clusters does not have significant importance in assessing their reactivity because of their floppiness.[21] The fact that reactivity is observed suggests that either there is a large amplitude motion, most

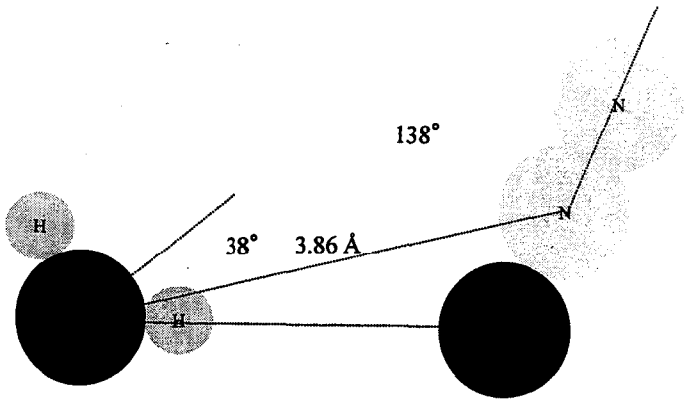

Figure 6-9. Schematic view of N_2O-H_2O cluster equilibrium structure, obtained by an *ab-initio* calculation.[6] Units are the same as those in Fig. 6-8.

probably of the hydrogens relative to the N_2O unit, or that the excited state of the complex has different conformation than its ground state. The photodissociation study of N_2O at 193 nm suggested that the dissociation occurred through a bent electronic state and its anisotropy parameter, β, was about 0.5.[16] This may cause the ejection of the oxygen atom with a perpendicular component of velocity with respect to the molecular axis. Therefore the ejected atoms is able to interact with the H_2O unit.

It is interesting to note that when the dissociation energy is reduced, the rotational temperature of the OH product drops almost at the same amount. This result

indicates that the reaction in this case occurs through a relative short-lived collision complex. This result is also consistent with the "rotational cooling" observed which indicates that the lifetime of the reaction complex is shorter than the culster lifetime itself.[7] Namely, the N_2 unit departs only after the OH product leaves the complex. In addition, we did not observe any vibrational excited product in the present study. This is remarkably different from the results in reference 6.

All the results mentioned above suggest that perhaps a major difference between the decomposition of free N_2O and complexed N_2O is the amount of energy deposited in the N_2 fragment. It seems that when the dissociation occurs in the life time of complex, more energy is deposited in the N_2, mainly as vibrational and rotational energies. If this is the case, two findings can be rationalized, the slow departure of the N_2 following the decomposition and the luck of vibrational energy in the OH product. The reason for these effects can be kinematics. While the decomposition of the free N_2O, the energy is partitioned based on the mass of a free oxygen atom, the effective mass of

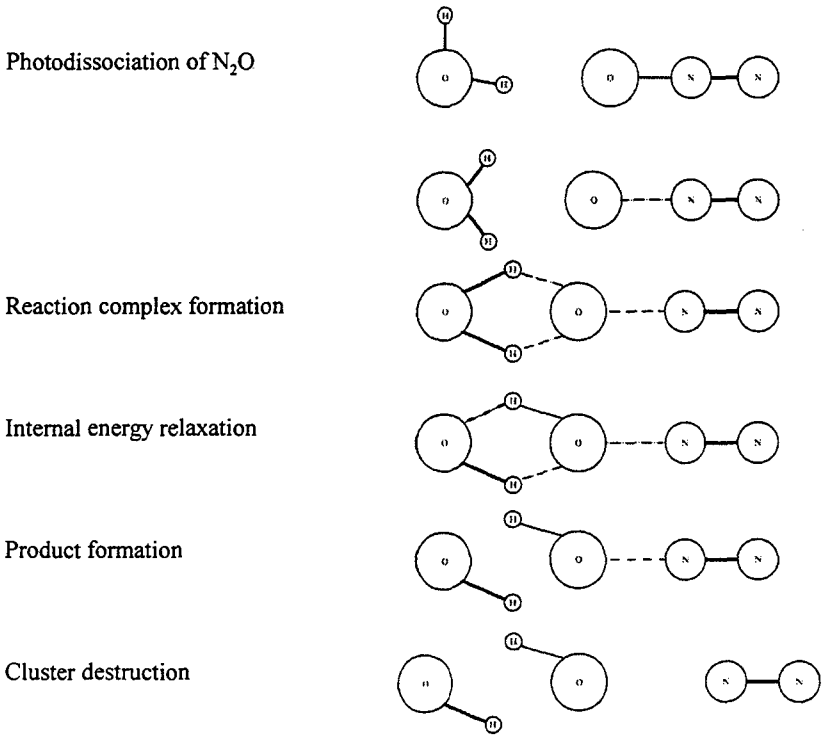

the oxygen may be larger, due to its interaction with the water in the complex and as a result less kinetic energy may be transferred to OH. Scheme of this reaction can be drown below.

6-5 Conclusion

We have re-examined the nascent product state distributions in the reaction of $O(^1D)$ with X_2O(X = H, D) photo-initiated by the dissociation of N_2O at 193 and 212.8 nm, and the corresponding photo-initiated intracluster reaction, N_2O-X_2O + $h\nu$ → N_2 + 2OX (X = H, D). The study at two different dissociation wavelengths allowed us to obtain direct information on the effect of initial collision kinetic energy on the energy distribution in the product.

Based on the new results, we conclude that the reaction of $O(^1D)$ with water occurs through abstraction mechanism with a relatively short lived collision complex. In the case of the intracomplex reaction, we have indication that more internal energy is deposited in the N_2 moiety, compared to the dissociation of an isolated N_2O. In addition the results indicate that the reaction between the oxygen atom and the water in the complex involved the formation of a short lived collision complex, with a lifetime of probably only few rotations of OH.

References

1. C.B. Cleveland and J.R. Wiesenfeld, *J. Chem. Phys.*, **96**, 248 (1992).
2. D.G. Sauder, J.C. Stephenson, D.S. King, and M.P. Casassa, *J. Chem. Phys.*, **97**, 952 (1992).
3. N. Tanaka, M. Takayanagi, and I. Hanazaki, *Chem. Phys. Lett.*, **254**, 40 (1996).
4. Y. Hurwitz, Y. Rudich, and R. Naaman, *Isr. J. Chem.*, **34**, 59 (1994).
5. D.S. King, D.G. Sauder, and M.P. Casassa, *J. Chem. Phys.*, **100**, 4200 (1994).
6. H.L. Kim, M. Takayanagi, and I. Hanazaki, *Chem. Phys. Lett.*, **222**, 431 (1994); N. Tanaka, U. Nagashima, M. Takayanaki, H.L. Kim, and I. Hanazaki, *J. Phys. Chem.*, **101**, 507 (1997).
7. A.B. McCoy, M.W. Lufaso, M. Veneziani, S. Atrill, and R. Naaman, *J. Chem. Phys.*, **108**, 9651 (1998).
8. G.H. Dieke and H.M. Crosswhite, *J. Quant. Spectrosc. Radiat. Transfer*, **2**, 97 (1962).; M.A.A. Clyne, J.A. Coxon, and A.R. Woon Fat, *J. Mol. Spectrosc.*, **46**, 146 (1973).
9. I.L. Chidsey and D.R. Crosley, *J. Quant. Spectrosc. Radiat. Transfer*, **23**, 187 (1980), R.A. Copeland, J.B. Jefefries, and D.R. Crosley, *Chem. Phys. Lett.*, **138**, 425 (1987), W.L. Dimpfl and J.L. Kinsey, *J. Quant. Spectrosc. Radiat. Transfer* **21**, 233 (1979), D.R. Crosley and R.K. Lengel, *J. Quant. Spectrosc. Radiat. Transfer* **17**, 59 (1977).
10. R.A. Sutherland and R.A. Anderson, *J. Chem. Phys.*, **58**, 1226 (1973).
11. C.B. Cleveland and J.R. Wiesenfeld, *Chem. Phys. Lett.*, **144**, 479 (1988).
12. K. Imura, N. Veneziani, T. Kasai, and R. Naaman, submitted to *Chem. Phys. Lett.*
13. D.F. Plusquellic, O. Votava, and D.J. Nesbitt, *J. Chem. Phys.*, **107**, 6123 (1997).

14. J.N. Harvey, J.O. Jung, and R.B. Gerber, *J. Chem. Phys.*, **109**, 8747 (1998).

15. D.F. Plusquellic, O. Votava, and D.J. Nesbitt, *J. Chem. Phys.*, **109**, 6631 (1998).

16. L.L. Springsteen, S. Satyapal, Y. Matsumi, L.M. Dobeck, and P.L. Houston, *J. Phys. Chem.*, **97**, 7239 (1993), G.S. Selwyn and H.S. Johmston, *J. Chem. Phys.*, **74**, 3792 (1981).

17. K.M. Monahan and W.C. Walker, *J. Chem. Phys.*, **63**, 1676 (1975).

18. M.J. Bronikowski and R.N. Zare, *Chem. Phys. Lett.*, **166**, 5 (1990).

19. D. Zolandz, D. Yaron, K.I. Peterson, and W. Klemperer, *J. Chem. Phys.*, **97**, 2861 (1992).

20. Y. Hurwitz and R. Naaman, *J. Chem. Phys.* **102**,1941 (1995).

Chapter 6 is mainly based on the following articles:

K. Imura, M. Veneziani, T. Kasai, R. Naaman, *J. Chem. Phys.*, **111**, 4025 (1999).

Summary

In chapter 1, the author gives an outline of historical background that motivated him to do this work described in the following.

In chapter 2, the author gives several experimental techniques and the principle of neutral cluster size-selection.

In chapter 3, the author shows the results of hexapole focusing measurements in order to elucidate the nature of quantum tunneling motion in HCl dimer and DCl dimer. The focusing curves of the HCl and DCl dimers were obtained using a 60-cm and 2.1-m long electrostatic hexapole field. The results indicates that the existence of two types of the dimer. The first one is homodimer, namely either the $H^{35}Cl$-$H^{35}Cl$ or the $H^{37}Cl$-$H^{37}Cl$, for which the data indicate fast tunneling motion. The second one is heterodimer, namely $H^{35}Cl$-$H^{37}Cl$ or $D^{35}Cl$-$D^{37}Cl$, that does not show any evidence for such tunneling motion on the time scale of the experiment. In the case of HCl dimers, even at relatively high fields, only the heterodimer could be focused. The fact that we could observe quasi-first Stark effect of heterodimer and obtain the permanent dipole moment is due to breakdown of "permutation symmetry" in the heterodimer. The electric dipole moments for both $(DCl)_2$ isotopomers were determined to be 1.5 D ± 0.2, which are the same value as observed for $(HCl)_2$.

In chapter 4, the author demonstrates the structure selection of neutral small clusters by using the hexapole electrostatic field. By combining it with the laser evaporation method, dipole moments of several newly synthesized organometallic clusters were determined experimentally. The observe dipole moments of $Al_1(CH_3CN)_1$ and $Al_1(NH_3)_1$ suggest that the direction of charge transfer in cluster strongly depends

on nature of ligand molecule which forms bond to Al atom, namely, CH_3CN or NH_3. In addition, the author studied on $Al_1(C_6H_6)_1$ cluster using the same method, and he found that the focusing curve consists of two components. One component at lower hexapole rod-voltage comes from molecule which holds C_{6v} symmetry. The other component at higher voltages is due to asymmetric top molecule with C_s symmetry. These experimental results demonstrate that the electrostatic hexapole state-selector has a potential to sensitively separate structural neutral isomers in non-destructive way. Furthermore, structures and dipole moments of $M_1(C_6H_6)_1$ (M = Ti, V, Co, Ni) were investigated experimentally. Experimental results showed a large dipole moment of the 1:1 cluster with early transition metal such as Ti and V, while the corresponding cluster with late transition metal was small. This difference can be explained by the difference in bonding characters in $M_1(C_6H_6)_1$. Namely, both de_1-Le_1 donation and de_2-Le_2 back-donation are important to stabilize the clusters of the early transition metals while for the corresponding clusters of the late transition metals, only the de_2-Le_2 back-donation contributes to the stabilization.

In chapter 5, the reaction of HCl dimer with Ne^* atom was investigated for the first time. It was revealed that HCl dimer could also produce $HCl^+(A)$ as well as HCl monomer, although it is believed that the dimer would not produce the ion. This suggests that HCl ionization occurs at relatively long impact parameter and the de-excitation of the metastable rare gas Ne^* atom would not affect so much following reaction in the Penning ionization.

In chapter 6, the reaction of $O(^1D)$ with water and water clusters was studied. The author measured the nascent product state-distributions in the reaction photo-initiated by the dissociation of N_2O at 193 and 212.8 nm, and the corresponding photo-

initiated intracluster reaction. The study at two different wavelengths for dissociation and the use of D_2O allowed him to obtain direct information on the effect of initial collision kinetic energy about the energy distribution of the product. Based on the new results obtained, the author concludes that the reaction of $O(^1D)$ with water occurs through abstraction mechanism with a relatively short-lived collision complex. In the case of the intracluster reaction, the author has indication that more internal energy is deposited in the N_2 moiety, compared to the dissociation of an isolated N_2O. In addition, the results indicate that the reaction between the oxygen atom and water in the complex involved the formation of a short lived collision complex, with a lifetime of probably only a few rotations of OH.

Through these works, the author can successfully get insight of fundamental natures and reactivity of small clusters. He also amazingly demonstrates the wide applicability of the hexapole technique with the aid of *ab initio* calculations.